

Development of a high repetition rate narrowband optical parametric oscillator and its applications

By

Someswara Rao CH

(Enrolment No: PHYS01201204010)

**Bhabha Atomic Research Centre,
Mumbai - 400085, India.**

*A thesis submitted to the
Board of Studies in Physical Sciences
In partial fulfillment of requirements
for the Degree of*

DOCTOR OF PHILOSOPHY

of

HOMI BHABHA NATIONAL INSTITUTE



December 2018

Homi Bhabha National Institute

Recommendations of the PhD Viva Voce Committee

As members of the Viva Voce Committee, we certify that we have read the dissertation prepared by Shri Someswara Rao CH entitled "Development of a high repetition rate narrowband optical parametric oscillator and its applications" and recommend that it may be accepted as fulfilling the thesis requirement for the award of Degree of Doctor of Philosophy in Physical Sciences.

Chairman - Prof. D.J. Biswas, BARC  Date: 12/07/19

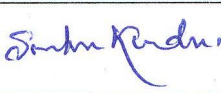
Guide / Convener - Prof. Alok K. Ray, HBNI  Date: 12/07/19

Examiner - Prof. P. K. Dutta, IIT Kharagpur  Date: 12/07/2019

Co-guide - Dr. J. P. Nilaya, BARC  Date: 12/7/2019

Member 1- Prof. S. K. Dixit, RRCAT  Date: 12/7/2019

Member 2- Dr. R.J. Kshirsagar, BARC  Date: 12/7/2019

Technology Adviser - Shri S. Kundu, BARC  Date: 12/7/2019.

Final approval and acceptance of this thesis is contingent upon the candidate's submission of the final copies of the thesis to HBNI.

I hereby certify that I have read this thesis prepared under my direction and recommend that it may be accepted as fulfilling the thesis requirement.

Date: 12/07/2019

Place: Trombay.

Signature 
Guide (ALOK K. RAY)

STATEMENT BY AUTHOR

This dissertation has been submitted in partial fulfillment of requirements for an advanced degree at Homi Bhabha National Institute (HBNI) and is deposited in the Library to be made available to borrowers under rules of the HBNI.

Brief quotations from this dissertation are allowable without special permission, provided that accurate acknowledgment of the source is made. Requests for permission for extended quotation from or reproduction of this manuscript in whole or in part may be granted by the Competent Authority of HBNI when in his or her judgment the proposed use of the material is in the interests of scholarship. In all other instances, however, permission must be obtained from the author.



Someswara Rao CH

DECLARATION

I, hereby declare that the investigation presented in the thesis has been carried out by me. The work is original and has not been submitted earlier as a whole or in part for a degree/diploma at this or any other Institution / University.



Someswara Rao CH

List of publications

Journal Publications:

1. High repetition rate nanosecond optical parametric oscillator pumped by the third harmonic of a DPSSL;
C.S. Rao, S. Kundu, and Alok. K. Ray;
Applied Physics B (2018) 124: 163
2. A Single longitudinal mode high repetition rate BBO Optical Parametric Oscillator pumped by the third harmonic of a DPSSL;
C.S. Rao, S. Kundu, and Alok. K. Ray;
Applied Physics B (under review)
3. The effect of elliptical focusing on the threshold of a nanosecond BBO crystal Optical Parametric Oscillator;
C.S.Rao, G. Kondayya, S.Kundu, and Alok K. Ray;
Journal of Modern Optics (under review)

Conference publications:

1. Single mode operation of a 355 nm pumped nanosecond Type-II β -BaB₂O₄ Optical Parametric Oscillator, C.S.Rao, R.C Bapna and K.Dasgupta, Proceedings of National Laser Symposium (NLS-21), 2013
2. High pulse repetition frequency, nanosecond, visible type-I β -BaB₂O₄ Optical Parametric Oscillator, C.S.Rao, A.K.Ray, and Sucharita Sinha, Proceedings of National Laser Symposium (NLS-21), 2016
3. Optimum elliptical focusing condition for β -BaB₂O₄ (BBO) Optical Parametric Oscillator. C.S.Rao, G.Kondayya and A.K.Ray, Proceedings of National Laser Symposium (NLS-26), 2017
4. Thermal effects in high average power, visible Optical Parametric Oscillator, C.S.Rao, Umesh Kumar, S.kundu and A.K.Ray, Proceedings of National Laser Symposium (NLS-26), 2017.

Acknowledgments

I take this opportunity to express my heartfelt gratitude to my guide Prof. Alok Kumar Ray, for his encouragement, patience, valuable guidance, and never ending support during this research work. His dedication and commitment to work have inspired me to improve myself. Without his help and detailed critical reviewing, this thesis would not have been what it is.

I am indebted to Prof. K. Dasgupta, who had initiated me into the field of optical parametric devices. I have benefited greatly from his insightful thoughts and guidance, which has improved my understanding of the subject.

I am grateful to my previous mentor Dr. R.C. Bapna, for his guidance and contribution towards the development of OPO lab facility. I have greatly benefited from his active involvement in some experiments and useful discussions at the initial stages of the work.

I would like to express my sincere gratitude to Dr. J. Padma Nilaya, co-guide for her fruitful suggestions and encouragement.

I am grateful to Shri S. Kundu, for the supervision and technical support. I have greatly benefited from his active involvement in some experiments.

I gratefully acknowledge the insightful comments and suggestions rendered by doctoral committee constituting senior scientists Prof. D.J. Biswas (chairman), Prof. S.K. Dixit, and Dr. R.J. Kshirsagar

I am grateful to Shri R. K. Rajawat, AD BTDG & Head L&PTD, for the encouragement and support.

I would like to thank my friend Dr. G. Kondayya (Naidu) for his help in numerical simulations. It is always motivating to work with an enthusiastic, dynamic and lively colleague like him.

I would like to express my most sincere gratitude and appreciation to my senior colleagues, Shri N. Kawade, Dr. G. Sridhar, Dr. V.S. Rawat (my badminton partner), Shri T.B. Pal, Dr. R.C. Das and Dr. S. Pradhan for active collaboration and stimulating discussions during this work.

It gives me great pleasure in acknowledging the support offered by my colleagues Jinesh, Seema, Wahid, Anil, Amit, Ajit, J.S.B, Mourya, Pooja, Priya, and my good friend Dhumal during this work.

It gives pleasure to express my special thanks to my friends Venu and Teja for their constant support and for sharing my pains.

I would like to express my gratitude to my parents and brothers for their love and everlasting care.

Finally, I would like to express my appreciation to my wife Sri, and my lovely kids Karthik and Shreya for their patient understanding and support during this work.

Table of Contents	Page No.
SYNOPSIS	xiii
List of Figures	1
List of Tables	5
1. Introduction and Theory of Parametric Interactions	7
1.1 Introduction	7
1.1.1 Background of optical parametric process	12
1.1.2 Motivation for the present work	19
1.1.3 Thesis Outline	21
1.2 Theory of optical parametric interactions	22
1.2.1 Nonlinear Polarization	23
1.2.2 Second Order Nonlinear Polarization	24
1.2.3 Optical Parametric Generation	25
1.2.4 Coupled Wave Equations	26
1.2.5 Optical Parametric Amplifications and Gain	28
1.2.6 Phase matching	31
1.2.7 Birefringent Phase Matching	32
1.2.8 Parameters affecting the phase matching condition	35
1.2.9 Walk-off effects	36
1.3 Optical Parametric Oscillators (OPOs)	39
1.3.1 Threshold of a nanosecond OPOs	42
1.3.2 Nonlinear Crystals Selection	44
1.3.3 Pump Laser Considerations	46

2.The effect of elliptical focusing on the threshold of a BBO crystal OPO

2.1 Introduction	50
2.2 Threshold of a nanosecond OPO under elliptical focusing	51
2.3 Numerical model: BBO OPO	56
2.4 Numerical Results	56
2.4.1 Optimum elliptical focusing condition for low threshold operation of a BBO OPO	56
2.4.2 Optimum elliptical focused parameter for damage free high repetition rate operation of the BBO OPO.	60
2.4.3 Experimental verification	61
2.5 Conclusions	65

3.Design and development of a DPSSL (355 nm) pumped high repetition rate nanosecond BBO OPO

3.1 Introduction	67
3.2 High repetition rate Type-I Phase matched BBO OPO	70
3.2.1 OPO Configuration	70
3.2.2 Nonlinear Crystal	73
3.2.3 Pump laser requirements	74
3.2.4 Pump Laser System	76
3.2.5 Pump beam focusing geometry	79
3.3 Experimental Results	81
3.3.1 Performance of the OPO	81

3.3.2	Long term power stability	85
3.3.3	Spectral linewidth	86
3.3.4	Beam quality and pointing stability:	89
3.4	Conclusions	91

4.Design and development of a high repetition rate single longitudinal mode BBO OPO pumped by 355 nm

4.1	Introduction	93
4.2	High repetition rate Type-II phase matched BBO OPO	96
4.2.1	Type II BBO OPO configuration	96
4.2.2	Performance of the Type-II BBO OPO	100
4.3	Reduction of spectral linewidth of Type II BBO OPO	107
4.3.1	Type-II BBO OPO with double pass pump beam configuration	107
4.3.2	Performance characteristics of Type II BBO OPO in double pass pump configuration	109
4.4	High repetition rate Single Longitudinal Mode (SLM) Type II BBO OPO	113
4.4.1	Design of SLM Type II BBO OPO	113
4.4.2	Development of automated SLM OPO Module	116
4.4.3	Performance characteristics of SLM OPO	120
4.5	Conclusion:	132

5.High average power operation of the OPO limited by thermal loading in BBO crystal

5.1	Introduction	133
5.2	Measurement technique of thermal loading in BBO crystals	135

5.3 Effect of high average power operation on the performance of Type-II BBO OPO	139
5.3.1 The effect of thermal loading in Type-II BBO OPO	139
5.3.2 Average power scaling limits of Type-II BBO OPO	143
5.4 Conclusion:	146
6.Application of narrowband OPO for measuring attenuation coefficient of seawater samples in visible spectral region for underwater communications	
6.1 Introduction	148
6.2 OPO based seawater optical attenuation coefficient measurement technique	149
6.3 Experimental Results	151
6.3.1 Comparison of optical attenuation coefficient of various water samples	151
6.3.2 Determination of laser transmission window of seawater samples	153
6.4 Conclusions:	154
Summary	155
References:	157



Homi Bhabha National Institute

SYNOPSIS OF Ph. D. THESIS

- 1. Name of the Student: Someswara Rao CH**
- 2. Name of the Constituent Institution: Bhabha Atomic Research Centre**
- 3. Enrolment No. : PHYS01201204010**
- 4. Title of the Thesis: Development of a high repetition rate narrowband Optical Parametric Oscillator and its applications**
- 5. Board of Studies: Physical Sciences**

SYNOPSIS

(Limited to 10 pages in double spacing)

Optical Parametric Oscillators (OPOs) have established as a highly efficient and versatile source of coherent tunable radiation in the visible to NIR spectral region. The attractive features of these laser sources include all solid-state compact design and the possibility of very broad wavelength tuning range using just a single nonlinear crystal and their ability to cover those wavelength ranges that are not straightforwardly accessible to conventional tunable lasers such as dye lasers, Titanium Sapphire laser, and diode lasers. Interestingly, these OPOs are distinctively

different from conventional lasers in which the laser is achieved via population inversion. Conversely, the tunable coherent radiation is achieved in OPO's through three-wave mixing non-linear process mediated by the NLO susceptibility $\chi^{(2)}$ in a noncentrosymmetric crystalline medium.

Since these OPOs are based on the solid-state medium, they can be configured as a compact robust device, suitable for use in industrial background and field applications. More importantly, their wide wavelength tunability turned out to be ideal light sources for an enormous number of applications in energy, environment, and healthcare, as well as, in basic and applied sciences. Using a variety of pump lasers, non-linear crystals, and resonator configurations, OPOs have been developed that produce tunable coherent radiation from 300 nm to about 20 μm . Further, highly monochromatic continuous wave (CW) OPOs, as well as, specially designed configurations, producing, or, amplifying ultrashort femtosecond pulsed laser beams, have been demonstrated.

Of these numerous optical configurations, pulsed beta-barium borate (BBO) optical parametric oscillators (OPOs) pumped at 355 nm with a frequency tripled, Q-switched Nd: YAG laser, and producing tunable output in the visible-NIR region from ~ 420 nm to ~ 2.5 μm [1, 2] has grown as the most versatile source for wide-ranging spectroscopic applications [3]. However, the BBO crystal based OPO requires high threshold fluence (0.2 J/cm²) [4] to achieve tunable coherent radiation across its tuning range because of its inherent nonlinear parametric process. Moreover, the phase-matching properties of these BBO crystals demand high quality spatial and temporal profiles of the pump lasers and the birefringence properties of the BBO crystal necessitate larger size pump beams to compensate walk-off effect. Reducing the threshold pump pulse energy by tight focusing of the pump beam is counterproductive as the beam walk-off reduces the effective interaction length, and reduces the optical conversion efficiency. As a result, BBO based OPO

demand high pulse energies (~ 30 mJ) of the pump lasers to operate it well above threshold. The UV pump lasers operating at high repetition rate (≥ 5 kHz) with a pulse energy of ~ 30 mJ at ~ 355 nm are not currently available. Hence, these OPO's are limited to operate at low repetition rates (10-50 Hz). Thus, despite of its far superior characteristics as a widely tunable solid-state laser source, the visible-NIR pulsed OPO has not yet been able to substantially replace the ubiquitous dye laser in numerous laser spectroscopy labs, especially, in application areas such as industrial processing, process monitoring, remote sensing and ultra-sensitive trace detection, where the effectiveness of the application is directly proportional to the duty cycle of the pulsed radiation source. Additionally, for narrowband OPO operation, the UV pump laser power requirement would be substantially higher. To demonstrate the multi-kHz repetition rate, high average power operation of these OPO's, a substantial reduction of threshold pump pulse energy, down to less than 1 mJ/pulse, is necessary.

Among BBO crystal based OPO's, Type-I phase-matched BBO OPO's exhibit broad spectral linewidth. The spectral linewidth of type I BBO OPO's varies from sub-nanometer to few nanometers as the wavelength is tuned toward degeneracy. Alternatively, Type-II phase-matching BBO OPO exhibits much narrower linewidth throughout the entire tuning range. However, divergence broadening in Type-II phase matching is more predominant and it is much larger than the inherent spectral linewidth arising due to parametric process [5].

In addition, the residual absorption of laser beams within the BBO crystal due to high average power operation of these OPO's, pumped with high average power UV lasers cannot be neglected. This leads to inhomogeneous heating of the nonlinear optical crystal that results in spatial temperature gradient and refractive index changes. The spatial inhomogeneous refractive

index changes lead to spatially varying phase-matching conditions, limiting the attainable average power, bandwidth and beam quality of OPO [6].

Hence, the investigations on optical configurations to reduce the threshold pump energy for pulsed BBO based OPOs are an active research area and is being pursued in our lab. We have developed a cylindrical focusing technique by which a substantial reduction in the threshold energy of Type-I BBO crystal based OPO was achieved, down to less than 1 mJ/pulse, using the third harmonic (355 nm) of a Q-switched Nd:YAG pump laser operating at 10 Hz pulse repetition frequency (PRF) [4]. It may be noted that the cylindrical focusing technique which maintains a larger beam size in the walk-off sensitive plane increases the interaction length of the pump and the signal while maintaining high field intensity simultaneously as the beam is focused in the insensitive plane of the BBO crystal. As a consequence, the threshold pump pulse energy of the OPO decreases significantly. In addition, it reduces the optical densities in the crystal and thus optical damage due to high intensities as well as the high average power of the pump and signal beams can be avoided.

The aim of my work presented in this thesis was to numerically study the effect of cylindrical focusing on the threshold of BBO crystal OPO and determine the maximum elliptical pump beam spot size for which the threshold energy of the BBO crystal OPO reduces to ≤ 1 mJ/pulse. Consequently, that would allow us to use commercially available frequency tripled (355 nm) Q-switched, multi-kHz PRF, DPSSL (diode pumped solid-state laser), which can deliver pulse energies of 2-2.5 mJ to pump the BBO OPO without damaging the crystal due to high average power operation. By integrating the recently developed pump threshold reduction technique using cylindrical focusing geometry and further by applying the numerical model calculations on its optimized optical configuration design, we have developed and reported [7] a high PRF (5 kHz),

nanosecond, visible-NIR BBO-OPO by pumping with the third harmonic of a DPSSL. It may be noted that this is the first report on a high repetition rate (5 kHz) visible-NIR BBO-OPO.

Further, the performance of the developed high repetition rate OPO has been characterized in detail. These studies were extended to develop the new spectral narrowing designs for achieving the narrowband, including single longitudinal mode (SLM) operation, of these high average power OPOs. Accordingly, the dissertation work was widened to study the thermal loading in the BBO crystal arising due to high repetition rate operation, which enabled us to determine the average power scaling limit of such visible nanosecond OPO's. Subsequently, the usefulness of the in-house developed narrowband, high average power, widely tunable OPO's was tested in our applied program.

Interestingly, the in-house development of such high repetition rate, narrowband OPO tunable in the visible-NIR, which has turned out to be a new outcome of this dissertation work will be useful for many applications in our organization.

The content of the thesis is presented in six chapters, which are briefly summarized in the following.

Chapter 1:

This chapter of my thesis starts with the introduction to Optical Parametric Oscillators and basics of nonlinear optics, second-order nonlinear polarization, the basic principles of optical parametric generation, nonlinear crystal properties, phase matching considerations, walk-off effects and pump laser characteristics are discussed. This chapter describes a brief review of the recent progress of the OPOs, in particular nanosecond, pulsed, visible-IR OPOs. The aims and objectives of the work and the underlying motivation are discussed in detail.

Chapter 2:

This chapter of my thesis deals with the numerical study on the effect of cylindrical focusing of the input pump beam on the threshold of a singly resonant nanosecond β -BaB₂O₄(BBO) optical parametric oscillator (OPO) pumped by the UV lasers. The results of the numerical model illustrate a substantial reduction in the threshold of the OPO with the optimum elliptical focusing parameters of the pump beam. The maximum size of the elliptical focused beam of the 355 nm pump laser for which the threshold energy of the Type-I BBO crystal based OPO reduces to ~ 1 mJ has been deduced from the numerical model. This helped us to configure the developed BBO based OPO to pump with a third harmonic (355 nm) output of a high PRF (5 kHz) DPSSL system operating with a pulse energy of $\sim 2 - 2.5$ mJ and to demonstrate its damage-free high average power operation.

Chapter 3:

This chapter of my thesis describes the design, construction and performance characterization of high repetition rate (5 kHz), nanosecond, Type-I phase-matched β -BaB₂O₄ (BBO) crystal based optical parametric oscillator (OPO), pumped by the third harmonic (355 nm) of a Diode Pumped Solid State Laser (DPSSL), which is demonstrated for the first time. The performance of the OPO has been studied and compared for different gain lengths of the Type-I BBO crystal, which facilitated to determine the optimum length of the crystal for the efficient operation of the OPO. Important parameters like optical conversion efficiency, the performance of the OPO across its tuning range and spectral bandwidth are measured and analyzed. The test results of the long-term stability of the OPO operating at its peak wavelength at a repetition rate of 5 kHz have been presented. During this stability test intention, the OPO was operated with an average power of 2.6 W, having a conversion efficiency of 26 % with power stability of 1.9 %.

Chapter 4:

The design and construction of a high repetition rate, Type-II phase-matched BBO crystal OPO for the narrowband operation has been described in this chapter of the thesis. The performance of the Type-II BBO OPO has been studied for its efficiency and spectral linewidth. The double pass pump beam technique, which we have implemented for reducing the spectral linewidth to ~ 0.15 nm for the high repetition rate, Type-II phase-matched BBO crystal OPO, has been discussed. The performance comparison of high repetition rate, Type-I BBO OPO, and Type-II BBO OPO with double pass pump beam configuration in terms of efficiency and spectral linewidth has been studied and analyzed.

The last part of this chapter describes a new approach for achieving a single longitudinal mode (SLM) operation of the OPO. The SLM OPO cavity design and construction has been discussed in detail and the spectral linewidth of SLM OPO has been measured across the OPO tuning range and analyzed. The time average spectral linewidth of the SLM is measured to be ~ 350 MHz.

Chapter 5:

This chapter of the thesis describes the adverse thermal effects arising from the optical absorption in nonlinear crystals due to high average power operation OPO's. The experimental setup and measurement technique of the temperature gradients at high average power pumping of the crystal has been described in detail. From the measurements, it is observed that the temperature gradient arising in Type-II BBO crystal is greater than its acceptable temperature bandwidth, at 3 kHz PRF. Consequently, the performance of this OPO starts to degrade when the pump laser is operated beyond 3 kHz with pulse energy above 2 mJ, owing to the thermal effects arising due to the absorption of the pump beam.

Chapter 6:

This chapter of the thesis describes the experimental setup for measuring the optical attenuation coefficient of various water samples including seawater for use of these data in underwater communication by utilizing the widely tunable (from 450-650 nm), high repetition rate (2 kHz), narrowband OPO. The variation of the attenuation coefficient of seawater sample as a function of wavelength illustrates the maximum transmission window of the seawater in the visible region.

Summary:

Developed broadband, high repetition rate (5 kHz), Type I BBO OPO, which can be continuously tuned from 490 nm to 630 nm and operates at a maximum power of 3.2 W with a conversion efficiency of ~ 28 %. For achieving narrowband operation of the OPO, utilized Type-II BBO crystal in the double pass pump beam configuration and achieved narrowband (0.15 nm - 0.19 nm) output at a repetition rate of 2 kHz across its tuning range. Further, single mode operation of the OPO is achieved by using a Fabry Perot etalon inside the cavity of Type-II BBO OPO with double pass pump beam reflector. The spectral linewidth of the SLM OPO is measured to be ~ 350 MHz. Thermal loading in the BBO crystal arising due to high repetition rate operation was studied for determining the average power scaling limit of visible nanosecond OPO's. Utilizing the home built high repetition rate, narrowband OPO, determined the wavelength at which the attenuation coefficient of seawater is minimum for the use in underwater communications.

References:

1. L. K. Cheng, W. R. Bosenberg, and C. L. Tang, *Appl. Phys. Lett.* **53**, 175 (1988).
2. Y. X. Fan, R. C. Eckardt, R. L. Byer, J. Nolting, and R. Wallenstein, *Appl. Phys. Lett.* **53**,

2014 (1988).

3. J. G. Haub, M. J. Johnson, and B. J. Orr, *J. Opt. Soc. Am. B*, **10**, 1765 (1993).
4. R.C. Bapna, C.S. Rao, K. Dasgupta, *Optics & Laser Technology*, **40**, 832 (2008).
5. G. Anstett, G. Göritz, D.Kabs, R. Urschel, R.Wallenstein, A. Borsutzky, *Appl. Phys. B* **72**, 583 (2001).
6. Norman P. Barnes and Julie A. Williams-Byrd, *J. Opt. Soc. Am. B*, **12**, 124 (1995).

List of Figures

Fig.1.1: Schematic of a singly resonant optical parametric oscillator.	11
Fig.1.2: Comparison of spectral coverage of prominent tunable lasers with the OPO devices....	17
Fig.1.3: Spectral coverage of the OPO devices based on birefringent and periodic poled nonlinear materials.....	18
Fig.1.4: Optical parametric generation in which a pump photon of frequency ω_p splits into two photons of frequency ω_s (signal) and ω_i (idler)	26
Fig.1.5: The walk-of angle ρ between the wave vector k and the Poynting vector S in a negative birefringent BBO crystal.....	38
Fig.1.6: Schematic illustration of the walk-off effect of ordinary and extraordinary waves.....	38
Fig.1.7: Angle tuning curve of BBO-OPO pumped at 355 nm, with type-I interaction.	41
Fig.2.1: Variation of spatial coupling coefficient h_{sm} with the pump beam focusing parameter ($\xi_p = \xi_s = \xi$) for different values of beam ellipticity factor $\vartheta_{\text{ellipse}}$ for the parametric conversion in BBO crystal.....	58
Fig.2.2: Variation of spatial coupling coefficient h_{sm} as a function of the beam ellipticity factor $\vartheta_{\text{ellipse}}$ for parametric conversion in BBO crystal.	59
Fig.2.3: Variation of threshold pulse energy as a function of the beam ellipticity factor $\vartheta_{\text{ellipse}}$ for different focusing parameter of the pump beam in the BBO crystal based OPO.	61
Fig.2.4: Schematic of the experimental setup of the Type-I BBO OPO.....	63
Fig.2.5: Comparison of theoretically calculated and experimentally measured threshold pump pulse energies of the broadband BBO OPO, pumped by 355 nm output of a Q-switched Nd:YAG Laser (10Hz), across its tuning range.....	64
Fig.3.1: Schematic of the experimental setup of Type-I phase matched BBO crystal based OPO..	71
Fig.3.2: Transmission spectra of the BBO OPO cavity optics, A) Input mirror and B) output coupler.....	72
Fig.3.3: Schematic illustration of pump and generated signal, idler beams polarization direction, optic axis direction and axis of rotation for frequency tuning in Type-1 BBO crystal.	72

Fig.3.4: Transmission spectra of the Type-I phase matched BBO crystals used in the OPO setup.	74
Fig.3.5: A) Spectral acceptance bandwidth B) Angular acceptance bandwidth for the pump laser of Type-I BBO OPO.	76
Fig.3.6: The temporal profile of the pump laser (DPSSL) operating at a wavelength of 355 nm at a repetition rate of 5 KHz.....	77
Fig.3.7: The power stability of the pump laser (DPSSL) operating at a wavelength of 355 nm at a PRF of 5 kHz.	78
Fig.3.8: Schematic of the Cylindrical focusing geometry	80
Fig.3.9: The wavelength tuning curve of the Type-I BBO OPO measured using 15 mm long crystal.....	82
Fig.3.10: Variation of OPO signal output power tuned from 490 nm to 630 nm at a fixed pump power of 10 W.	83
Fig.3.11: Performance comparison of signal output power of Type-I BBO OPO for different crystal sizes at 5 kHz repetition rate at a signal wavelength 492 nm.	84
Fig.3.12: The measured temporal profile of the OPO signal output at a wavelength of 492 nm, operated at a repetition rate of 5 kHz.....	84
Fig.3.13: Longterm stability of the Type-I BBO OPO signal output power monitored for the duration 30 min.	85
Fig.3.14: Spectral Linewidth of Type-I BBO OPO as a function of signal wavelength.	87
Fig.3.15: Comparison of theoretical and experimentally observed spectral linewidth of Type-I BBO OPO signal output across its tuning range.....	88
Fig.3.16: The measured M^2 factor, near and far field profiles of the OPO signal beam at a wavelength of 492 nm at a repetition rate of 5 kHz.....	89
Fig.3.17: The measured beam pointing stability of the OPO signal output at a wavelength of 492 nm at a repetition rate of 5 kHz	90
Fig.4.1: Comparison of A) Angle dependence wavelength tuning and B) Nonlinear coefficient in Type-I and Type-II phase matching, pumped at 355 nm.....	97
Fig.4.2: Measured Transmission spectrum of the Type-II BBO crystal used in the OPO setup..	98
Fig.4.3: Calculated A) Spectral acceptance bandwidth B) angular acceptance bandwidth of the Type-II BBO OPO across the tuning range.	99

Fig.4.4: Schematic of the Type-II phase matched BBO crystal OPO used for narrowband operation	99
Fig.4.5: Wavelength tuning curve of the signal wave with change in internal angle to the optic axis of Type-II BBO OPO.	101
Fig.4.6: Signal output performance of the Type-II BBO OPO at different repetition rates of the pump laser.	102
Fig.4.7: Spectral linewidth of Type-II BBO OPO as a function of signal wavelength.	103
Fig.4.8: Comparison of theoretical and experimental observed spectral linewidth of Type-II BBO OPO across the tuning range of the signal wave.	104
Fig.4.9: Comparison of calculated Spectral Linewidth of Type-II BBO OPO arising due to divergence and inherent parametric process.	106
Fig.4.10: The measured M^2 factor, near and far field profiles of the OPO signal beam at a wavelength of 512 nm at a repetition rate of 4 kHz.....	107
Fig.4.11: Schematic of the Type-II BBO OPO with double pass pump geometry.	109
Fig.4.12: Comparison of spectral linewidth of Type-I, Type-II BBO and Type-II BBO OPO using pump double pass configuration.	110
Fig.4.13: Performance comparison of Type-II BBO OPO using pump double pass configuration.	111
Fig.4.14: The measured M^2 factor, near and far field profiles of the OPO signal beam at a wavelength of 560nm at a repetition rate of 2 kHz.....	112
Fig.4.15: Schematic of the Fabry Perot etalon based SLM Type-II BBO OPO, E represents etalon.....	114
Fig.4.16: Schematic of the single longitudinal mode selection using an intra-cavity FP etalon.	114
Fig.4.17: Schematic of the FP etalon based spectral measurement technique.....	120
Fig.4.18: (A) Interferogram of the SLM OPO at 560 nm obtained with 4.5 GHz FP Interferometer. (B) Interferogram of the frequency stabilized He:Ne obtained with 4.5 GHz FP Interferometer.	121
Fig.4.19: Intensity plot of the pixel scan of Interferogram (A), SLM OPO output at 560 nm. .	122
Fig.4.20: Spectral characteristics of SLM Type-II BBO OPO operating at different wavelengths.	123
Fig.4.21: Inherent frequency stability of SLM OPO operating at a wavelength of 564.787 nm.	124

Fig.4.22: Variation of the spectral linewidth during the long-term operation of the SLM OPO operating at a wavelength of 564.787 nm.	125
Fig.4.23: Frequency stability of SLM OPO with cavity stabilized feedback loop.....	126
Fig.4.24: Comparison of the spectral linewidth of the SLM OPO under wavelength locking and without locking.	127
Fig.4.25: Variation of the spectral linewidth of the SLM OPO under wavelength locking.	127
Fig.4.26: Variation of SLM OPO signal output power across its tuning range.....	129
Fig.4.27: Temporal pulse shape of the SLM OPO operating at a wavelength of 518.6 nm at 1 kHz repetition rate.....	129
Fig.4.28: The measured M^2 factor, near and far field profiles of the SLM OPO signal beam at a wavelength of 560 nm at a repetition rate of 1 kHz.....	130
Fig.4.29: Photograph of the High repetition rate SLM OPO operating at a wavelength of ~ 590 nm at 1 kHz repetition rate.....	131
Fig.5.1: Infrared camera image of the crystal acquired when a high repetition rate (5 kHz) pump laser is propagated through the BBO crystal.	138
Fig.5.2: The temperature rise of the crystal with time at locations A and B	138
Fig.5.3: Output performance of the Type-II BBO OPO at high average powers of the input pump laser.	140
Fig.5.4: The longterm power stability of the Type-II BBO OPO at an input power of 9W at 4 kHz repetition rate.....	141
Fig.5.5: Propagation transmission loss of the pump laser beam in the Type-II BBO crystal operating at different repetition rates with a pulse energy of 2.25 mJ.....	142
Fig.5.6: Variation of the output signal power and temperatures of the crystal when the pump laser operating at different repetition rates with pulse energy of 2.25 mJ.....	143
Fig.5.7: Comparison of measured peak temperatures of Type-I and Type-II BBO crystals at different repetition rates of pump laser for set pump pulse energy of 2.5 mJ.	145
Fig.6.1: Schematic of the OPO based optical attenuation coefficient measurement technique.	150
Fig.6.2: Comparison of measured optical attenuation coefficient of different water samples as a function of visible wavelengths.	152

List of Tables

Table 1.1: Possible birefringent phase matching schemes and corresponding field polarizations for parametric generation in uniaxial crystals..... 34

Table 1.2: Properties of the selected nonlinear crystals commonly employed in OPOs. 46

Table 3.1: Important parameters of the BBO crystals used in the high repetition rate OPO..... 73

Table 3.2: Important parameters of the pump laser (DPSSL) used in the high repetition rate OPO 77

Table 4.1: Operating characteristics of high repetition rate OPOs developed at our lab..... 132

Table 5.1: Some important physical and thermal properties of BBO crystal [59] 137

Table 6.1: Operating characteristics of Type-II BBO OPO..... 150

Table 6.2: Measured laser transmission window of various water samples 153

Chapter 1

Introduction and Theory of Parametric Interactions

1.1 Introduction

After the invention of the first laser in 1960 by Theodore H. Maiman [1], there has been always a great deal of interest in the development of a solid-state, compact and robust coherent sources of light, which are capable of providing broad tunable output in the ultraviolet, visible and infrared spectral range. To this end, it has been understood that widely tunable coherent sources with high pulse energies at high pulse repetition frequencies in nanosecond pulse durations would facilitate many technological applications. Obviously, these high average power tunable sources have many potential uses in the fields of basic and applied research, such as spectroscopy, laser isotope separation, environmental monitoring of pollutants, health care, industry, and defense.

In the early days of the laser development, generally, each laser gain medium produced a set of discrete emission wavelengths determined by the internal energy levels of the gain material. Many basic as well as applied researches required new wavelengths and were achieved via nonlinear processes such as Raman shifting and harmonic generation. However, these nonlinear conversion processes to generate new coherent sources are not efficient in many cases. Later, the lasers with significantly wider tuning ranges were developed using gain materials in liquid state with collisionally broadened energy levels in which the transitions from the upper to the lower energy bands can occur over a wide band of frequencies, resulting in continuous laser emission

over a broad spectral range. Thus, the liquid dye laser discovered by P. P. Sorokin and F. P. Schafer was the first laser to achieve wide continuous tunability, and a potential dream of scientists was realized leading to its widespread use in the research labs all over the world. These dye lasers are very versatile [2] and till now widely used in many applications that require wavelength agility, particularly in the visible spectral region, and specific output characteristics such as high power or high pulse energy [3].

However, the utility of these dye lasers has been restricted in many applications by their limited wavelength tuning range of each organic dye molecule as well as messy nature since these dyes are dissolved in inflammable organic solvents to prepare the gain media. The tuning range of these dye lasers is typically in the range of 30-40 nm using a single dye gain medium. Therefore, the dye lasers require many such dyes having fluorescence emission in overlapping spectral region to cover even the entire visible spectral range. Moreover, the rapid photo-degradation of the large organic dye molecules in the near IR and UV spectral regions prevents their practical utility at wavelengths beyond below ~350 nm and ~700 nm. Also, the non-radiative transition process, resulted from the photon energy difference between the pump photons and the longer wavelength laser photons in dye laser media, produced localized heat in the excited gain region which leads to the optical inhomogeneity that hinders obtaining good spatial profile of the laser output during high pulse repetition frequency, high average power operation of these dye lasers. To overcome this localized heating in the excited gain volume the dye solution is rapidly circulated such that the active dye volume exposed to the pump laser is removed quickly between successive pump laser pulses [4]. However, the rapid circulation of dye solution is only partially effective in overcoming this problem in dye lasers as it introduces additional inhomogeneities due to turbulence and cavitations at high flow velocities. Furthermore, handling a large volume of toxic and inflammable

dye solution in flow systems with additional safety requirements is a major concern for the high power dye lasers operating at high repetition rates. These large circulating dye solution flow systems with adequate safety increase the complexity of the high average power dye laser system. Therefore, the applicability of high power dye lasers, especially in an industrial environment outside the laboratories, is limited due to the safety and complexity issues related with handling and disposal of such hazardous and toxic dye solutions.

The search for a widely tunable solid-state laser to supplement and replace ubiquitous dye lasers resulted in to various solid-state tunable lasers [5] out of which Titanium-sapphire laser [6, 7] has been widely used in scientific research because of their wide tunability in the spectral region 700 nm to 1100 nm and their ability to generate high repetition rate as well as ultrashort (fs) pulses. In Ti: sapphire tunable solid-state lasers the interaction between the Ti^{+3} ion and the host crystal is such that lattice vibrations or phonon usually accompany the absorption and emission of photons. As a result, the absorption and emission spectra become broadened in such laser and the broad tuning range is achieved due to the vibronic transitions gain over the larger bandwidth. Even though the Ti: sapphire laser exhibit larger tuning range but the wavelength coverage is limited to the near-infrared spectrum, the tuning range is typical ~700 to 1100 nm. Also, in Ti: sapphire laser, high average power operation is limited by heat loading within the gain medium. This thermal loading is caused by large quantum defect since it is generally pumped at 532 nm whereas lasing emission is at 700-1100 nm. Thus, the part of the energy of the pumping photon lost (not turned into photons at the lasing wavelength) in the gain medium at the lasing through non-radiative de-excitation to the ground level. This thermal loading can lead to thermo-optical distortion and lensing, which severely affect the performance and hinders the high average power operation of these lasers.

On the other hand, the Optical parametric oscillators (OPOs) are non-linear solid-state sources of widely tunable coherent radiation [8, 9]. They have turned out to be attractive sources for many applications in regard to their unique features of wide wavelength tunability, can be continuously tunable from the ultraviolet to the infrared spectral range with a single source of the pump laser and a non-linear crystal, as well as of providing high pulse energies. They can be designed as all solid-state, compact and robust devices for use in an industrial environment and field applications. Unlike dye and Ti: sapphire lasers, these OPOs offer a far broader wavelength tunability, shows no photodegradation of its gain medium, and has negligible heating, as it does not involve absorption of pump radiation. As a result, OPOs have been emerging as an ideal source for diverse applications such as trace analysis, LIDAR, laser display, medical research and material processing [10].

Importantly, these OPOs are distinctively different from conventional laser sources in which the process of laser emission is a consequence of population inversion in the laser gain medium. Conversely, the optical gain in the optical parametric devices is achieved through the parametric interaction of the optical fields arising from the nonlinear polarization exhibited by the solid-state gain medium. For practical realization of the parametric process, the material medium which exhibits the nonlinear polarization is a nonlinear crystal enclosed in a resonant optical cavity, formed for example with two mirrors on each side of the crystal as in a conventional laser. A typical schematic of the optical cavity of the OPO is shown in the Fig.1.1. A high-intensity laser beam from the pump laser is focused into the nonlinear crystal of the OPO. If the intensity of incident pump photon is sufficiently high, the optical parametric process-induced is large enough to cross the operating threshold in the resonator for the generation of signal and idler output radiations due to second-order nonlinear polarization, whose frequencies add up to that of the

pump, in accordance with the requirement of energy conservation. The momentum conservation requirement for these radiation fields provides an additional condition for effective conversion of pump laser photons to signal and idler photons. This is achieved by the process of phase matching in birefringent crystals, which along with the energy conservation condition, determines the wavelengths of the two output radiation fields. A very important characteristic of this birefringent phase-matching technique is by changing the orientation of the optic axis of the crystal with respect to the direction of pump radiation, it is possible to adjust the range of generated frequencies, so that optical radiation over a wide range of frequencies can be obtained simply by tilting the parametric crystal appropriately. The theory of optical parametric generation and amplification, which is the basis of this dissertation work, is described in detail in section 1.2.5 of this introductory chapter.

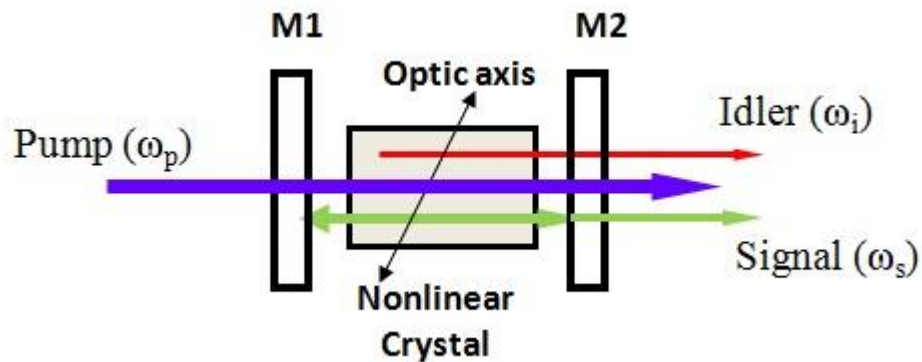


Fig.1.1: Schematic of a singly resonant optical parametric oscillator. M1 and M2 are the broadband plane mirrors. M1: High reflectivity at signal and high transmission for pump and idler wavelengths. M2: Partially reflectivity at the signal and high transmission for pump and idler wavelengths.

1.1.1 Background of optical parametric process

A year after the invention of the laser, Franken et.al demonstrated the second harmonic generation (SHG) of the ruby laser in a quartz crystal [11]. The conversion efficiency of the generated second harmonic radiation was very poor because of the lack of phase matching in quartz material due to dispersion. Two methods were evolved for achieving phase matching to increase the conversion efficiency of the SHG process. One approach by exploiting the birefringence of the crystal to offset the dispersion [12-14] referred as birefringent phase matching and the other one is periodic modulation of the sign of the nonlinear coefficient to reset the optical phase. The latter approach, suggested by Armstrong et al. [15] referred to as quasi-phase-matching (QPM).

The theory of parametric generation and amplification of tunable radiation was developed by Kingston [16], Kroll [17], and Akhmanov et al. [18] which led to the development of Optical Parametric Oscillator for the first time in 1965 by Giordaine and Miller [19]. They used a Q-switched Nd:CaWO₄ laser, frequency-doubled to the green (0.529 μm) to pump a LiNbO₃ nonlinear crystal and generated tunable OPO signal output in the wavelength range of 0.97 μm to 1.15 μm by temperature tuning of the crystal. Since then, many efforts have been given towards understanding and improving the performance of these magnificent laser devices. Numerous nonlinear optical materials have been synthesized and evaluated for possible use in practical optical parametric devices. Despite the early success, the practical realization of these OPO devices was difficult due to the non-availability of reliable nonlinear materials which can sustain the high-intensity pump laser beams that were required to generate practical coherent output at reasonable energy. Moreover, the relatively poor spatial beam quality of available Q-switched pump lasers had restricted effective progress in OPO technology. Detailed discussions on the initial evolution of work on OPOs and related theory can be found in earlier scientific studies [8, 9, 16-20].

These problems of generating reliable and practically useful pulse energies from OPO have been largely overcome after the discovery of excellent new nonlinear crystals such as β -Barium Borate (BBO), Lithium Triborate (LBO), Potassium Titanyl Phosphate (KTP) in the mid-'80s. These crystals exhibit high optical damage thresholds which can sustain high-intensity pump laser beams. Additionally, the improvements in the laser resonator design had led to the development of high-quality Nd: YAG pump lasers [6] with a low-divergence beam with smooth spatial and temporal Gaussian beam profiles which enables the OPOs to operate with good efficiencies.

To this end, OPOs generating efficient and reliable tunable radiation in the UV, visible, or near-infrared, have been derived mainly from BBO and LBO crystals because of their wide transparency range and higher damage thresholds. However, the smaller birefringence in LBO as compared to that in BBO tends to limit the phase-matching spectral range. But this property leads to the possibility of noncritical phase-matching and larger acceptance angle, which is a niche for frequency conversion applications in the visible and near IR as well as ultrafast OPO devices. However, the nonlinear crystals KTP and KTA are the materials of choice for the design of OPOs, pumped with Nd:YAG lasers at 1.064 μm , to generate far IR radiation. The characteristics of the various nonlinear crystals depending on their optical and material properties are discussed in section 1.3.2.

Meanwhile, a wide range of commercial OPO lasers based on improved Q-switched Nd:YAG lasers with its harmonics and good quality non-linear crystals, mainly operating at low pulse repetition frequency such as 10 Hz, have been produced and is available to the researchers for laser spectroscopy applications. These OPOs incorporate birefringent phase-matched BBO, LBO, KTP, or KTA crystals, and are pumped by Q-switched Nd:YAG lasers or 2nd (532 nm) and 3rd (355 nm) harmonics of Nd:YAG, and cover the OPO output wavelength over a wide spectral

region from about 300 nm to more than 3.5 μm . The wavelength can be extended to the UV by doubling the OPO output or mixing it with the pump laser beam. These commercial low repetition rate (10-100 Hz) lasers can generate pulse energies from a few mJ to more than 100 mJ, depending on the OPO design and the pump laser. Various linewidth ranges are offered from broadband (5 to 100 cm^{-1}), to moderate (a few cm^{-1}), to narrow linewidth (less than 0.1 cm^{-1}).

Different types of non-linear crystals are used in birefringent phase-matched OPO to generate efficient broadband or narrowband output. Typically, a broadband type-I OPO offers the highest conversion efficiency, producing the highest output energy for a given pump laser, whereas a type-II OPO exhibits significantly narrower linewidth at the expense of efficiency. However, for an OPO to generate a linewidth narrower than 1 cm^{-1} the OPO must be injection seeded or incorporate line-narrowing optical elements within their cavities (for example, a grating or etalon). These narrow linewidth OPO systems typically offer lower conversion efficiency.

On the other hand, much impetus to the progress of the OPOs has come from the quasi-phase-matched (QPM) NLO media, such as periodically poled (PP) materials PPLN and PPKTP, tailored for specific wavelengths by the periodic structuring of ferroelectric domains [21]. The progress in the lithography technology combined with the technique of periodically reversed polarization domains in ferroelectric crystals in the late 1980s led to the development of microstructured nonlinear crystals for the use in quasi-phase-matched (QPM) nonlinear interactions which enabled the OPOs to operate in regimes inaccessible to conventional birefringently phase-matched media as shown in the Fig.1.2. A reversal of the ferroelectric's domains corresponds to a sign reversal of the nonlinear coefficient. In QPM materials the phase matching is implemented by reversing the sign of nonlinear coefficient with a period twice the

coherence length. These QPM media offer higher nonlinear-optical coefficients, lower operating thresholds, and smaller size than birefringent phase-matched OPO materials.

However, QPM devices are limited to near and mid-IR wavelength range because of difficulties in generating shorter period gratings that are needed to match coherence lengths of visible and UV radiations [22]. A detailed description of the theory and summaries of recent work on OPOs with QPM micro structured crystals can be found in [9].

On the other hand, using a variety of pump lasers, crystals, and resonator configurations, OPOs have been developed that produce tunable outputs from 300 nm to about 20 microns as shown in the Fig.1.3. Highly monochromatic CW OPOs, as well as, specially designed configurations, producing, or, amplifying ultrashort-pulse OPO systems, have been demonstrated. This progress is well documented, for example, in the feature issue of Journal of Optical Society of America B, concentrating on CW and nanosecond pulsed OPO [23], and in a subsequent issue [24], dealing principally with synchronously pumped, ultrashort pulsed OPO systems.

Of late, the promising features of BBO crystal such as wide transmission range (189 to 3000 nm), high non-linearity (about four times that of KDP) and high damage threshold, as well as the phase-match ability over its whole transparency regime [25] had revived the research and technological interest in OPOs. The BBO crystal has been recognized as an excellent choice as a nonlinear optical crystal for nanosecond pulsed OPO's operating in the UV, visible and IR range. Y. X. Fan et al [26] has demonstrated for the first time the operation of BBO crystal based OPO, pumped with the second harmonic of the Nd:YAG laser, which is tunable in the NIR, and later the tuning range of the BBO OPO has been extended to visible to NIR by pumping with 355 nm [26,27].

The nanosecond BBO OPOs have been pumped with different pump lasers such as second (532 nm), third (355 nm) or fourth (266 nm) harmonic output of the Nd:YAG laser [28-34], Excimer laser (308 nm) [35-36]. Advantageously, the tuning range of these OPOs, together, extends largely from 302 nm to 3270 nm. Among different pump wavelengths, the favorable choice is pumping with the third harmonic at 355 nm because of sufficient broad tuning range which extends from 400 nm to 2500 nm. Output pulse energies from a few mJ to tens of mJ can currently be made available from these devices in pulses of 1 to 10 ns duration, at up to ~ 100 Hz repetition rates and with optical extraction efficiencies in excess of 30 percent. Because of the high optical damage threshold of the crystal, energy scaling of BBO OPOs to the multi joule level is also attainable with the use of high-energy pulsed pump sources [34].

However, one of the major drawbacks of these free-running BBO-OPO's is that they exhibit broad spectral linewidth which varies from few \AA far from degeneracy to few hundreds of \AA near degeneracy. To reduce the spectral linewidth, additional intra-cavity line-narrowing optical elements such as gratings or etalons may be introduced into the OPO cavity. For this purpose, novel efficient resonator architectures using different combinations of gratings and etalons have been realized [31,37-40]. Even, the single longitudinal mode (SLM) operation in BBO-OPO using two intra-cavity etalons has been demonstrated by Robertson et.al [41]. However, the introduction of these intra-cavity line-narrowing elements raises the oscillation threshold with a corresponding reduction in the output power and efficiency. The alternate approach to obtain the narrow linewidth at high output power levels is injection-lock a high power oscillator with a low power narrow linewidth oscillator [42]. Utilizing this injection seeding technique, narrowband operation of the BBO OPO's with a bandwidth of $< 0.1 \text{ cm}^{-1}$ was demonstrated [10,43]. Although this technique

offers high pulse energies and efficiencies, the tenability of the seeded system depends on the corresponding limited frequency range of the seed laser.

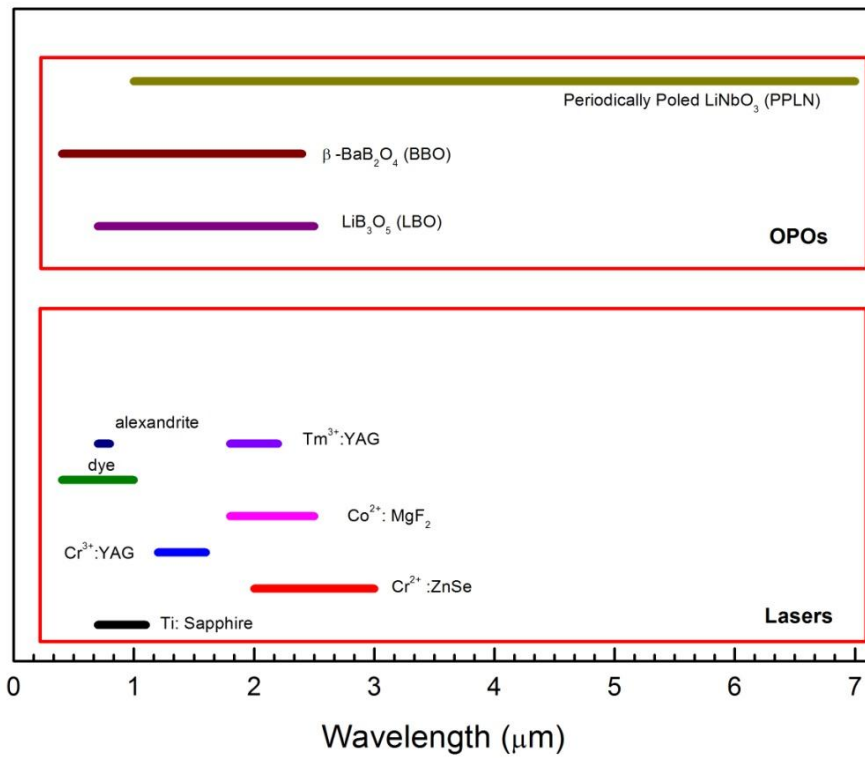


Fig.1.2: Comparison of spectral coverage of prominent tunable lasers with the OPO devices [9]

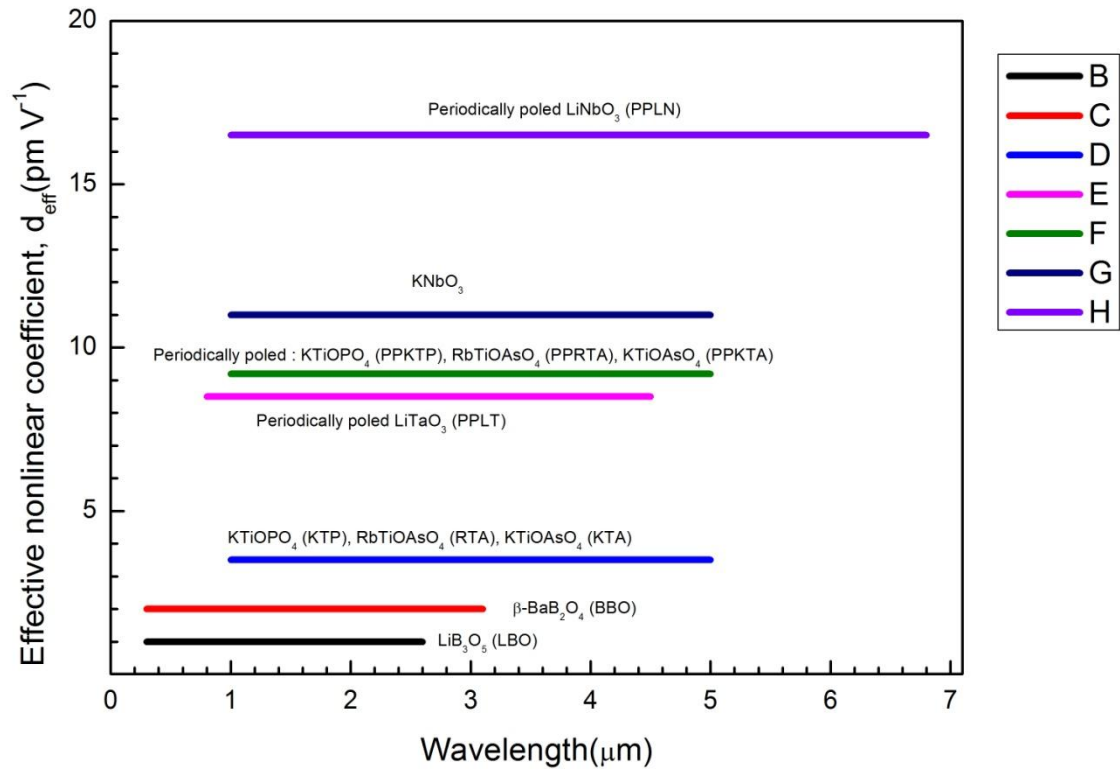


Fig.1.3: Spectral coverage of the OPO devices based on birefringent and periodic poled nonlinear materials [9]

1.1.2 Motivation for the present work

Multi-kHz repetition rate, narrowband coherent sources, continuously tunable at visible and near-IR region of radiation, are pivotal to many basic and applied scientific applications such as sensitive and selective detection/analysis of trace gases and metrology by laser absorption spectroscopy, selective separation of isotopes/elements for radio-pharmaceutical and nuclear energy use using laser resonance photo-ionization spectroscopy etc. These applications not only require wide tunability but also demand reliable and sustainable operations of narrow bandwidth lasers with sub-mJ to a few mJ pulse energy as well as high repetition rates (5-10 kHz), making such robust coherent sources challenging to develop. All solid-state widely tunable coherent sources, developed using multi-kHz repetition rate DPSSL pumped OPO, is one such promising laser system.

It is well understood that among various prominent tunable OPOs, as illustrated in the Fig.1.2, the non-linear crystal BBO based OPO pumped with the third harmonic (355 nm) of a Q-switched Nd:YAG laser offers wide tuning range, both in the visible as well as in near-IR spectral range. In addition to its wide wavelength tunability, BBO crystal based OPOs also exhibit high optical conversion efficiencies and high damage threshold, making them the most versatile practical devices for diverse scientific and industrial applications.

High pulse energy (few mJ) output based on BBO crystal OPOs have been demonstrated by many groups [28,29,30]. However, to avoid damage to the BBO crystal at high pulse energies, the pump intensity is controlled by adopting large pump beam sizes on the crystal for such OPO systems. This increases the pulse energy requirements of the pump source at 355 nm generally, restricting the repetition rates of the OPO to a few Hz. On the other hand, if the repetition rate of the system is increased to multi-kHz, the output energy and beam quality of the OPO is limited by

the phase-mismatch in the BBO crystal, arising due to the temperature dependent refractive index change from residual absorption of pump energy in the BBO. Thus, to develop a high (few mJ) pulse energy, high repetition rate (5-10 kHz), widely tunable narrowband OPO in the visible spectral range, it is important to devise a strategy to minimize the pump threshold and optimize the conversion efficiency of such OPOs along with minimizing thermal effects. Such OPO systems are not commercially available and therefore, need to construct and develop from the scratch for required applications within DAE.

Recently, high repetition rate in burst mode (up to 10 kHz), narrowband BBO OPO operation with sub-mJ (0.4 mJ) pulse energy is demonstrated using frequency tripled Nd:YAG (burst mode) as the pump source [44, 45]. This OPO system has been mainly utilized in combustion diagnostics. High repetition rate operation in this setup was achieved owing to the burst mode operation of the OPO, which effectively managed the thermal issues. Although both sub-mJ pulse energy and high repetition rates operation of such OPO was demonstrated, burst mode operation will not be suitable to applications such as laser photo-ionization spectroscopy based isotope separation which requires continuous duty-cycle operation for good yields.

An alternative route for achieving sub-mJ pulse energy, high repetition rate, continuous duty cycle operation of BBO based OPO is to reduce the pump energy threshold required to manage the overall thermal issues. Several techniques have been demonstrated to reduce the threshold pump energy using different OPO cavity configurations and pump focusing techniques [35, 40, 46-48]. Importantly, the cylindrical focusing technique [48, 49], first demonstrated by D.W. Coutts et. al [49], allows reduction of threshold pump energy with the damage-free operation of the BBO OPO. More importantly, it also increases the interaction length of the pump and the

signal waves within the parametric BBO crystal in the walk-off sensitive plane allowing efficient and sustainable output energy with continuous tuning (only limited by the d_{eff} of the interaction).

In this thesis work, we have developed and successfully demonstrated, for the first time to the best of our knowledge, high repetition rate (up to 5 kHz) operation of broad bandwidth, sub-mJ pulse energy, widely tunable (490 nm – 630 nm) Type-I phase-matched BBO based OPO. Further, by utilizing the Type-II phase-matched BBO crystal in double pass pump beam configuration [50], we have shown the high repetition rate (up to 1 kHz) operation of single longitudinal mode, sub-mJ pulse energy, widely tunable (490-590 nm) OPO. Additionally, the Type-II BBO based widely tunable narrowband OPO, developed during this thesis work, was utilized for accurate determination of attenuation coefficient (both absorption and scattering) of local seawater samples at different wavelengths in the visible region, thus enabling device specifications for underwater optical communications systems to be developed.

1.1.3 Thesis Outline

The outline of the thesis is as follows: the second part of the chapter1 presents the theory of optical parametric interactions, phase matching, factors affecting the phase matching conditions and basic principles of optical parametric oscillators. In Chapter2, we have presented the numerical calculations to realize the effect of elliptical focusing on the threshold of a nanosecond BBO-OPO pumped at 355nm. This study facilitated us to determine the optimum elliptical size of the pump beam on the BBO crystal for achieving high average power operation of these OPO's. The chapter-3 of the thesis describes the design, construction and performance characterization of a high repetition rate (5 kHz), nanosecond, 355 nm pumped, Type-I phase-matched BBO crystal based OPO. The chapter-4 describes the design, development, and characterization of narrowband high repetition rate, 355 nm pumped nanosecond BBO OPOs. Interestingly, this OPO design was

extended to achieve stable, single longitudinal mode (SLM) operation, which has been a fascinating and satisfying development work. The Chapter-5 describes the experimental studies on the effect of thermal loading inside the BBO crystal, due to high average power operation of these OPOs, on the performance of the OPO. Finally, the chapter-6 of the thesis describes in house use of such DPSSL pumped (355 nm) multi-kHz repetition rate, narrowband BBO-OPO for measuring the attenuation coefficient of various water samples including seawater in a constructed optical cell for the possible use of these data in underwater optical communication.

1.2 Theory of optical parametric interactions

It is well known that interaction of intense light with a nonlinear optical material induces a nonlinear polarization comprising of second-order and higher-order components. The second-order nonlinearity of the optical medium gives rise to the three-wave mixing processes which are SFG, SHG, and DFG. DFG also facilitates optical parametric amplification of a laser beam making the realization of OPOs possible.

In this section of this chapter, we introduce the coupled-mode equations for the three-wave mixing processes in a nonlinear crystal and give the analytical solutions for optical parametric amplification and gain. Further, we discuss how phase matching between the interacting waves improves the efficiency of these processes and the Birefringence Phase Matching (BPM) technique for achieving phase matching between the interacting waves in a nonlinear crystal. The beam walk-off effect arising due to birefringence of the crystal has been discussed in detail. In the last part of the section, we discuss the basic concept of Optical Parametric Oscillators and the time-dependent analytical formulation for calculation of threshold pump fluence in pulsed OPOs. The crystal selection criteria and the pump laser characteristics for designing efficient Visible-NIR nanosecond OPOs have been discussed.

1.2.1 Nonlinear Polarization

When electromagnetic radiation passes through a dielectric medium, the force associated with the incident electric field produces a displacement of the electrons with respect to the nuclei and induces a time-varying electronic polarization in the dielectric material. When the electric field strength of the incident radiation is small compared to the binding coulomb force of the electrons, the induced polarization in the medium is proportional to the electric field and hence oscillates with the same frequency as that of the applied field. The linearity also implies that the electromagnetic waves passing through the material do not interact with each other, or with themselves. Thus, the observed phenomenon is not dependent on light intensity. This is expressed as:

$$P = \epsilon_0 \chi^{(1)} E \quad 1.1$$

Where ϵ_0 is the permittivity of free space, $\chi^{(1)}$ is the linear susceptibility of the medium, P and E are the polarization and electric field vectors of the propagated light, respectively.

In the case where the optical electric field strength is comparable to the inter-atomic electric field, as with the laser radiation, the polarization response of the medium becomes nonlinear in the applied field. To model such a nonlinear response, the induced polarization P is customarily written as a power series expansion in the applied field E as follows:

$$P = \epsilon_o [\chi^{(1)} E + \chi^{(2)} E^2 + \chi^{(3)} E^3 + \dots] \quad 1.2$$

Where, $\chi^{(2)}$, $\chi^{(3)}$... are the nonlinear susceptibilities of the medium and the $\chi^{(m)}$ represents the susceptibility tensor of m^{th} order with the rank $(m+1)$. The magnitudes of the tensor components rapidly decrease with increasing rank of nonlinearity. For instance, the tensor magnitude ratios of $\chi^{(1)}$, $\chi^{(2)}$, $\chi^{(3)}$ are estimated to $1 : 10^{-8} : 10^{-16}$ [7]. Hence, nonlinear effects in a medium are only

observable when high intensity light such as lasers are employed. Almost all the linear and nonlinear optical effects of practical importance are described by the first three terms in Equation (1.2). It may be noted that $\chi^{(1)}$ is the linear susceptibility and responsible for the linear optical properties of the material such as refraction, absorption, dispersion, and birefringence of the medium.

1.2.2 Second Order Nonlinear Polarization

The second-order nonlinear susceptibility $\chi^{(2)}$ provides the parametric interaction between three electromagnetic waves and is responsible for processes such as frequency doubling, the Pockel's effect, sum and difference frequency mixing, and most importantly in the context of this work, optical parametric generation.

To show how $\chi^{(2)}$ gives rise to SHG, SFG and other nonlinear effects, consider an applied field E incident on the nonlinear medium,

$$E = E_1 \cos(k_1 z - \omega_1 t) + E_2 \cos(k_2 z - \omega_2 t) \quad 1.3$$

The second-order nonlinear polarization $P_{NL} = \epsilon_0 \chi^{(2)} E^2$ giving,

$$\begin{aligned} P_{NL} = & \frac{1}{2} \epsilon_0 \chi^{(2)} E_1^2 [1 + 2 \cos 2[k_1 z - \omega_1 t]] + \frac{1}{2} \epsilon_0 \chi^{(2)} E_2^2 [1 + 2 \cos 2[k_2 z - \omega_2 t]] \\ & + \epsilon_0 \chi^{(2)} E_1 E_2 [\cos[(k_1 + k_2)z - (\omega_1 + \omega_2)t] \\ & + \cos[(k_1 - k_2)z - (\omega_1 - \omega_2)t]] \end{aligned} \quad 1.4$$

the first two terms describe the dc rectification and second harmonic generation and the third and fourth terms describe sum-frequency and difference-frequency generation. Obviously, all of the above processes take place simultaneously in the nonlinear medium. The phase matching of the nonlinear interactions selects the process of interest to the exclusion of the other possible process.

The second-order nonlinear tensor, $\chi^{(2)}$ is most often replaced with d-tensor. The relation between the tensors is $\chi_{ijk}^{(2)} = 2d_{ijk}$, the d-tensor, in general, has 27 components. However, because of crystal symmetry, many of these components vanish, so that the total numbers of independent components, generally, are fewer. Some media such as gases, liquids, and amorphous solids have inversion symmetry and $\chi^{(2)}$ vanishes for such media, hence they cannot produce second-order nonlinear interactions. Thus, isotropic media and Centro-symmetrical crystals cannot be used to generate second-order nonlinear effects.

At this point, it is worthwhile to note that the third-order nonlinear susceptibility $\chi^{(3)}$ is responsible for the phenomenon of frequency tripling, the Kerr effect, Raman and Brillouin scattering, etc. Numerous texts and review articles on $\chi^{(2)}$ processes and higher-order nonlinear effects can be found in the literature [51-53].

1.2.3 Optical Parametric Generation

Optical parametric generation is the key process for generating the new extended frequencies of interest. In optical parametric generation [8, 9, 17, 20, 51-54], intense laser light at frequency ω_p interacts with the anisotropic crystal, and through the second-order nonlinear polarization, produces two new fields at smaller frequencies, ω_s , and ω_i referred as the signal and idler waves, respectively. In the photon domain, as schematically shown in the Fig.1.4, the process is equivalent to the spontaneous break-up of high-energy pump photons into two constituents of lower energy (termed signal and idler), subject to the conservation of energy. The sum of energies of the constituent photons must equal the pump photon energy.

$$\omega_p = \omega_s + \omega_i \quad 1.5$$

The phase-matching condition selects the signal and idler wavelengths pair for amplification from the infinite range of possible signal and idler pairs, satisfying energy

conservation. The phase-matching condition corresponds to the momentum conservation, which is expressed in terms of wave vectors (k) as,

$$k_p = k_s + k_i \quad 1.6$$

The above equation provides a wavelength-tuning mechanism for parametric devices. For a given pump frequency and propagation direction, tuning can be achieved by altering the refractive indices of the medium along the direction of propagation through rotation of (angle-tuning) or by changing the temperature (temperature tuning) of the non-linear crystal.

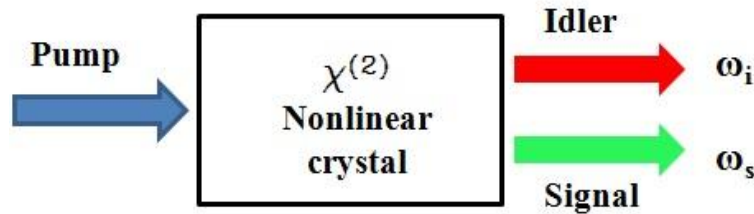


Fig.1.4: Optical parametric generation in which a pump photon of frequency ω_p splits into two photons of frequency ω_s (signal) and ω_i (idler)

1.2.4 Coupled Wave Equations

The equations governing the parametric interactions between the signal, idler and pump waves propagating in an anisotropic nonlinear medium are derived by using Maxwell's equations and briefly described below. The Maxwell's equation for a non-absorbing, non-conducting dielectric medium containing no free charge propagating along the z-axis, is given by

$$\nabla^2 E - \mu_0 \epsilon_0 \frac{\partial^2 E}{\partial t^2} = \mu_0 \frac{\partial^2 P_{NL}}{\partial t^2} \quad 1.7$$

where μ_0 is the permeability constant of vacuum and P_{NL} is the second-order nonlinear polarization given by, $P_{NL} = \epsilon_0 \chi^{(2)} E^2$ and the Fourier components of the interacting fields in the Equation (1.7) are defined as,

$$E_m(z, t) = \frac{1}{2} [E_m(z) \exp(kz - \omega t) + c. c.] \quad 1.8$$

where $m = s, i, p$ and $E_m(z)$ represents the complex field amplitude. Since the parametric process involves the interaction of three electric fields, the total field E will comprise of three waves representing the pump, signal, and idler, so that,

$$E = E_s(\omega_s) + E_i(\omega_i) + E_p(\omega_p) \quad 1.9$$

By substituting Equation (1.9), and using equation (1.8), into the wave equation (1.7), the parametric process is modeled by separating the resultant equation into three components at three different frequencies, ω_s, ω_i and ω_p , each of which must satisfy separately the wave equation. Then, by considering the three separate wave equations at each frequency and assuming that the field amplitudes vary slowly over distances compared to a wavelength, one obtains the variations of the three field amplitudes with propagation as [8],

$$\frac{dE_s(z)}{dz} = i k_s E_p(z) E_i^*(z) \exp(i\Delta kz) \quad 1.10$$

$$\frac{dE_i(z)}{dz} = i k_i E_p(z) E_s^*(z) \exp(i\Delta kz) \quad 1.11$$

$$\frac{dE_p^*(z)}{dz} = -i k_p E_s^*(z) E_i^*(z) \exp(i\Delta kz) \quad 1.12$$

The interaction coefficient k_m is defined as, $k_m = \frac{\omega_m d_{eff}}{n_m c}$ and $m = s, i, p$ where d_{eff} is the effective nonlinear coefficient, n_m is the refractive index of the nonlinear crystal at angular frequency ω_m for the signal, idler and pump waves and c is the velocity of light. Δk defines wave vector mismatch or deviation from phase-matching condition. The above Equations (1.10) to

(1.12) are coupled to one another through second-order nonlinear susceptibility $\chi^{(2)}$. These coupled wave equations are responsible for the parametric interaction of the three fields, pump, signal and idler, and are the basis for many observed nonlinear optical phenomena including SHG, SFG and Optical Parametric Generation (OPG).

In the parametric generation process, the relative phase of these fields is maintained such that the $\Delta k = 0$, in that case, the generated fields at ω_i and ω_s experience maximum growth, while the power in the input pump field at ω_p is gradually drained with propagation through the medium.

Multiplying the above Equations (1.10) to (1.12) successively, we obtain

$$\left(\frac{nc\varepsilon_0}{2}\right)\frac{E_s^*}{\omega_s}, \quad \left(\frac{nc\varepsilon_0}{2}\right)\frac{E_i^*}{\omega_i} \text{ and } \left(\frac{nc\varepsilon_0}{2}\right)\frac{E_p}{\omega_p} \quad 1.13$$

It may be noted that the right-hand sides of each equation are equal so that,

$$\frac{1}{\omega_s} \frac{dI_s}{dz} = \frac{1}{\omega_i} \frac{dI_i}{dz} = -\frac{1}{\omega_p} \frac{dI_p}{dz} \quad 1.14$$

where I_j is the intensity of the corresponding fields. These are the Manley-Rowe relations [55]. It simply states that parametric generation splits one pump photon into two photons which satisfy conservation of energy at every point in the nonlinear crystal.

1.2.5 Optical Parametric Amplifications and Gain

The above coupled Equations (1.10-1.12) are used to determine the parametric amplification and gain. In the parametric interaction process a strong pump field at frequency ω_p which is provided by a laser, mixes through the second-order nonlinear susceptibility ($\chi^{(2)}$), with a signal field at ω_s to give rise to an idler field at $\omega_i = \omega_p - \omega_s$. The idler field so generated in turn mixes back with the pump to produce an additional signal. The re-generated signal re-mixes with the pump to produce more idler. Under suitable phase-matching condition, the process can

continue in this way until power can be gradually transferred from the strong pump to initially generated weak signal and idler fields.

In the absence of a coherent source of signal and idler beams at the input, the initial supply of photons at ω_s , and ω_i for mixing with the input pump is provided by the spontaneous break up of pump photons through spontaneous parametric fluorescence. This process also referred to as parametric noise or parametric luminescence, may be viewed as to arise from the zero-point fluctuation of the electromagnetic field at the signal and idler frequencies [56, 57].

The gain and amplification factor for the growth of signal and idler fields are obtained by solving the coupled Equations (1.10) to (1.12). The general solution is described in the literature [15]. However, the simplified analytical solution to the coupled equations can be obtained by the assumption that the pump beam does not undergo strong depletion with propagation through the medium then, $dE_p/dz = 0$, in Equation (1.10). Under this approximation by solving the coupled equations, we can obtain the single-pass fractional intensity gain $G(l)$ at ω_s , (or ω_i), given by,

$$G_s(l) = \frac{I_s(z=l)}{I_s(z=0)} - 1 = g^2 l^2 \frac{\sinh^2 [g^2 l^2 - (\frac{\Delta k l}{2})^2]^{\frac{1}{2}}}{[g^2 l^2 - (\frac{\Delta k l}{2})^2]} \quad 1.15$$

where l is the length of the OPO crystal, and g is the parametric gain coefficient defined as,

$$g = \sqrt{KI_p} \quad 1.16$$

where I_p is the pump intensity and K is a coupling coefficient,

$$K = \frac{2\omega_s\omega_i d_{eff}^2}{n_s n_i n_p \epsilon_0 c^3} \quad 1.17$$

It can be seen from equation (1.12) and (1.13), that the magnitude of parametric gain depends on the pump intensity, interaction length, and nonlinear coefficient, as well as on the frequencies and refractive indices of the interacting fields. The parametric amplification is strongly dependent on phase mismatch parameter Δk . For $\Delta k = 0$, the generated fields experience maximum

gain, whereas the growth of parametric waves is severely limited by an increase in the magnitude of Δk . In practice, therefore, it is imperative to ensure maximum gain of the parametric waves by setting $\Delta k = 0$. This is achieved through the technique of phase matching, as discussed in more detail in the next section.

Parametric devices often operate under different gain conditions, depending on the magnitude of gain coefficient g . In the low-gain regime, $gl \leq 1$, corresponds to parametric generation when using CW or low peak power pulsed pump sources, Equation (1.15) can be simplified to

$$G_s = g^2 l^2 \text{sinc}^2\left(\frac{\Delta k l}{2}\right) \quad 1.18$$

This regime is pertinent to most parametric devices. On the other hand, in the high gain regime, $gl \gg 1$, corresponds to pumping with high intensity pulsed laser sources, Equation (1.17) can be approximated as

$$G_s = \left[1 + \left(\frac{\Delta k l}{2g_{eff}} \right)^2 \right] \sinh^2 g_{eff} l \quad 1.20$$

Where, $g_{eff} = [g^2 - \left(\frac{\Delta k}{2}\right)^2]^{\frac{1}{2}}$ and when $(\Delta k/2) < g$,

$$G_s \approx \frac{1}{4} \exp(2gl) \quad 1.20$$

From the above equations (1.15), (1.19) and (1.20), under phase-matching condition, the single-pass power gain has a quadratic dependence on interaction length l in the low-gain limit, whereas, it increases exponentially with interaction length in the high-gain limit.

1.2.6 Phase matching

Equation (1.15) illustrates that for attaining maximum gain in a parametric amplifier, the quantity Δkl must be zero. Since length (l) of the parametric crystal is finite, this condition implies that the Δk term must be set to zero.

$$\Delta k = k_p - k_s - k_i = 0 \quad 1.21$$

The above equation can be expressed as

$$n_p \omega_p - n_s \omega_s - n_i \omega_i = 0 \quad 1.22$$

However, this is not often possible, because of material dispersion. The optical fields at different frequencies (ω) cannot generally travel with the same phase velocity and maintain temporal synchronization during propagation through the material. The extent of loss of phase velocity synchronism among the pump, signal, and the idler is determined by the phase-mismatch parameter, Δk . Under normal conditions, $\Delta k \neq 0$, so that the optical waves at different frequencies slip out of phase after traveling a short distance through the medium. This distance is known as coherence length, L_c , and is given by [7]

$$L_c = \frac{\pi}{\Delta k} \quad 1.23$$

With propagation beyond a coherence length, the intensities of the generated waves at signal and idler gradually fall back to zero with back conversion to the pump wave. With further propagation, the waves step in and out of phase periodically, with a period determined by the coherence length. The coherence length is thus a measure of maximum interaction length over which the amplification of parametric fields would be significant. Typical values of coherence length are a few tens of microns in most nonlinear optical materials.

Understandably, for any meaningful growth of the parametric waves, phase velocity synchronism must be maintained over crystal interaction lengths, which are significantly longer than the coherence length. In fact, in order to exploit the full length of a nonlinear crystal, phase velocity synchronism must be maintained over a distance comparable or longer than the crystal length. Satisfying phase-matching condition, $\Delta k = 0$, allows the coherence length to become infinitely long. Under this condition, the signal and idler fields undergo amplification over the full interaction length of a crystal, draining power from the pump coherently and thus a large output can be extracted at the signal (ω_s) and idler (ω_i).

In practice, birefringent crystal is used for achieving phase matching in general to offset the effect of dispersion [13, 20]. The birefringent Phase Matching (BPM) technique is briefly described in the following section of this chapter. However, other methods such as Quasi Phase Matching (QPM) in which, the orientation of the electric dipoles is periodically reversed by 180° along the pump propagation direction may also be used to achieve phase matching. A full analysis of QPM is found in the literature [21, 58]. Many of nonlinear optical design characteristics of BPM and QPM are accessible through the SNLO software developed by Smith [59].

1.2.7 Birefringent Phase Matching

The practical technique for satisfying phase-matching condition, $\Delta k = 0$, is to use the birefringence of optically anisotropic media to offset material dispersion. In such media, the refractive index of the wave (and hence the magnitude of wave vector) traveling through the medium not only depends on its frequency but also on the direction of propagation, as well as, on its state of polarization. Therefore, by judicious choice of polarization states and crystal orientation, it is possible to maintain phase matching at every point along the direction of

propagation for the particular combination of frequencies ($\omega_s, \omega_i, \omega_p$). This technique is known as a birefringent phase matching (BPM) [7, 9, 53, 60].

With regard to their optical properties, birefringent crystals can be classified as uniaxial or biaxial. The optical characteristics of such crystals are often described in terms of a three-dimensional index surface called the optical indicatrix. The principal axes of this surface are defined by three principal refractive indices n_x, n_y and n_z . In uniaxial crystals, $n_x = n_y \neq n_z$, so that the optical indicatrix is an ellipsoid of revolution around the z-axis. Whereas in biaxial crystals $n_x \neq n_y \neq n_z$ and the optical indicatrix is an ellipsoid with three unequal axes. In uniaxial crystals, there exists a unique direction along which all polarization states experience the same refractive index. In biaxial crystals, two such directions are identified. These directions define the optic axes of the crystal. The complete description of the phase-matching process in biaxial crystals is given by Hobden [61].

In uniaxial crystals, it is customary to define the principal axes of the indicatrix in terms of ordinary and extraordinary indices n_o and n_e , instead of n_x (or n_y) and n_z . A light beam whose polarization is normal to the optic axis is called ordinary wave, or o-wave, while a beam-polarized parallel to the optic axis is known as an extraordinary wave or e-wave. The ordinary wave experiences the same refractive index regardless of the direction of propagation in the medium ($n_o(\theta) = n_o$). Whereas, for the extraordinary wave, the refractive index, n_e , varies from n_o to n_e as θ varies from 0° to 90° according to

$$\frac{1}{n_e(\theta)^2} = \frac{\cos^2\theta}{n_o^2} + \frac{\sin^2\theta}{n_e^2} \quad 1.24$$

Further, there are two classes of uniaxial crystals, positive uniaxial crystals for which $n_e > n_o$ and negative uniaxial crystals for which $n_e < n_o$. The general procedures for determining the

locus of phase-matching directions for three-wave interactions have been outlined by Dmitriev et.al [60].

In negative uniaxial crystals (ex. BBO crystal), phase matching can be achieved for an extraordinary pump with either one or both of the signal and idler being ordinary waves. The case when the signal and idler are both ordinary waves is referred to as type-I phase matching; when either is extraordinary it is referred to as type-II or orthogonal phase matching. In the positive uniaxial crystal, the pump must be an ordinary wave and either or both of the signal and idler extraordinary waves giving rise to type-II or type-I phase matching, respectively. The choice of the type of phase matching depends on the values of its refractive indices, the strength of its birefringence and the particular combination of frequencies involved. The possible birefringent phase-matching schemes and corresponding field polarizations for the parametric generation of $\omega_p \rightarrow \omega_s + \omega_i$ in uniaxial crystals are described in the Table. 1.1.

Table 1.1: Possible birefringent phase matching schemes and corresponding field polarizations for parametric generation in uniaxial crystals.

Crystal Class	$\omega_p \rightarrow \omega_s + \omega_i$			
	Positive Uniaxial		Negative Uniaxial	
Phase-matching scheme	Type I	Type II	Type I	Type II
Field polarizations	$E_o \rightarrow E_e + E_e$	$E_o \rightarrow E_o + E_e$	$E_e \rightarrow E_o + E_o$	$E_e \rightarrow E_o + E_e$
		$E_o \rightarrow E_e + E_o$		$E_o \rightarrow E_e + E_o$

Moreover, when the propagation direction is along one of the principal axes of the indicatrix, the phase matching is termed as non-critical (NCPM), while for any other direction it

is referred to as critical phase matching (CPM). The advantage of non-critical phase matching is discussed in the following sections of this chapter.

1.2.8 Parameters affecting the phase-matching condition

In practice, the perfect phase matching, $\Delta k = 0$ is not possible because of the finite divergence, spectral bandwidth and temperature bandwidth of pump radiation contribute to a nonzero Δk . Owing to the dependence of the refractive indices on angle, temperature, and wavelength, any change of these parameters will cause a deviation from the exact phase-matching condition. The phase-matching condition is now a function of angle, temperature, and wavelength, i.e., $\Delta k = \Delta k(\theta, T, \lambda)$.

The increase in the magnitude of Δk arising from the finite bandwidth, spectral bandwidth and temperature bandwidth of the coupled equations can be approximated as given by Equation (1.25), by taking the first-order derivatives of phase mismatch Δk expanded in Taylor series at the point of phase-matching angle (θ_m), frequency (ω_m) and temperature (T_m),

$$\Delta k \approx \frac{\partial(\Delta k)}{\partial \theta} \Delta \theta + \frac{\partial(\Delta k)}{\partial \omega} \Delta \omega + \frac{\partial(\Delta k)}{\partial T} \Delta T \quad 1.25$$

The acceptance bandwidths of the crystal are a measure of maximum angular, spectral and temperature deviations that can be tolerated for a given crystal length before parametric gain is reduced to one half of its peak value at $\Delta k = 0$. Therefore, by setting $\Delta k = \pm \pi/l$, the acceptance bandwidths of angle ($\Delta \theta$), frequency ($\Delta \omega$) and temperature (ΔT) is calculated.

The magnitude of these bandwidths will depend upon the type of phase matching employed, and type of crystal used i.e. either Type I or Type II. The expressions for calculating bandwidths for the full range of phase-matching schemes are given in reference [60].

For attaining maximum gain of the parametric process, it is desirable to use phase-matching configurations and non-linear crystals that yield large acceptance bandwidths. For example, in the case of non-critical phase-matching (NCPM) configuration, the phase-matching process ensures large angular acceptance bandwidths.

At the same time, it is also important to use diffraction-limited pump laser beams with low divergence and narrow spectral width to avoid the phase mismatch effects due to angular and spectral bandwidths. The temperature gradients arising due to the absorption of the pump beam in the crystals will change the refractive index. As a result of the change in the refractive index, the phase-matching condition will alter during the parametric interaction process. Consequently, efficiency will reduce. The sensitivity of the phase-matching condition with the temperature change ($\partial\Delta k/\partial T$) in the Equation (1.25) defines the acceptable temperature bandwidth for the particular phase-matching condition.

1.2.9 Walk-off effects

In a birefringent crystal, the direction of wave propagation (i.e., wave vector k) for an extraordinary wave is not generally the same as the direction of energy (Poynting vector, $S = E \times H$) propagation. The direction of Poynting vector S is normal to the direction of the tangent drawn at the point of intersection of the wave vector k , with the index surface as shown in the Fig. 1.5. For an ordinary wave, the surface of the index is a sphere with radius n_0 . Therefore, the direction of the Poynting vector S coincides with the wave vector k . For an extraordinary wave, the surface of the index of refraction, $n_e(\theta)$, is an ellipsoid. Therefore, the pointing vector S and wave vector does not coincide (except at $\theta = 0$ and $\theta = 90^\circ$) but makes a small angle ρ known as the walk-off

angle. The Fig.1.5 illustrates the disposition of Poynting vector S and wave vector k in anisotropic and anisotropic medium.

In a uniaxial crystal, the walk-off angle (ρ) is given by [61],

$$\rho = \pm \tan^{-1} \left[\left(\frac{n_o}{n_e} \right)^2 \tan \theta \right] \mp \theta \quad 1.26$$

where the upper sign corresponds to a negative crystal and the lower sign to a positive crystal. Thus, for both type I and type II phase matching processes, the ordinary and extraordinary beams of finite size will not completely overlap over the full length of the nonlinear medium. The extraordinary pump beam in case of Type-I phase-matching completely separates from the parametric signal wave generated at the crystal entrance at a distance called the aperture length, which is given by,

$$l_a = \frac{a}{\rho} \quad 1.27$$

where 'a' is the beam diameter and ' ρ ' is the walk-off angle.

For a weakly focused Gaussian beam, the aperture length is given by [62],

$$l_a = \frac{\sqrt{\pi}}{\rho} \omega_p \quad 1.28$$

where ω_p is the pump beam radius. Although perfect phase matching is maintained between the interacting beams, the walk-off effects can severely limit the maximum useful crystal length over which parametric generation can efficiently extract power from the pump beam.

The deleterious effects of walk-off can be largely avoided by the use of a large beam diameter or by employing NCPM geometry where the beam is propagating along one of the principal index axes of the crystal. In these directions, the crystal does not show birefringence. Other strategies to compensate walk-off include using two crystals oriented in a walk-off

compensated configuration [63], and cylindrical focusing of the pump beam [64]. Further details of these techniques in the context of this dissertation work will be discussed in Chapter 4.

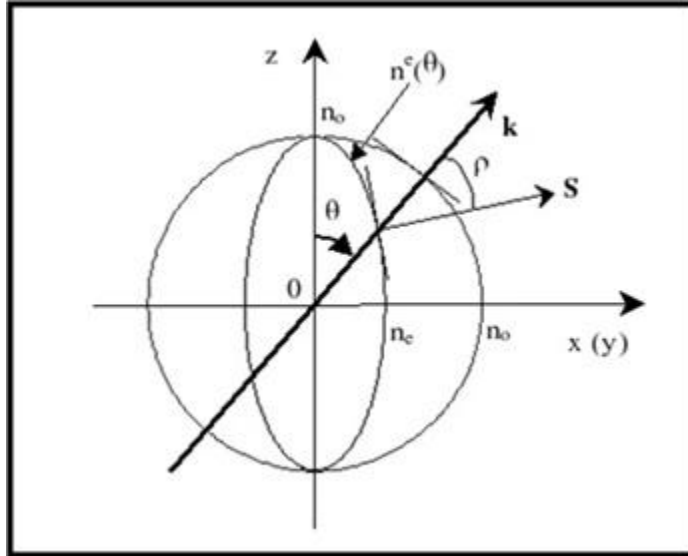


Fig.1.5: The walk-of angle ρ between the wave vector k and the Poynting vector S in a negative birefringent BBO crystal

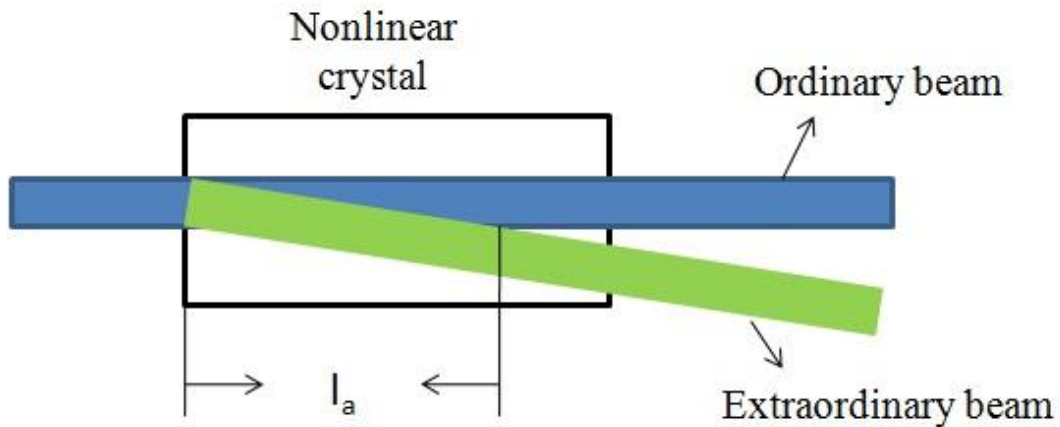


Fig.1.6: Schematic illustration of the walk-off effect of ordinary and extraordinary waves

1.3 Optical Parametric Oscillators (OPOs)

The optical gain of parametrically generated waves when an intense beam is incident on the crystal (discussed in section 1.1) can be increased by providing positive feedback, which is achieved by placing the nonlinear crystal in a two-mirror resonator. When the optical parametric gain of the resonator exceeds its optical loss, oscillation occurs. Such a device is called an optical parametric oscillator (OPO). The schematic of the OPO is illustrated in the Fig. 1.1. Above the threshold for oscillation, the signal and idler waves grow dramatically at the expense of pump power. The output of such a device is coherent radiation like that of a laser.

There are two types of OPOs characterized by the form of feedback. If the end mirrors of this device are highly reflecting at both frequencies of signal (ω_s) and idler (ω_i), the device is known as a doubly resonant oscillator (DRO) and if the end mirrors are highly reflecting at either signal frequency (ω_s) or idler (ω_i) frequency, but not at both, the device is known as a singly resonant oscillator (SRO) usually, both mirrors are transparent to the pump wave.

The operation characteristics of these DRO and SRO configurations have been discussed in detail in [8, 9]. The steady-state oscillation threshold analysis of these two types of OPO configurations shows that SRO configuration exhibits much higher oscillation thresholds than that of DRO configuration. Hence, for all practical purposes, the SROs are pumped with high peak power pulsed pump sources. On the other hand, the operation of DROs can be attained by using CW and pulsed pump lasers with modest power levels. However, the major drawbacks of DROs are the inherent amplitude and frequency instabilities and tuning difficulties imposed by the double resonance condition and the requirement for stringent control of the pump laser frequency and oscillator cavity length. Because of these practical difficulties of DROs, the singly resonant OPOs are preferred in practice even though, they exhibit much higher thresholds.

Wavelength tuning of these singly resonant OPOs can be achieved by either changing the pump wavelength or phase-matching properties of the nonlinear optical crystal. Generally, pump wavelength is fixed and the latter condition is accomplished by changing the temperature or orientation of the non-linear crystal or grating period in quasi-phase matching process. The change in the crystal orientation or temperature alters the refractive index around the phase matching condition that will change the signal and idler wavelengths such that a new phase-matching condition is set. Tuning curves for parametric oscillators can be determined by solving the phase-matching equations (1.21, 1.22) for signal and idler frequencies at a given pump frequency as a function of the tuning variable. The wavelength tuning curve of a BBO-OPO, obtained by varying the orientation of a Type-I phase-matched BBO crystal pumped at 355 nm, is shown in the Fig. 1.7 [65].

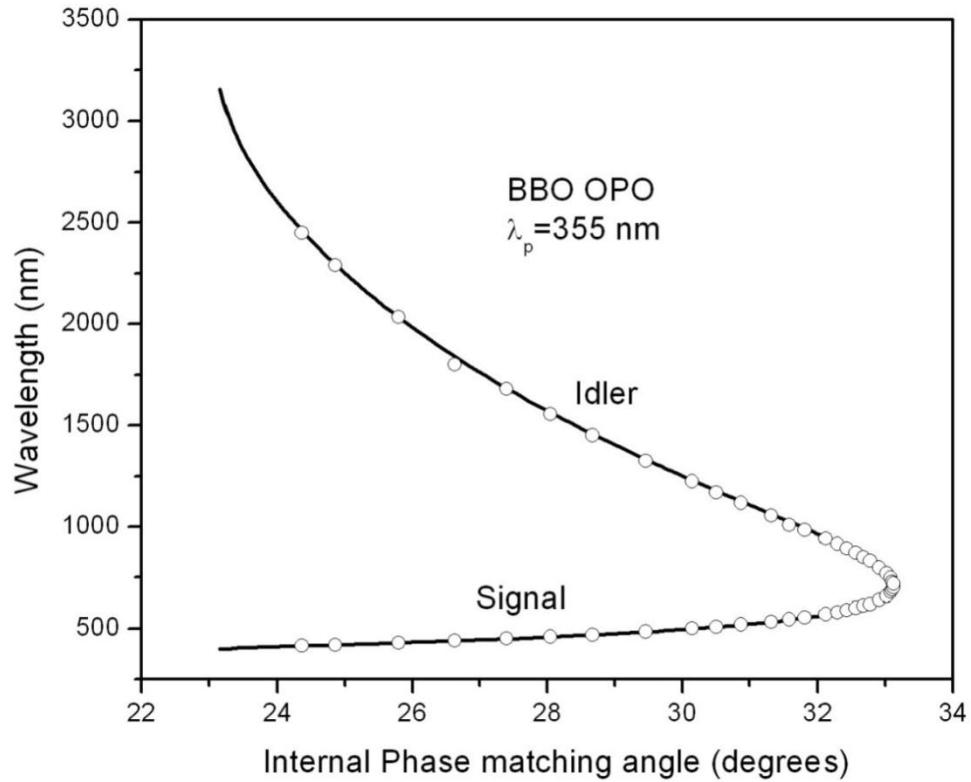


Fig.1.7: Angle tuning curve of BBO-OPO pumped at 355 nm, with type-I interaction. The solid curve represents the calculated wavelengths, while circles give the experimentally measured values [65].

1.3.1 Threshold of a nanosecond OPOs

Singly resonant OPOs are usually pumped with the output from a Q-switched Nd:YAG laser at either the fundamental 1.06 μm or its any harmonics, depending on the desired output wavelengths range and nonlinear material. Because of the transient nature of pulse pumping, coherent amplification of parametric waves has to occur in the presence of the pump and no gain is available outside the temporal window of the pump pulse. Given the finite duration of the pump pulse, only a limited number of round-trips of parametric waves can be made available through the nonlinear crystal in OPO cavities of practical length, thus inhibiting the establishment of steady-state conditions. Therefore, the steady-state threshold analysis of CW OPO is not applicable for a pulsed OPO operating in the nanosecond temporal regime.

A time-dependent gain model which calculates the threshold pump energy fluence (energy/area) of a pulsed singly resonant oscillator was described by Bronson and Byer [66]. This model assumes a Gaussian temporal profile and a Gaussian spatial distribution for the pump and the resonant signal, with an idler wave that is unconstrained by the optical cavity. The effects of spatial walk-off and mode overlap are included in the model.

In this model, the generated signal wave is assumed to be amplified as it makes consecutive transits through the optical cavity. The oscillation threshold is defined as pulse energy of pump at which the signal energy (after m round-trips) has reached 100 μJ , corresponding to a ratio of signal power (P_m) to parametric noise power (P_n) of, $\ln(P_m/P_n) = 33$. The threshold fluence for the SRO is given by [66]

$$J_{th} \cong \frac{2.25}{Kg_s I_{eff}^2} \tau \left[\frac{L}{2\tau c} \ln \frac{P_m}{P_n} + 2\alpha l + \ln \frac{1}{\sqrt{R}} + \ln 2 \right]^2 \quad 1.29$$

where τ is the $(1/e^2)$ intensity half-width of the pump pulse, L is the cavity length, l is the length of the crystal, α is the signal field loss coefficient, R is the cavity mirror reflectivity at the signal wavelength.

The coupling coefficient K is related to the parametric gain coefficient that has been previously defined in (1.17), and g_s is the signal spatial mode coupling coefficient describing the mode overlap between the resonant signal and pump field. It is defined by,

$$g_s = \frac{w_p^2}{w_p^2 + w_s^2} \quad 1.29$$

where w_p and w_s are the Gaussian mode radii of the pump and signal, respectively. The effective parametric gain length l_{eff} is determined by the walk-off length,

$$l_{eff} = \frac{\sqrt{\pi}\omega_p}{2\rho} \quad 1.30$$

where ρ is the double refraction walk-off angle. The walk-off length is closely related to the aperture length introduced in Equation.1.28. For attaining maximum efficiency, the beam diameter must be increased until the effective walk-off length is equal or greater to the crystal length.

The first term in the square bracket represents the effective loss due to build-up time during pulsed operation. This is a measure of time required for the parametric gain to build up from noise to oscillation threshold [66]. Hence, it is essential that the OPO rise time should be minimized so that parametric waves are rapidly amplified above the threshold level in a time significantly shorter than the pump pulse temporal width. In practice, this can be achieved by minimizing cavity length to allow a larger number of round trips over the pump pulse interval.

The second and third terms describe the increase in threshold due to absorption losses and the cavity output coupling loss. Lowering the intra-cavity losses α and maximizing R can further reduce the threshold. The final term $\ln 2$ is due to the SRO operation. The threshold fluence is

inversely proportional to K , which means that the threshold is proportional to the inverse of the square of d_{eff} . Therefore, the choice of the crystal with large d_{eff} is important for low threshold operation of these OPOs.

1.3.2 Nonlinear Crystals Selection

The choice of the right nonlinear crystal is very important for designing efficient optical parametric devices. These nonlinear crystals must be transparent to the pump as well as the signal and idler wavelengths and free from impurities and exhibit low absorption and scattering losses at these wavelengths. Other material requirements include a good optical homogeneity, mechanical hardness, chemical stability, non-hygroscopic, and available in bulk form and sufficiently large size. For efficient operation of this device, it is desirable to use nonlinear crystals which offer favorable phase matching geometries with large d_{eff} coefficient and exhibit large spectral, angular and temperature acceptance bandwidth and small double refraction walk-off angle.

In practice, a very important consideration in the choice of suitable crystal for reliable operation of high average power OPO is a high optical damage threshold. In general, attainment of operation threshold in OPOs requires high pump intensities of typically tens of MW/cm^2 . Hence, the nonlinear crystal must withstand the power densities of 5-10 times these values for efficient conversion.

The nonlinear crystals which are commonly employed in OPOs operating at different wavelength regimes are summarized in Table 1.2. For OPOs operating in UV, visible or near-infrared, BBO and LBO are the best materials because of their transparency range, which extends to very short wavelength [7, 25, 60, 67, 68]. While the effective nonlinear coefficient of LBO (~ 1 pm/V) is considerably lower than BBO (~ 2 pm/V), its capability for non-critical phase-matching (NCPM), and small walk-off angle, has enabled the development of high repetition rate OPOs,

pumped by the second harmonic of a Q-switched diode pump solid-state lasers [69]. A detailed comparison of BBO and LBO has been provided in reference [70].

KTP is the material of choice for the design of OPOs pumped with Nd: YAG lasers at 1.06 μm and tunable from 1.6 μm to 3.4 μm [71]. OPOs based on other nonlinear crystals such as Potassium Niobate (KNB) and Potassium Titynal Arsenate (KTA) have also been developed using a variety of phase matching and pumping configurations, particularly in the difficult spectral range from 3 μm to 5 μm [71]. The optical, mechanical and phase-matching properties of these nonlinear crystals are available in [59,72]

At wavelength longer than 4 μm , there are no materials suitable for conversion from the established Nd: YAG lasers. The main problem is lack of transparency. Pumping of OPOs for the generation of mid-infrared radiation has to be done at wavelengths longer than 2 μm . The materials AgGaSe₂ and AgGaS₂ that were used in early experiments for generating wavelength beyond 4 μm suffer from low damage threshold and poor thermal conductivity [72]. One of the most promising long-wave infrared materials is ZnGeP₂ (ZGP). ZGP exhibits high optical nonlinearity, high thermal conductivity, and high damage threshold. One of the remarkable breakthroughs in mid-IR technology was the demonstration of broadband ZGP-OPO with average output power more than 10 W at 3-5 μm and more than 50 % efficiency [71]. The OPO was pumped with a 20 W diode-pumped, Q-switched (10kHz, 11ns) Ho:YLF laser operating at 2.05 μm . Later, an impressive tuning range from 3.8 μm to 12.4 μm was demonstrated in a ZGP-OPO, pumped by pulsed Er:YAG laser at 2.9 μm [73].

The periodically poled crystals such as PPLN and PPKTP with large effective nonlinearity and long interaction lengths (up to 60 mm in PPLN) has enabled the realization of pulsed OPOs operating in the range from 1.5 μm to 5 μm at considerably lower pump pulse energies. A more

comprehensive survey of birefringent and periodically poled nonlinear materials can be found in reference [9].

Table 1.2: Properties of the selected nonlinear crystals commonly employed in OPOs.

Nonlinear material	Transmission range (μm)	Pump Wavelength (μm)	Realized Tuning range(μm)	Nonlinear Coefficient (pm/V)	Optical Damage threshold (GW/cm^2)
BBO (BaB_2O_4)	0.19-3.1	0.266	0.3-2.5	2	5
		0.355	0.41-2.5		
		0.532	0.67-2.5		
LBO (LiB_3O_5)	0.16-3.0	0.355	0.41-2.5	1.2	~ 10
KTP (KTiOPO_4)	0.35-4.0	0.532	0.61-4	3.18	~ 1.0
		1.064	0.14-4.0		
KNB (KNbO_3)	0.35-4.5	1.064	1.4-4.2	10.2	1.2
LNB (LiNbO_3)	0.35-4.3	0.532	0.6-4.2	5	0.20
		1.064	1.42-0.42		
AgGaS ₂	0.8-9.0	1.064	1.2-9.0	15	0.040
		2.050	2.6-9.0		
AgGaSe ₂	1-15	2.050	2.5-9.0	20	0.040
ZnGeP ₂	0.74-12	2.800	3.9-12.4	75	1
CdSe	0.75-25	2.800	3.57-13.0	18	0.040
GaSe	0.62-20	2.800	3.3-19.0	54	0.040

1.3.3 Pump Laser Considerations

The properties of the pump laser are of great importance in designing an OPO device. The pump laser dramatically affects the performance of the OPO, much more so than with other tunable

laser sources. The spatial profiles, spectral bandwidth, pointing stability, divergence, and temporal pulse width and pulse shape of the pump laser, all play important roles.

The smooth spatial profile of the pump beam is essential because hot spots in the beam can damage the nonlinear crystal. Current Q-switched Nd:YAG lasers offer two types of beams, either an approximation to a Gaussian or an approximation to a flat-top. Either profile is adequate for OPO pumping; the important requirement is an unstructured smooth profile at the crystal. For narrowband OPOs, a temporally modulated pump profile will also modulate signal thereby broadening the spectrum of output.

The output wavelengths are functions of the angle made between the pump wave vector and the optic axis. If the pointing stability of the pump laser is poor, then this angle changes on a shot to shot basis and so does the output wavelength. Pointing stability of 100 μrad is needed to keep the wavelength fluctuations within an acceptable level of 0.01 nm. The requirement of phase matching places further demands on pump bandwidth and divergence of the pump laser as described in the previous section.

Among several pulsed lasers, which have been used for studies on pulsed OPOs operating in the visible-near IR region, the injection seeded single-mode Q-switched Nd:YAG laser is the most suitable commercially available laser for OPO pumping.

To conclude, we have described in this introductory chapter, the theory of optical parametric interactions which has been evolved and matured due to contributions of a large number of researchers over past decades and a brief outline of the present thesis work.

Chapter 2

The effect of elliptical focusing on the threshold of a BBO crystal OPO

In this chapter, we report, the results of our numerical model developed to determine the optimum elliptical focusing parameters of the input UV (355 nm) pump beam for achieving reliable low threshold operation of a high repetition rate singly resonant nanosecond β -BaB₂O₄ (BBO) based optical parametric oscillator (OPO). The results of our analysis have facilitated to obtain a substantial reduction in the threshold of the OPO operation with the optimum elliptical focusing parameters of the pump beam. We have utilized our numerical model calculations to find out the maximum dimensions of the elliptical focused pump beam at 355 nm for which the threshold pulse energy of the Type-I BBO crystal based OPO reduces to ~ 1 mJ. This, in turn, facilitated to construct a multi-kHz repetition rate BBO crystal based OPO, pumped with the third harmonic of a DPSSL system operating with a maximum pulse energy of $\sim 2 - 2.5$ mJ, and demonstrate efficient, sustainable, optical damage-free high average power operation of the OPO. The threshold energy of the Type-I BBO OPO, excited by the pump beam at 355 nm, is calculated across its tuning range using our developed model and compared with the experimental observations.

2.1 Introduction

Several theoretical studies on the effect of pump beam focusing conditions on parametric oscillations of various non-linear crystals have been reported [66, 74,75, 76, 77, 78]. The effect of spherical focusing on the threshold and efficiency of both single resonant and double resonant OPO's based on Greens function approach has been reported by Guha.et.al [79]. This theory has been extended to elliptical focused beams by Tukker et.al [80]. They have developed a numerical model for studying the elliptical focusing effects in the presence of beam walk-off for the Difference Frequency Generation (DFG) in LiNbO₃ and AgGaS₂ crystals. The present numerical approach for calculating the spatial overlap coefficient of the OPO signal with the pump beam in our constructed OPO is based on the general theory presented by Tukker et.al [80].

It may be noted that in the pulsed operation of OPOs, coherent amplification of parametric waves has to occur in the presence of the pump beam and no parametric gain is available outside the temporal window of the pump pulse, discussed in section 1.3.1 of chapter 1. Therefore, the time-dependent theory, developed by Bronson and Byer et.al [66], has been considered in formulating the analytical expression for threshold energy of the OPO in our model. To make the model practically useful, the optical losses arising due to the OPO cavity build up time, output coupler, and intra-cavity absorptions are included for calculating the threshold pump energy. In this chapter, we present the results of numerical simulations which facilitated to determine the effect of elliptical focusing on the threshold of the OPO and in turn the optimum elliptical pump beam parameters on the Type- I phase-matched BBO crystal. This helped us in designing the low threshold, multi-kHz repetition rate operation of OPOs with improved efficiencies.

We have utilized this model analysis to find out the maximum size of the elliptical focused pump beam at 355 nm for which the threshold energy of the Type-I BBO crystal based OPO reduces to ~ 1 mJ. This in turn allows using a high repetition rate (5 kHz), third harmonic output of a commercial DPSSL system with available pulse energy of $\sim 2 - 2.5$ mJ as pump beam for OPO, while avoiding optical damage of the BBO crystal due to high optical intensities and thermal effects during its sustainable high average power operation [81].

2.2 Threshold of a nanosecond OPO under elliptical focusing

The power gain in the signal due to second-order nonlinear interaction process of the pump, signal and idler fields inside a nonlinear crystal at a signal frequency ω_s is defined as [80]

$$\Delta P_s = -\omega_s \epsilon_0 d_{eff} \text{Im} \int E_s^* E_p E_i^* dx dy dz \quad 2.1$$

Where d_{eff} is the effective nonlinear coefficient of the nonlinear crystal and E_p , E_s and E_i are electric field strengths of the pump, signal, and idler fields, respectively. In this model, we have considered the interaction of these fields as Type-I (e – o + o), where the pump electric field is propagated as extraordinary and the signal and idler as ordinary waves. The pointing vector walk-off angle ρ of the extraordinary wave is defined as the angle between the z-axis and the pointing vector in the x, z plane. The electric fields have an elliptical profile with the major axis in the x-direction and are propagating in the positive z-direction. We have assumed that both pump and generated signal beams are focused at the center of the parametric crystal. The elliptically focused pump and the resonated signal fields can be written as

$$E_p(x, y, z, t) = \tag{2.2}$$

$$\frac{E_{0p}}{\sqrt{(1+i\zeta_{px})(1+i\zeta_{py})}} \exp(i\kappa_p z) \exp(-i\omega_p t) \exp\left[\frac{-[x-\rho(z-z_c)]^2}{\vartheta_{ellipse}^2 w_{0p}^2 (1+i\zeta_{px})}\right] \exp\left[\frac{-y^2}{w_{0p}^2 (1+i\zeta_{py})}\right]$$

$$E_s(x, y, z, t) = \tag{2.3}$$

$$\frac{E_{0s}}{\sqrt{(1+i\zeta_{sx})(1+i\zeta_{sy})}} \exp(i\kappa_s z) \exp(-i\omega_s t) \exp\left[\frac{-x^2}{\vartheta_{ellipse}^2 w_{0s}^2 (1+i\zeta_{sx})}\right] \exp\left[\frac{-y^2}{w_{0s}^2 (1+i\zeta_{sy})}\right]$$

where,

$$|E_{0j}|^2 = \frac{4P_j}{\pi \vartheta_{ellipse} w_{0j}^2 \varepsilon_0 n_j c},$$

$$\zeta_{jx} = \frac{2}{b_{jx}} \left(z - \frac{l}{2}\right),$$

$$\zeta_{jy} = \frac{2}{b_{jy}} \left(z - \frac{l}{2}\right),$$

$$\vartheta_{ellipse} = \frac{w_{0x}}{w_{0y}}, \quad b_{jy} = w_{0j}^2 \kappa_j, \quad b_{jx} = \vartheta_{ellipse}^2 w_{0j}^2 \kappa_j$$

where j is either p or s , P_j is the power, w_{0j} is the beam waist size, n_j is the index of refraction, κ_j is the wave vector and $\vartheta_{ellipse}$ is the ratio of the beam radii in the x and y directions. The idler field is obtained by solving Maxwell's equation using the Green function technique and integrating over x' and y' coordinates as described in reference [80],

$$E_i(x, y, z, t) = \int_0^z K_1 \exp(i\Delta z') \exp(i\kappa_i z) \sqrt{\frac{\pi^2}{ib_x ib_y}} \exp(a_{1x} x^2 + a_{1y} y^2 + 2a_2 \rho y - a_3 \rho^2) dz' \tag{2.4}$$

where,

$$\Delta \kappa = \kappa_p - (\kappa_s + \kappa_i),$$

$$K_1 = \frac{\omega_i^2 d_{eff}}{2\pi c^2} \frac{E_{0p} E_{0s}^*}{\sqrt{(1+i\zeta'_{px})(1+i\zeta'_{py})(1-i\zeta'_{sx})(1-i\zeta'_{sy})}} \frac{1}{(z-z')},$$

$$ib_j = \frac{1}{c'_{pj}} + \frac{1}{c_{sj}^*} - \frac{i\kappa_i}{2(z-z')},$$

$$c'_{px} = \vartheta_{ellipse}^2 w_{0p}^2 \left[1 + i \frac{2}{b_{px}} \left(z' - \frac{l}{2}\right)\right],$$

$$c'_{sx} = \vartheta_{ellipse}^2 w_{0s}^2 \left[1 + i \frac{2}{b_{sx}} \left(z' - \frac{l}{2}\right)\right], c'_{py} = w_{0p}^2 \left[1 + i \frac{2}{b_{py}} \left(z' - \frac{l}{2}\right)\right]$$

$$c'_{sy} = w_{0p}^2 \left[1 + i \frac{2}{b_{sy}} \left(z' - \frac{l}{2}\right)\right], \text{ where } j \text{ is either } x \text{ or } y,$$

$$a_{1j} = \frac{i\kappa_i}{2(z-z')} - \frac{\kappa_i^2}{(z-z')^2 4ib_j},$$

$$a_2 = -\frac{2i\kappa_i \left(z' - \frac{l}{2}\right)}{4ib_y (z-z') c'_{py}},$$

$$a_3 = \left(z' - \frac{l}{2}\right)^2 \left(\frac{1}{c'_{py}} - \frac{1}{c_{py}^2 ib_y}\right).$$

The signal power gain in a single pass through the crystal is obtained by substituting Equations (2.4),(2.3) and (2.2) into Equation (2.1) and performing the integration over the x and y directions.

$$\Delta P_s = \frac{32\pi d_{eff}^2 P_p P_s l_c}{c n_p n_s n_i \varepsilon_0 \lambda_s \lambda_i} \frac{\kappa_s \kappa_p}{\kappa_s + \kappa_p} h_s \quad 2.5$$

Where l_c is the crystal length and h_s is spatial overlap coefficient defined as

$$h_s \quad 2.6$$

$$= \frac{1}{4} \frac{\kappa + 1}{\kappa \xi_s + \xi_p}$$

$$\times \text{Re} \int_0^1 \int_0^{z_2} \frac{\vartheta_{ellipse}^2 \exp[i\Delta\kappa l_c (z_2 - z_1)] \exp(-f_w \rho^2) dz_1 dz_2}{\sqrt{[(z_1 + A_{sx})(z_2 + A_{sx}^*) + C_{sx}][(z_1 + A_{sy})(z_2 + A_{sy}^*) + C_{sy}]}}$$

where,

$$A_{sy} = -\frac{1}{2} - \frac{i}{4} \left(\frac{1}{d_1} + \frac{1}{d_2} \right),$$

$$C_{sy} = -\frac{1}{16} \left(\frac{1}{d_1} - \frac{1}{d_2} \right)^2,$$

$$A_{sx} = -\frac{1}{2} - \frac{i\vartheta_{ellipse}^2}{4} \left(\frac{1}{d_1} + \frac{1}{d_2} \right),$$

$$z_1 = \frac{z'}{l_c}, \quad z_2 = \frac{z}{l_c}$$

$$C_{sx} = -\frac{\vartheta_{ellipse}^2}{16} \left(\frac{1}{d_1} - \frac{1}{d_2} \right)^2,$$

$$d_1 = \frac{\xi_s \xi_p (\kappa - 1)}{\kappa \xi_p + \xi_s}, \quad d_2 = \frac{\kappa \xi_s + \xi_p}{(\kappa - 1)},$$

$$\xi_p = \frac{l_c}{b_{py}}, \quad \xi_s = \frac{l_c}{b_{sy}},$$

$$\kappa = \frac{\kappa_p}{\kappa_s},$$

f_w is beam walk-off factor,

$$f_w = a_3^* + \frac{l_c^2 (z_2 - \frac{1}{2})^2}{c_{px}} - \frac{1}{ib_{1y}} \left[\frac{l_c (z_2 - \frac{1}{2})}{c_{px}} + a_2^* \right]^2,$$

where,

$$ib_{1j} = \frac{1}{c_{py}} + \frac{1}{c_{sj}^*} - a_{1y}^*,$$

$$c_{px} = \vartheta_{ellipse}^2 w_{0p}^2 \left[1 + i \frac{2}{b_{px}} \left(z' - \frac{l}{2} \right) \right],$$

$$c_{sx}^* = \vartheta_{ellipse}^2 w_{0s}^2 \left[1 - i \frac{2}{b_{sx}} \left(z' - \frac{l}{2} \right) \right].$$

The threshold [80] pump power is obtained by equating the signal power gain with the round trip loss of the resonator cavity. The Threshold power P_p^t ,

$$P_p^t = \frac{\varepsilon_{loss}}{K_2 h_s} \tag{2.7}$$

where, ε_{loss} is the fractional round trip loss and

$$K_2 = \frac{32 \pi d_{eff}^2 l_c}{\lambda_s \lambda_p n_p n_p n_p c \varepsilon_0} \frac{\kappa_s \kappa_p}{\kappa_s + \kappa_p}$$

For pulsed OPO operation, we have assumed that the incident pump beam electric field distribution is Gaussian in time,

$$E_p(t) = E_{0p} \exp\left(-4 \ln 2 \frac{t^2}{\tau^2}\right) \quad 2.8$$

Where τ is FWHM of the pump laser pulse. Substituting, Equation (2.8) in Equation (2.2) and integrating over time and the XY plane give the input pump pulse energy U_p [82],

$$U_p = \varepsilon_0 c n_p |E_{0p}|^2 \frac{\pi^{3/2}}{8\sqrt{\ln 2}} \vartheta_{ellipse} w_{0j}^2 \tau \quad 2.9$$

replacing the value of $|E_{0p}|^2$, $|E_{0p}|^2 = \frac{4P_p}{\pi \vartheta_{ellipse} w_{0p}^2 \varepsilon_0 n_p c}$ in the Equation (2.9) and substituting the value P_p in Equation (2.7) gives, the threshold pulse energy of the pump laser U_p^t ,

$$U_p^t = \frac{\sqrt{\pi} \tau \varepsilon_{loss}}{2\sqrt{\ln 2} K_2 h_s} \quad 2.10$$

The OPO cavity losses due to the build-up time during the pulsed operation and other losses due to the residual optical absorption in the crystal and cavity output mirror are approximated based on the time-dependent gain model developed by Brosnan and Byer et.al [66]. Substituting these loss terms in Equation (2.10), gives,

$$U_p^t = \frac{\sqrt{\pi} \tau}{2\sqrt{\ln 2} K_2 h_s} \left[\frac{15L}{\tau c} + 2\alpha l + \ln \frac{1}{\sqrt{R}} + \ln 2 \right]^2 \quad 2.11$$

where l is the length of the non-linear crystal, L is the optical length of the OPO cavity, α is the loss coefficient in the crystal and R is the overall reflectivity of the resonator end mirrors.

2.3 Numerical model: BBO OPO

The elliptical focusing effects of the pump beam at 355 nm, on the threshold of the BBO crystal based OPO, are studied by numerically evaluating the spatial overlap coefficient (h_s) of the pump and generated signal beams and the corresponding threshold energies of the OPO are calculated using Equation (2.11). These are described in the earlier section for different dimensions of the elliptical focused pump beam. The value of the h_s is calculated by integrating the Equation (2.6) with the adoptive Simpson method [83]. The numerical results of h_s are evaluated considering that BBO OPO is operating at a signal wavelength of 560 nm and the corresponding idler wavelength of 969.8 nm. The extraordinary pump beam walk-off angle is considered as 73 mrad [59] for the above interaction. We have chosen the length of the BBO crystal (l_c) as 15 mm and the beam waist size in the x-direction is $\mathcal{G}_{\text{ellipse}}$ times larger than in the y-direction. The value of h_s is maximized with respect to phase matching (Δk) and focusing parameters ξ_p . The maximum value of h_s is denoted as h_{sm} .

2.4 Numerical Results

2.4.1 Optimum elliptical focusing condition for low threshold operation of a BBO OPO

The numerical value of h_{sm} is calculated for different confocal parameter (ξ_p) values of the pump beam at different ellipticity factors ($\mathcal{G}_{\text{ellipse}}$). The Fig.2.1 shows the dependency of h_{sm} on the pump beam focusing parameter ξ_p for different values of $\mathcal{G}_{\text{ellipse}}$. For these calculations, the confocal parameters of the pump and the generated signal waves are considered identical ($\xi = \xi_p = \xi_s$). The Fig.2.1 illustrates that there exists an optimum beam spot size which corresponds to a maximum

value of h_s (h_{sm}) of the pump beam for each value of the ellipticity factor. It may be noted that the increase in the value of h_{sm} corresponds to an increase in the conversion efficiency of the nonlinear interaction process and thus optical efficiency of the OPO output. From the Fig.2.1 it is evident that even the pump beam intensity on the crystal decreases with increase in the ellipticity factor, the conversion efficiency of the parametric process rises due to the increase in the effective interaction length of the parametric pump and signal beams. It has been observed that the value of h_{sm} increases from 0.001 to 0.012 if the ellipticity factor of the pump beam is changed from $\mathcal{G}_{ellipse} = 1$ (circular) to $\mathcal{G}_{ellipse} = 25$, which corresponds to a significant increase in the parametric gain by a factor of 12.

The Fig.2.2 shows the variation of h_{sm} as a function of $\mathcal{G}_{ellipse}$ for unequal confocal parameters of ξ_p and ξ_s . In this plot, h_s is maximized with respect to the focusing parameters ξ_p and ξ_s . The optimum value of h_{sm} is obtained with $\xi_p = 2.1$, $\xi_s = 4.2$ and $\mathcal{G}_{ellipse} = 23$. The h_{sm} increases to a factor of 8.3 from spherical focusing to optimum elliptical focusing. The corresponding pump beam waist size and threshold pulse energy of the OPO at the optimum elliptical focusing condition is calculated to be $15.5 \mu\text{m}$ and $\sim 0.1 \text{ mJ}$, respectively.

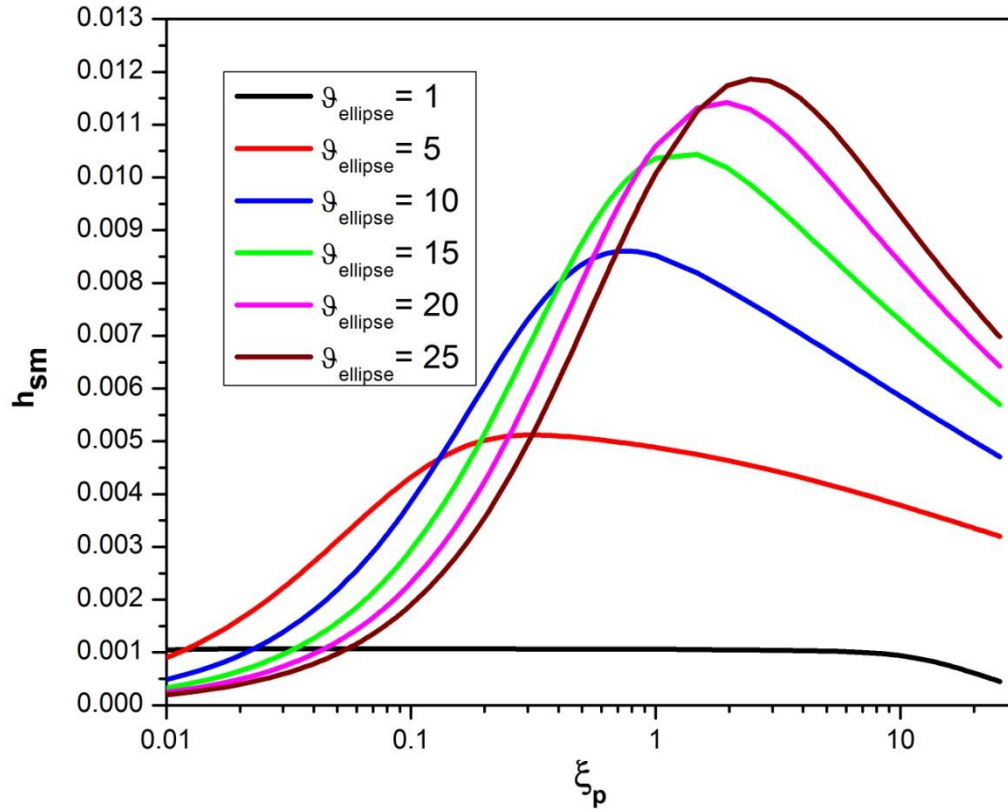


Fig.2.1: Variation of spatial coupling coefficient h_{sm} with the pump beam focusing parameter ($\xi_p = \xi_s = \xi$) for different values of beam ellipticity factor g_{ellipse} for the parametric conversion in BBO crystal.

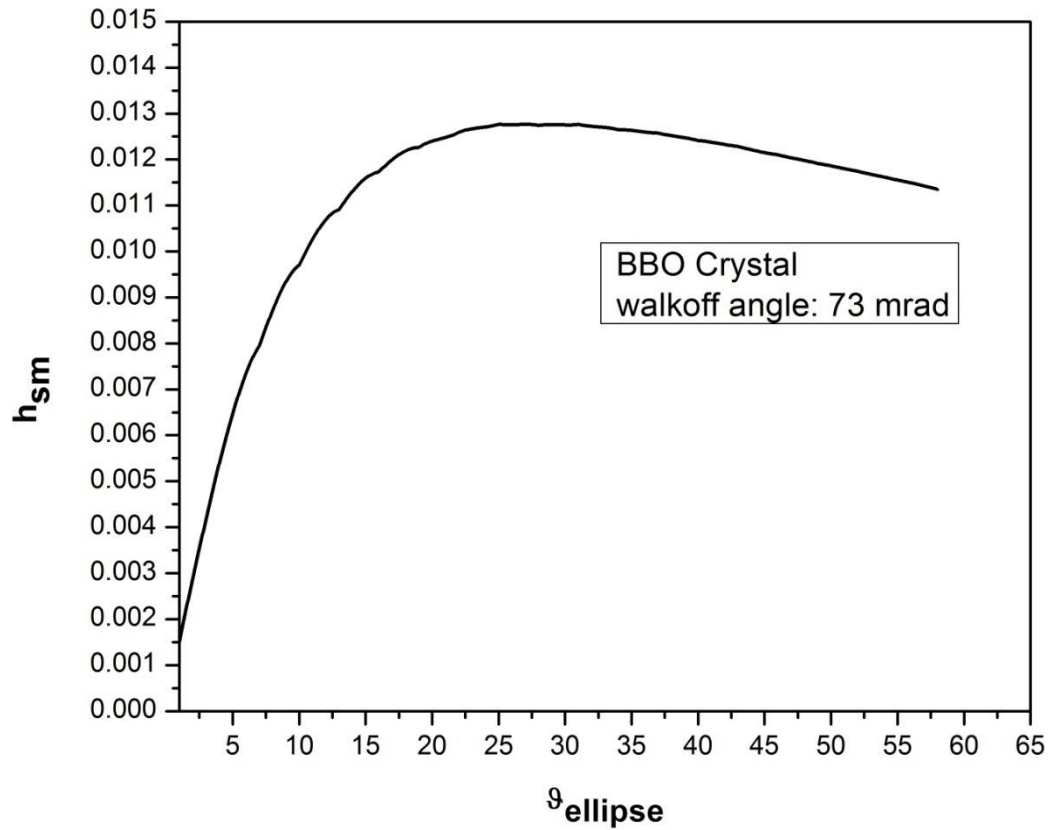


Fig.2.2: Variation of spatial coupling coefficient h_{sm} as a function of the beam ellipticity factor g_{ellipse} for parametric conversion in BBO crystal.

Consequently, the OPO operating threshold energy is reduced significantly to a low value at the optimum focusing condition because of the smaller focal spot size of the pump beam in the insensitive plane. However, considering the pump pulse energy of 3 mJ with 10 ns pulse width the peak intensity at the crystal surface under the optimum focusing condition is calculated to be 1.7 GW/cm², which is very close to the damage threshold [72] of BBO crystal. Hence, for sustainable operation of a high repetition rate BBO OPO, the intensity of the pump beam should be brought down to much lower value than the optical damage threshold of the crystal. In order to reduce the

intensity of the pump laser further, the area of the elliptically focused pump beam spot on the crystal surface is increased to a sufficiently larger value compared to the area obtained with optimum focusing. At the same time, the threshold pump pulse energy of the OPO should be maintained around 1 mJ so that a high repetition rate DPSSL system delivering pulse energies of 2-2.5 mJ at UV (355 nm) can be reliably used as a pump laser to achieve high average power operation of these OPOs. This is discussed in the next section.

2.4.2 Optimum elliptical focused parameter for damage free high repetition rate operation of the BBO OPO.

It is clearly understood that the maximum elliptical waist size of the pump beam in the y-direction, for which the threshold energy of the BBO crystal OPO may be maintained at around 1 mJ for the focused spot sizes of the pump beam, should be much larger ($> 150 \mu\text{m}$) than the optimum size ($15.5 \mu\text{m}$) obtained from our numerical model results. The Fig.2.3 shows the variation of the threshold pulse energy of the BBO OPO with the ellipticity factor ($\mathcal{G}_{\text{ellipse}}$) of the input pump beam for different confocal focusing parameters (ξ_p). As shown in the Fig.2.3 the threshold pulse energy of the BBO OPO for a confocal parameter of $\xi_p = 0.025$, corresponding to a pump beam waist size of $143 \mu\text{m}$ in the y-direction, reduces to 1 mJ at a beam ellipticity factor ($\mathcal{G}_{\text{ellipse}}$) of 10. This value of the pump beam waist size is calculated to be the maximum, among other confocal parameters with a $\mathcal{G}_{\text{ellipse}}$ factor, for which the threshold of the OPO reduces to 1 mJ. As a result, the peak intensity of the pump beam on the crystal surface with this focused spot size reduces to $\sim 40.5 \text{ MW/cm}^2$, by a factor ~ 42 when compared to the earlier calculated optimum focusing. Hence, using this improved optical focusing geometry of the pump beam high repetition rate DPSSL system, which can deliver pulse energies of 2-2.5 mJ at UV (355 nm), was used for

reliable and sustainable pumping operation of the OPO without damaging its intra-cavity BBO crystal.

2.4.3 Experimental verification

To study the threshold pump pulse energy of the BBO OPO experimentally for the above calculated elliptical focusing geometry, a plane mirror cavity-based BBO OPO was setup. This OPO set up was pumped by the third harmonic (355 nm) of a Q-switched Nd:YAG laser, which delivered a smooth temporal profile of FWHM 10 ns, at 10 Hz PRF, at a maximum pulse energy of 50 mJ. This pump laser provides a circular beam of size 5 mm in diameter with a far-field beam

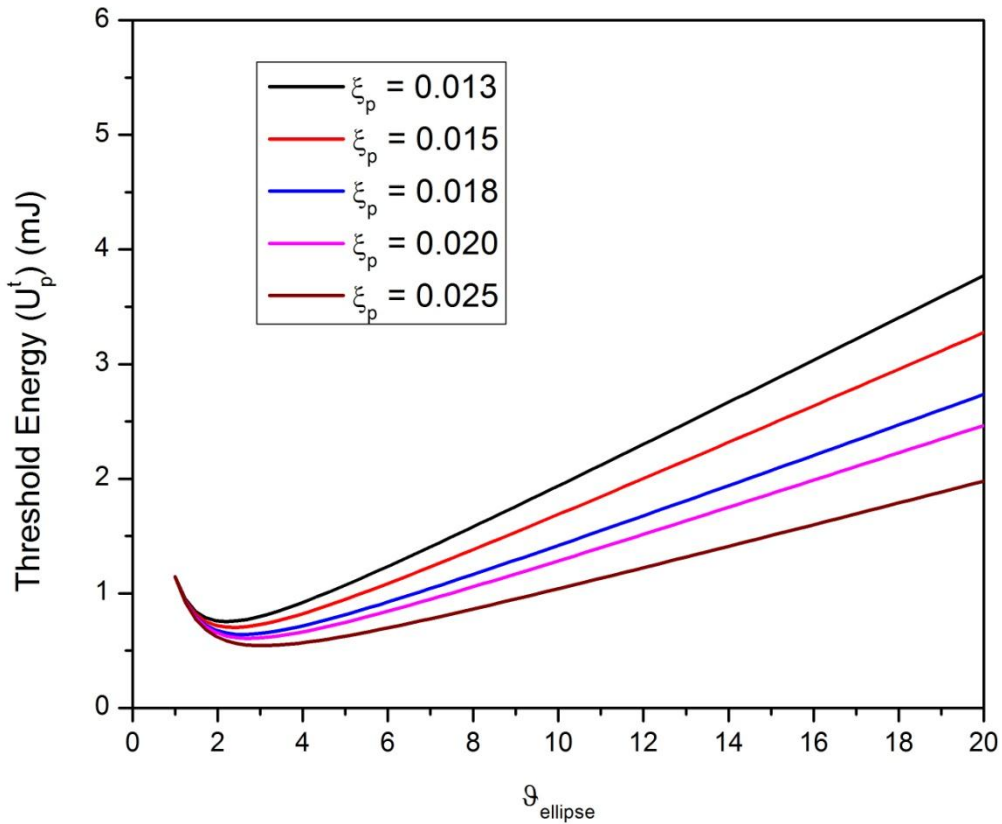


Fig.2.3: Variation of threshold pulse energy as a function of the beam ellipticity factor g_{ellipse} for different focusing parameter of the pump beam in the BBO crystal based OPO.

divergence of less than 0.5 mrad. The Fig.2.4 shows the schematic of this experimental setup of BBO crystal based OPO. The OPO input cavity mirror (M3) possesses high reflectivity $> 99\%$ and the output coupler (M4) is coated for 70% reflectivity in the same 490 nm- 630 nm spectral region. It may be noted that both the mirrors of the OPO cavity have high transmission at the pump and idler wavelengths to prevent doubly resonant operation. In this OPO setup of cavity length 40 mm, we have used a BBO crystal having dimensions $6 \times 8 \times 15 \text{ mm}^3$ and the crystal is cut ($\theta=30^\circ$, $\phi = 0$) for Type-I phase matching. The optical arrangements for the cylindrical focusing geometry adopted for achieving the elliptical focused spot of the pump laser at the center of the crystal are described in detail in our earlier work [78]. Briefly, the beam waist size of the elliptically focused pump beam is measured to be 2.3 mm in the x-direction (walk-off plane) and $148 \mu\text{m}$ in the y-direction and the corresponding confocal parameter ξ_p and $\mathfrak{g}_{\text{ellipse}}$ factors are 0.023 and 15.5, respectively. Using this cylindrical focusing geometry of the pump beam, the threshold pulse energy of the broadband BBO crystal OPO at a signal wavelength of 560 nm is experimentally measured to be 1.5 mJ. This is about 12.6 times less than the threshold pump pulse energy of the same OPO for spherical focusing geometry with the pump beam waist size of 2.3 mm. The threshold pulse energy calculated from the numerical model for the above elliptical focused beam waist at a signal wavelength of 560nm is 1.34 mJ, which is very close to the measured value. The h_{sm} value decrease from 8.862×10^{-4} to 4.92×10^{-4} and the corresponding threshold pump (355 nm) pulse energy was calculated to be increased from 1.34 mJ to 2.44 mJ when the focusing of the pump beam was changed from elliptical ($2.3 \text{ mm} \times 0.148 \text{ mm}$) to spherical (spot size 0.6 mm) while keeping the pump beam area approximately similar on the BBO crystal. However, optical damage to the BBO crystal was observed while experimentally measuring the threshold of the

OPO using the spherical focusing optics, when the pump beam spot size was reduced to less than 1 mm.

To this end, the variation of threshold pulse energy of the BBO OPO has been calculated across its tuning range by considering the variation in the nonlinear coefficient (d_{eff}) and beam walk-off angle with the signal wavelength [59] and compared with the experimentally measured values. The Fig. 2.5 illustrates the comparison of theoretically calculated and experimentally measured threshold pump (355 nm) pulse energies of the constructed broadband OPO, as shown in the Fig. 2.4, across its tuning range.

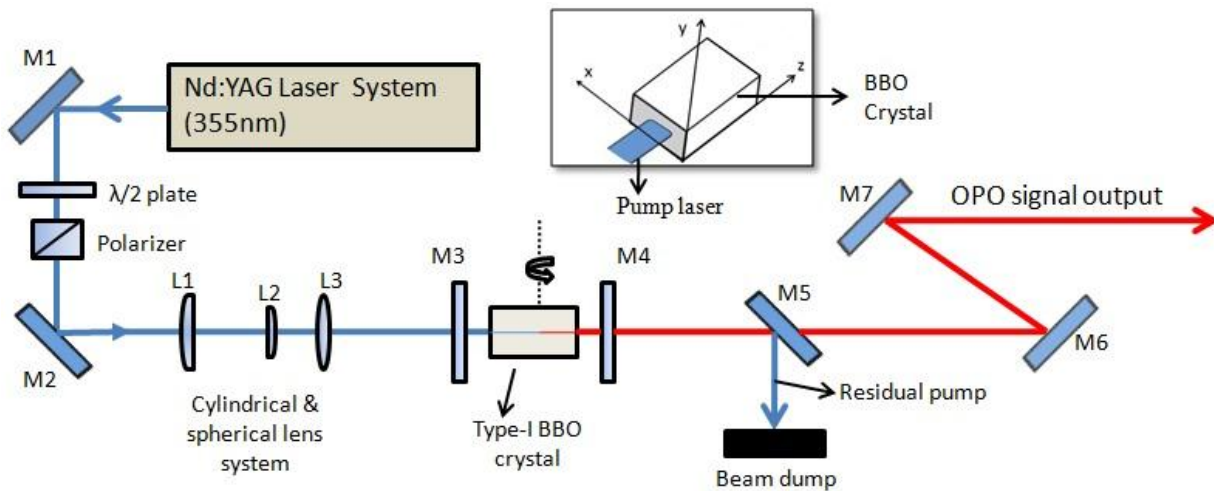


Fig.2.4: Schematic of the experimental setup of the OPO. M1, M2: Pump beam routing mirror, M3, M4: OPO cavity mirrors, M5: Pump beam reflector, M6, M7: Signal beam reflectors. The inset showing a typical illustration of the Type-I BBO crystal with laboratory axes xyz and the elliptical focused pump beam spot on the crystal.

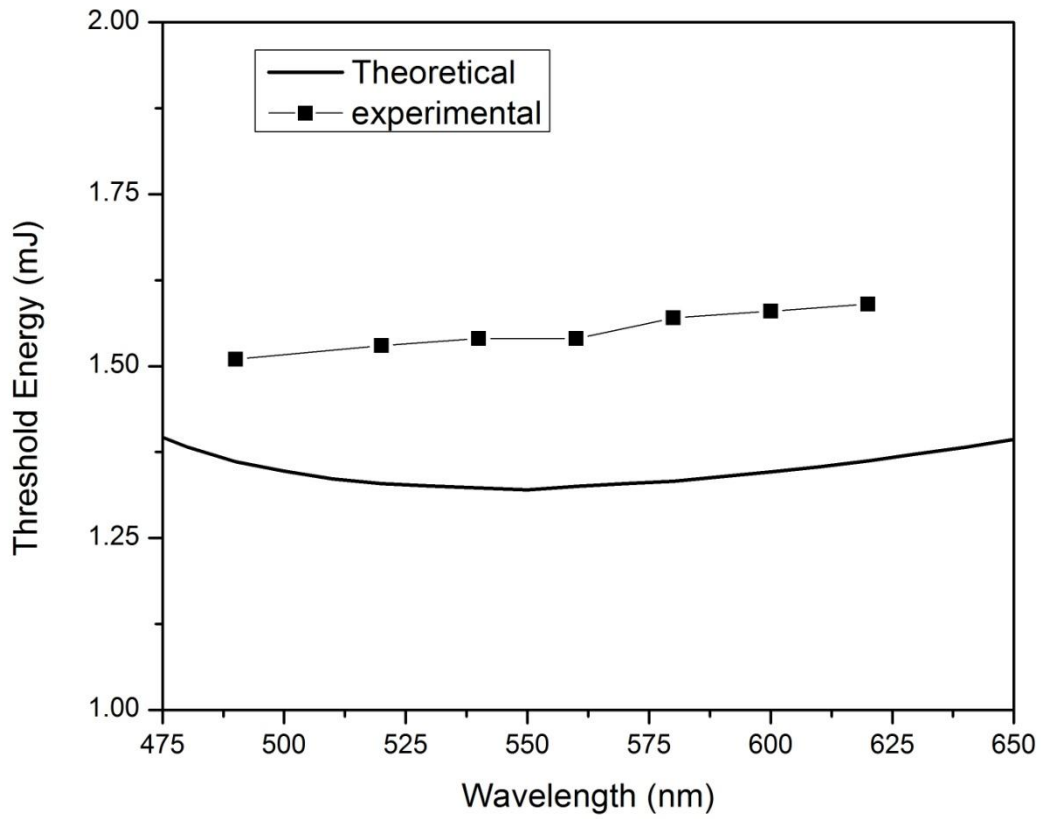


Fig.2.5: Comparison of theoretically calculated and experimentally measured threshold pump pulse energies of the broadband BBO OPO, pumped by 355 nm output of a Q-switched Nd:YAG Laser (10Hz), across its tuning range.

2.5 Conclusions

In conclusion, we have developed a numerical model to determine the optimum elliptical focusing parameters of the input pump beam at 355 nm for achieving low threshold broadband operation of a singly resonant nanosecond β -BaB₂O₄ (BBO) optical parametric oscillator (OPO). The results of our model have illustrated clearly that the parametric gain of a broadband BBO OPO increases by a factor of ~ 8.3 with the optimum elliptical focusing parameters in comparison to the spherical focusing ($g_{\text{ellipse}}=1$) geometry of the pump beam. However, at the optimum focusing condition, the peak intensity of the pump beam is calculated to be very high, approaching the damage threshold of the BBO crystal for the operation of such OPO. Hence, we have utilized our model calculation results in determining the maximum size of the elliptical focused pump beam at 355 nm on the crystal for which the threshold energy of the Type-I BBO crystal based OPO reduces to ~ 1 mJ. At the same time, the pump peak intensities are reduced by about 50 times thus enabling the reliable OPO operation under excitation by the third harmonic of a high pulse repetition rate (5 kHz) DPSSL system operating with a pulse energy of 2 mJ to 2.5 mJ. This has facilitated us to demonstrate damage-free high average power operation of the broadband BBO OPO. The threshold pulse energies of such Type-I BBO crystal based OPO, pumped with the third harmonic of a high average power DPSSL, have been calculated using our theoretical model across its broad tuning range and compared with the experimentally determined values. A good agreement is observed between our model and experimental values.

Chapter 3

Design and development of a DPSSL (355 nm) pumped high repetition rate nanosecond BBO OPO

In this chapter, we report our studies on the successful development of a high repetition rate (5 kHz), nanosecond, Type-I phase-matched β -BaB₂O₄ (BBO) crystal based optical parametric oscillator (OPO), pumped by the third harmonic (355 nm) of a Diode Pumped Solid State Laser (DPSSL), for the first time. The conventional high threshold pump pulse energy, which has been impeding the high repetition rate operation of BBO OPO, is gainfully reduced to ≤ 1 mJ by using optimized cylindrical focusing of the pump beam. The performance of the OPO is compared for different gain lengths of the Type-I BBO crystal and determined the optimum length of the crystal for the efficient operation of the OPO. We have obtained a stable output power of ~ 2.6 W at a typical signal wavelength 492 nm, at a conversion efficiency of 26 %, when excited with the third harmonic (at 355 nm) output of a DPSSL operating at 5 kHz.

3.1 Introduction

Traditionally, the nanosecond singly resonant optical parametric oscillators have been pumped with flash lamp pumped Q-switched Nd:YAG lasers and with their harmonics [27, 28, 31, 84] and of late with diode pumped solid state lasers (DPSSL) for high average power operation [85-87]. The advent of new period poled crystals with a large effective nonlinearity and long interaction lengths, combining with the advances in the diode pumped laser technology, has

facilitated the development of high repetition rate nanosecond OPO's with pulse energies spanning from a few μJ to mJ in the infrared (IR) spectral region [88, 89]. Recently, H. Q. Li et al [69] have demonstrated high PRF (10 kHz) operation of the OPO using 50 mm long LiB_3O_5 (LBO) crystal in non-critical phase-matching (NCPM) configuration. The OPO was pumped with second harmonic (532 nm) of a DPSSL, which gave signal output up to 9.4 W at 900 nm for pump power of 18 W. The NCPM condition, discussed in section 1.2.9 of chapter 1, avoids spatial walk-off and angular acceptance, and thus allowed to use tightly focused pump beam. Therefore, a large size LBO crystal based OPO allowed the generation of high average power tunable output.

However, the visible to NIR spectral region tunable nanosecond OPO's based on BBO crystal, pumped by the third harmonic of a Nd:YAG laser at 355 nm, are still operated in low repetition rates. The multi kHz repetition rate operations of these OPO's are not yet demonstrated. The main limitation, as discussed in chapter 1 in section 1.1.2, arises since these OPO's exhibit high pump (UV) pulse energy threshold, generally a few tens of mJ . Thus, it demands high pulse energy ($\sim 30 \text{ mJ}$) along with the good temporal and spatial quality of the pump beams. Presently, UV (355 nm) pump lasers delivering such high pulse energies at multi-kHz repetition rates are not available. Further, the large double refraction walk-off angle exhibited by the BBO crystal limits the interaction gain length of the crystal with tight focusing of the pump beam which demands large size pump beam in the walk-off sensitive plane of the crystal. It may be noted that the walk-off angle of BBO is 3.2 deg. To this end, non-critical phase-matching configuration, employed by H. Q. Li et al [69] for LBO crystal OPO, which allows tight focusing of the pump beam, to reduce the pulse energy requirement of the pump laser, is not possible in BBO crystal OPO because of its low temperature coefficient of birefringence.

In our earlier work on Type-I BBO OPO, pumped by 355 nm output of a low repetition rate (10 Hz) Nd:YAG laser, a substantial reduction in the pump threshold energy was achieved using cylindrical focusing geometry [78]. Cylindrical focusing of the pump laser beam produces an elliptical beam on the BBO crystal. The major axis of ellipse lies in the walk-off sensitive plane and is kept large so that the aperture length in the walk-off sensitive plane is greater compared to the crystal length. At the same time, the high intensity of the pump beam is maintained by tight focusing in the orthogonal plane, which is insensitive to walk-off. However, this OPO was operated at a very low repetition rate, 10 Hz, instead of our present work toward multi kHz, high average power OPO. The optical scheme of this low repetition rate OPO is illustrated in the Fig.4.1.

This cylindrical geometry of the pump beam focusing, compared to its conventional spherical focusing geometry, increases the interaction length of the pump and generated signal beams simultaneously on the crystal, resulting in an enhancement in the parametric gain. Besides, the line focus cylindrical geometry of the pump beam diminished the thermal gradients within the crystal, which facilitated reducing the thermal detuning problem and preventing optical damage [90] of the crystal and other intra-cavity optics of the OPO under high average power operation. The main advantage is, of course, a higher net gain and hence, a lower pump threshold of the OPO.

We have adopted a similar pump focusing geometry in our present OPO setup for demonstrating its high repetition rate operation. In this chapter, we report studies on the operation of high repetition rate (5 kHz), nanosecond temporal pulse width, Type I BBO OPO, which can be tuned from 490 nm to 630 nm. Herein, we describe the experimental setup and signal output performance of such high repetition rate BBO OPO.

3.2 High repetition rate Type-I Phase matched BBO OPO

3.2.1 OPO Configuration

A schematic of the experimental setup of the constructed high repetition rate OPO is shown in the Fig.3.1. The OPO consists of a Type I phase-matched BBO crystal inside an optical cavity formed by flat-flat mirrors. The pump beam input cavity mirror (M3) of the OPO possesses high reflectivity $> 99\%$ in the spectral region 490 nm to 630 nm and the output coupler (M4) is coated for optimum reflectivity at 70 % in the same spectral region. The optimum reflectivity of the OPO output coupler is calculated based on the parametric gain coefficient which is calculated to be $\sim 0.7\text{ cm}^{-1}$ (Equation (1.6), in section 1.2.5 of chapter 1) and scattering and absorption losses which are assumed to be $\sim 5\%$ for our design. Moreover, the earlier workers, published in ref. [50] and [68], have used the similar reflectivity output coupler for the 355 nm pumped BBO OPO. Both input and output mirrors of the OPO cavity possess high transmission at pump and idler wavelengths to prevent doubly resonant operation the OPO. The transmission curves of the OPO cavity mirrors are shown in the Fig. 3.2.

The BBO crystal was mounted on a calibrated precision rotation stage and the wavelength tuning has been accomplished by varying the phase-matching angle θ about the tuning axis. The Fig. 3.3 illustrates pump beam polarization E vector direction, optic axis direction, and the axis of rotation of the crystal.

As shown in the Fig. 3.1, the residual pump energy after the exit OPO cavity mirror is routed to the beam dump using the dichroic mirror M5. The mirror M5 has high reflectivity at pump wavelength (355 nm) and high transmission for OPO signal wavelengths. The signal beam is then directed to a power meter and a monochromator using the mirrors M6 and M7. Both of

these mirrors have high reflectivity at the OPO signal wavelengths and high transmission for pump and idler wavelengths so as to block the pump and the idler from reaching the OPO signal output power meter and wavelength measurement systems.

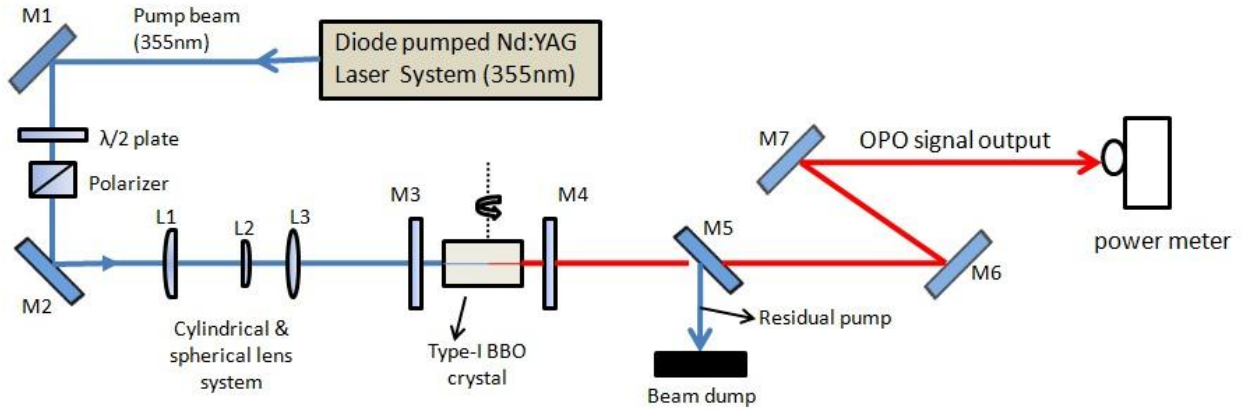
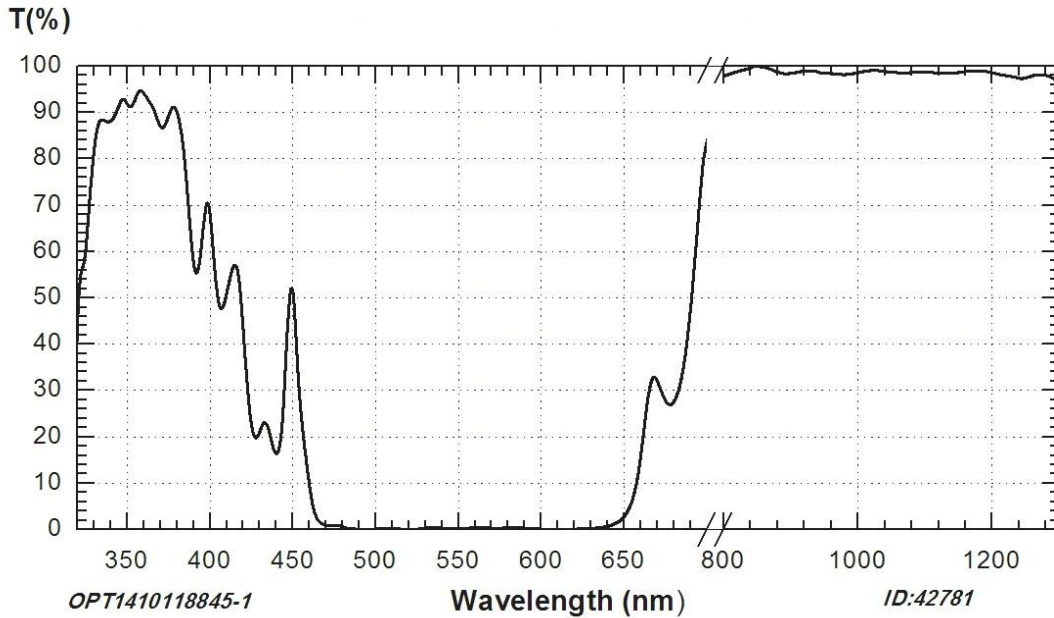
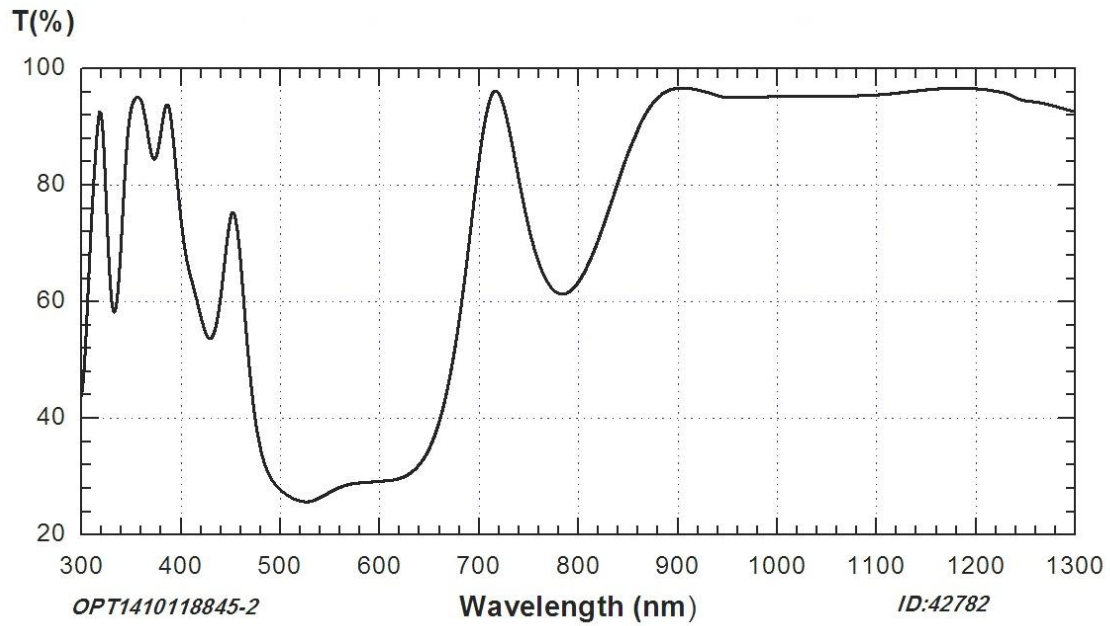


Fig.3.1: Schematic of the experimental setup of Type-I phase matched BBO crystal based OPO. M1, M2: Pump beam routing mirror, M3, M4: OPO cavity mirrors, M5: Pump beam reflector, M6, M7: Signal beam reflectors.



A)



B)

Fig.3.2: Transmission spectra of the BBO OPO cavity optics, A) Input mirror and B) output coupler.

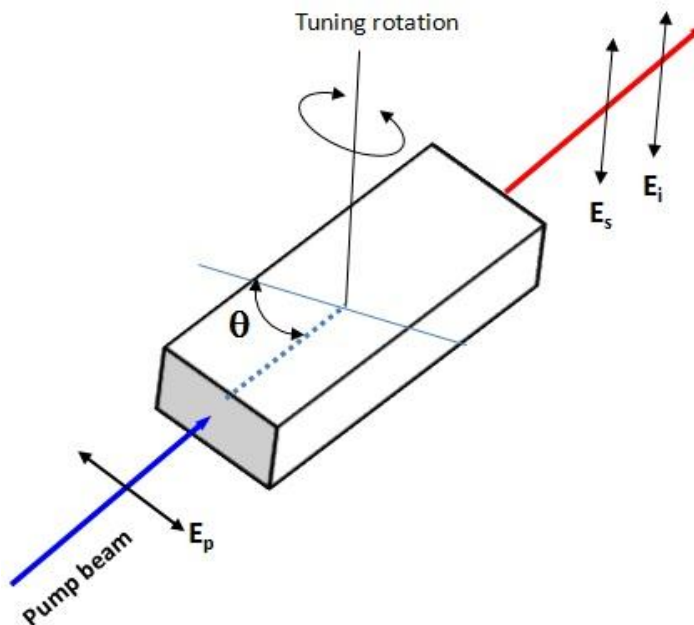


Fig.3.3: Schematic illustration of pump and generated signal, idler beams polarization direction, optic axis direction and axis of rotation for frequency tuning in Type-1 BBO crystal.

3.2.2 Nonlinear Crystal

In this OPO setup, we have used three available different gain lengths of BBO crystals (Castech, China) of dimensions $6 \times 8 \times 12 \text{ mm}^3$, $6 \times 8 \times 15 \text{ mm}^3$ and $6 \times 8 \times 18 \text{ mm}^3$ which are cut ($\theta=30^\circ$, $\phi = 0$) for Type-I phase matching and the corresponding OPO cavity lengths for the above BBO crystals are 22 mm, 25 mm and 28 mm, respectively. The crystal faces are coated with high damage threshold protective coating film at 355 nm. The specifications of the BBO crystal are provided in Table 3.1. The Fig. 3.4 shows the transmission spectrum of the 15 mm and 18 mm long Type-I BBO crystals employed in our OPO setup.

Table 3.1: Important parameters of the BBO crystals used in the high repetition rate OPO

BBO Crystal	Parameter
Flatness	$\text{Lambda}/8 @ 355 \text{ nm}$
Surface quality	10/5 scratch/dig
Parallelism	Better than 20 arc seconds
Perpendicularity	Better than 5 arc minutes
Optical homogeneity	$\Delta n \sim 10^{-6}/\text{cm}$
Linear absorption coefficient	$\alpha < 0.01 \text{ cm}^{-1} @ 355 \text{ nm}$
Damage threshold	$500 \text{ MW}/\text{cm}^2 @ 355 \text{ nm}$
Coating	Protective AR coating

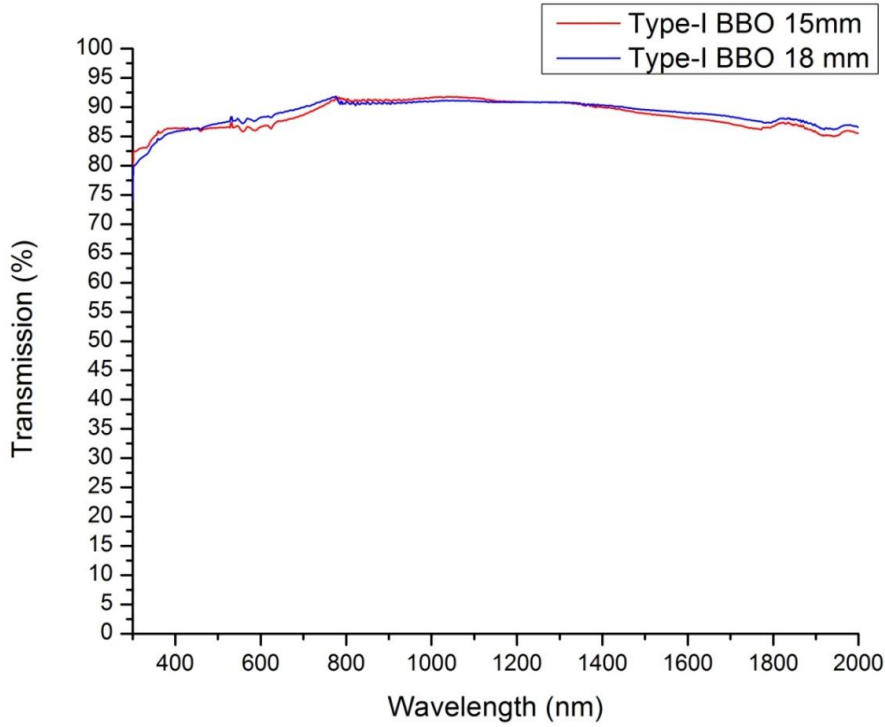


Fig.3.4: Transmission spectra of the Type-I phase matched BBO crystals used in the OPO setup.

3.2.3 Pump laser requirements

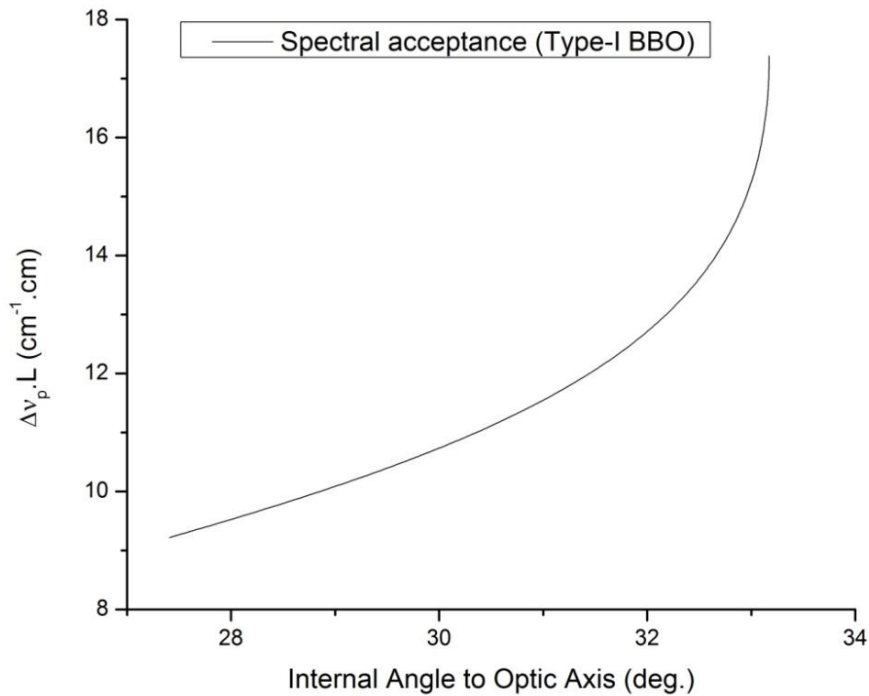
The maximum allowed pump bandwidth and angular divergence in the pump beam for BBO crystal giving rise to the momentum-mismatch $|\Delta k| \sim \frac{\pi}{l}$ discussed in Chapter-1 Section 1.2.8 can be obtained by using the equations (3.1) and (3.2) [36],

$$\Delta\nu_p = \frac{1}{l} [(n_p - n_i) + \lambda_i \left(\frac{dn_i}{d\lambda_i}\right) - \lambda_p \left(\frac{dn_p}{d\lambda_p}\right)]^{-1}. \quad 3.1$$

$$\Delta\theta_p = \frac{1}{l} \left[\frac{1}{\lambda_p} \left(\frac{\partial n_p}{\partial \theta_p}\right) \right]^{-1} \quad 3.2$$

where n_p and n_i are the refractive indices at the pump and idler wavelengths respectively, λ_p and λ_i are wavelengths of the pump and idler wavelengths respectively. The variation of spectral

acceptance and angular acceptance bandwidths for the pump laser with the internal phase-match angle across the tuning range of Type-I BBO OPO is shown in the Figures 3.5(A) and 3.5(B). From the plots, it is evident that for efficient operation of the OPO, the spectral spread of the pump laser must be confined to within few cm^{-1} and the angular divergence of the pump laser must be less than 0.3 mrad and also techniques such a cylindrical focusing geometry described in section 3.2.5 can be employed to ensure that all the pump beam propagates within the narrow acceptance angle of the BBO crystal.



A)

B)

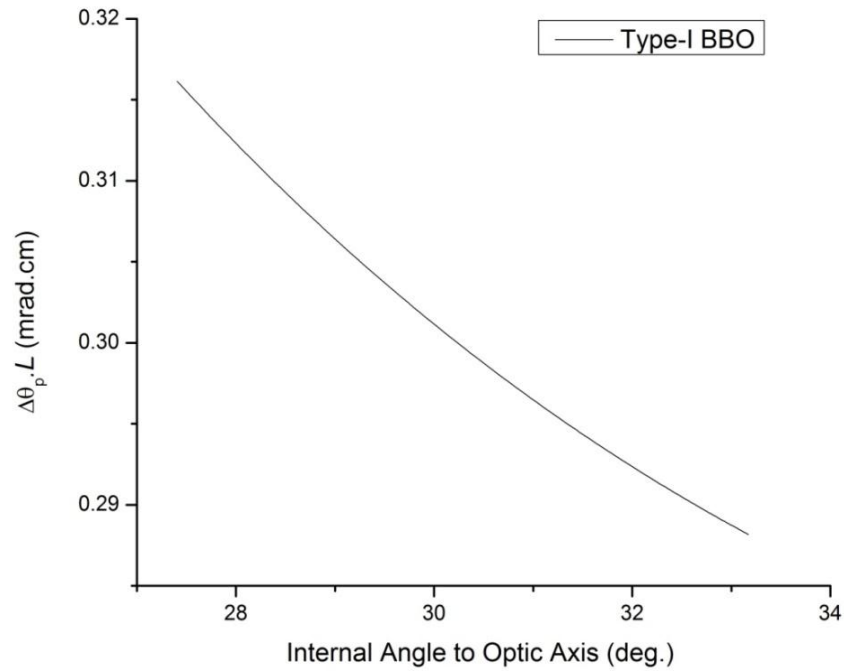


Fig.3.5: A) Spectral acceptance bandwidth B) Angular acceptance bandwidth for the pump laser of Type-I BBO OPO.

3.2.4 Pump Laser System

The pump source is the third harmonic (355 nm) of a diode pumped Nd:YAG laser (M/S Edgewave GmbH, Germany). The laser delivers a smooth temporal profile with 10 ns full width half maximum (FWHM) at 5 kHz PRF with a pulse energy of ~ 3.2 mJ at 355 nm and the energy stability is about less than 2%. The temporal profile of the pump laser operating at a repetition rate of 5 kHz is shown in the Fig. 3.6. The long term power stability plot of the pump laser operating at 5 kHz repetition rate is shown in the Fig. 3.7. The standard deviation of power over 30 minutes of operation is ~ 40 mW.

Table 3.2: Important parameters of the pump laser (DPSSL) used in the high repetition rate OPO

DPSSL System	Parameter
Wavelength	355 nm
Average Power (max.)	~16 W
Pulse duration	10-12 ns
Repetition rate	0-5 kHz
Jitter	< 1ns
Beam divergence	~ 150 μ rad
Spatial mode	TEM ₀₀ , $M^2 < 2$
Beam pointing stability	Better than 50 μ rad
Beam diameter	≥ 5 mm
Polarization	100:1, linear

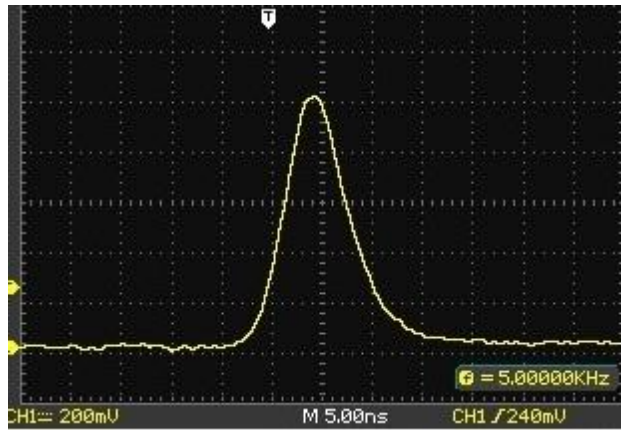


Fig.3.6: The temporal profile of the pump laser (DPSSL) operating at a wavelength of 355 nm at a repetition rate of 5 KHz.

The repetition rate of the diode pumped solid-state laser (DPSSL) system can be varied from 1 kHz to 5 kHz. The DPSSL provides the UV beam of size 5 mm × 5 mm with a far-field beam divergence of less than 0.5 mrad. The maximum output power of the pump laser at 355 nm is 16 W. The output beam from the pump laser is routed through a variable attenuator optical setup, comprising of a multiple order half-wave plate and a polarizer at 355 nm, which are used to vary the output power of the pump laser to OPO.

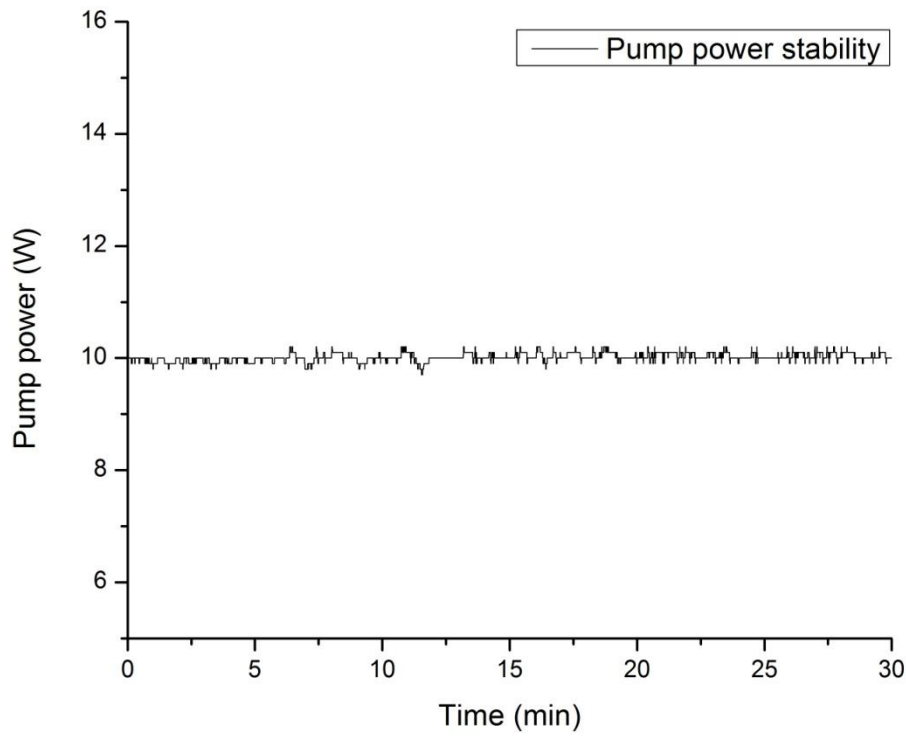


Fig.3.7: The power stability of the pump laser (DPSSL) operating at a wavelength of 355 nm at a PRF of 5 kHz.

3.2.5 Pump beam focusing geometry

The UV pump beam at 355 nm is allowed to pass through a cylindrical focusing geometry optical set up which is shown in the Fig. 3.1. The pump focal geometry which has been used to generate the elliptical focused beam was similar to Coutts et al. [49]. However, they used it for SHG of copper vapor laser output. In our case, the UV pump beam with 5 mm diameter is compressed in the horizontal plane by cylindrical telescope lenses comprising of L_1 and L_2 , which is configured to produce a slightly diverging beam in the horizontal plane. The focal length of L_1 and L_2 was 100 mm and 50 mm, respectively. The distance between L_1 and L_2 was kept approximately 145 mm. The pump beam is then focused using a 500 mm focal length spherical lens (L_3) in the non walk-off plane of the crystal to about 133 μm waist size while producing an approximately 3.8 mm diameter beam in the horizontal walk-off plane. The focusing geometry is illustrated in the Fig.3.8. The generated elliptical spot size is close to the optimum elliptical focused size required for damage-free low threshold (< 1 mJ) operation of the OPO as predicted by the numerical model discussed in the chapter 2.

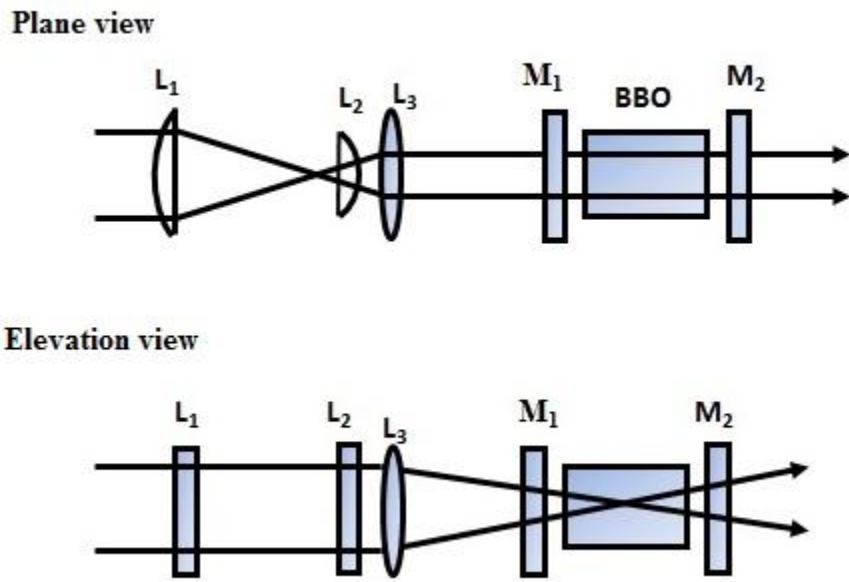


Fig.3.8: Schematic of the Cylindrical focusing geometry; L1: Cylindrical lens of focal length 100mm; L2: Cylindrical lens of focal length 50 mm; L3, Spherical lens of focal length 500mm; M1, M2, OPO cavity mirrors.

3.3 Experimental Results

3.3.1 Performance of the OPO

With the available set of mirrors, the Type I BBO crystal OPO signal could be continuously tuned from 490 nm to 630 nm, corresponding to calculated idler wavelengths from 1288.5 nm to 813.3 nm. The tuning range is limited by the reflectivity profile of the present cavity mirrors. The Fig. 3.9 shows the measured wavelength curve of this Type-I BBO OPO. The variation of signal output power, measured at a typical signal wavelength 492 nm as a function of the pump power at 5 kHz repetition rate, for different lengths of BBO crystals, are shown in the Fig. 3.10. The OPO output signal power increases with the input pump power in all three cases of the BBO crystals. The maximum output power of 3.23 W is obtained with an input pump power of 11.5 W, corresponding to a conversion efficiency of 28 % at signal wavelength 492 nm. It may be noted that the single-pass gain of the OPO signal possesses quadratic dependence on the parametric crystal interaction length. Hence, the output power of the OPO is enhanced with the increase in the crystal length. However, the beam walk-off effect dominates with the increasing length of the crystal, to more than an optimum value, which degrades the performance of the OPO. Consequently, the slope efficiency of the OPO is observed to increase from 26.8 % to 33.4 %, and the threshold pump power decreases from 5.6 W to 2.55 W when the BBO crystal length is changed from 12 mm to 15 mm. However, the increase in the slope efficiency (0.8 %) and the decrease in threshold pump power (0.05 W at 5 kHz) of the OPO are observed to be nominal, when the BBO crystal length is increased further from 15 mm to 18 mm, because of beam walk-off effect.

Thus, the optimum length of the BBO crystal is fixed at 15 mm for the present high repetition rate OPO system for achieving reasonably high slope efficiency and low threshold operation using cylindrical focusing geometry. The Fig. 3.11 shows the variation of measured

signal output power when the OPO signal output is tuned from 490 nm to 630 nm at a fixed pump power of 10 W at a repetition rate 5 kHz. It may be noted that the reduction in the efficiency of OPO system, during tuning output signal wavelength from 490 nm to 630 nm, is correlated to decrease in the effective nonlinear coefficient of the BBO crystal with the increase in signal wavelength and further due to higher reflection losses at the crystal surface.

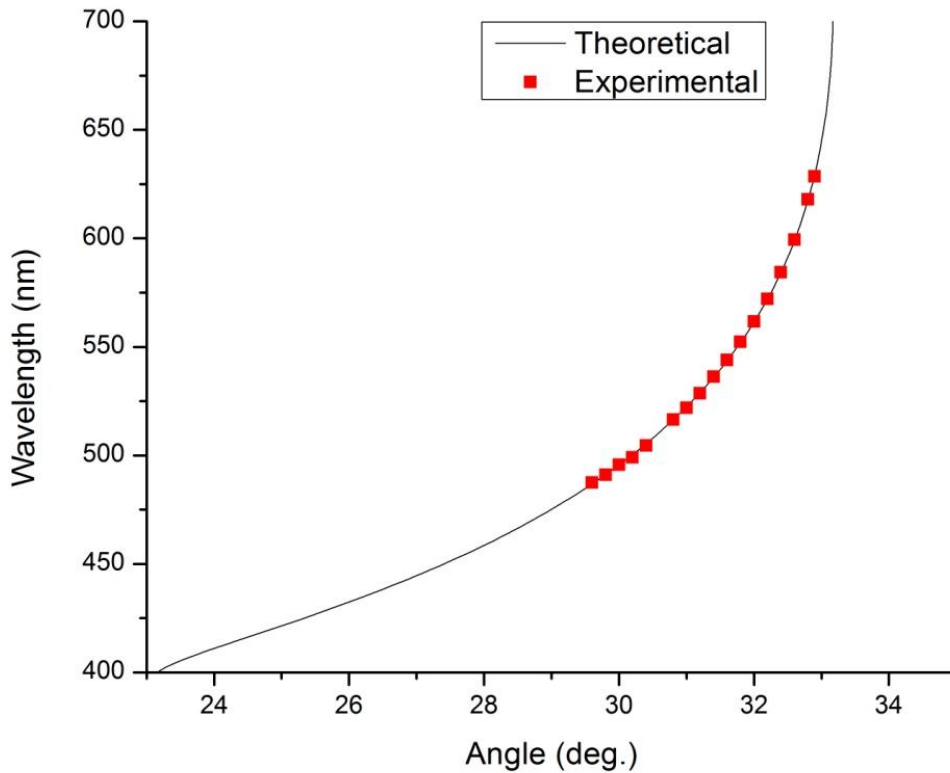


Fig.3.9: The wavelength tuning curve of the Type-I BBO OPO measured using 15 mm long crystal.

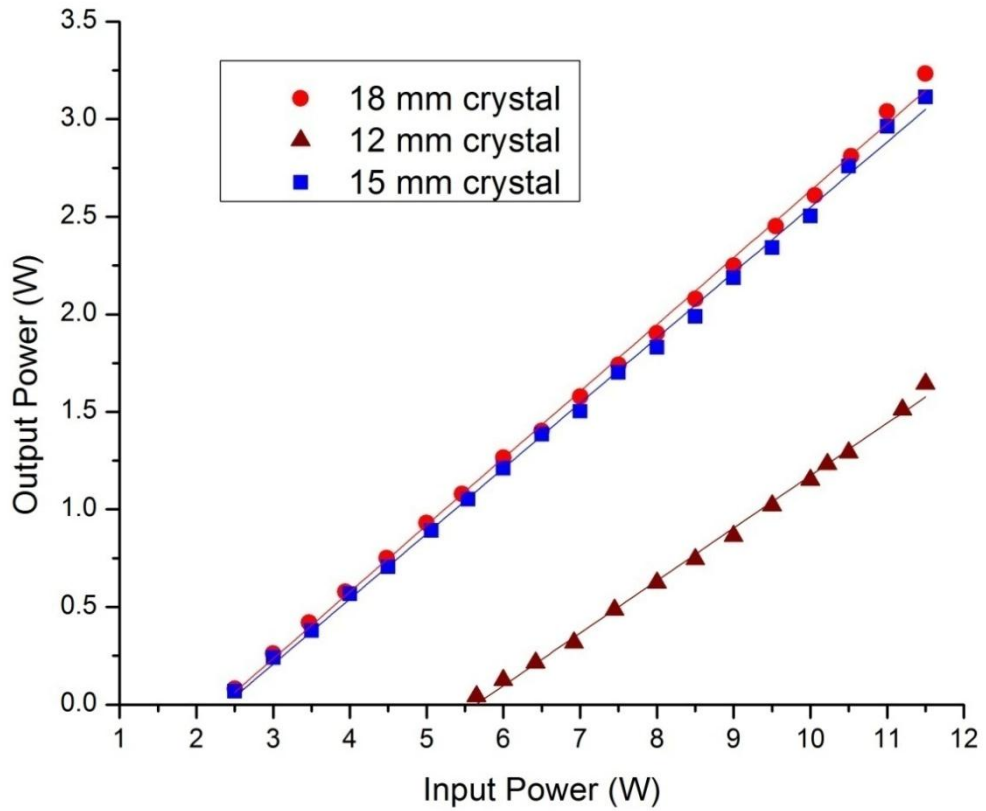


Fig.3.10: Variation of OPO signal output power tuned from 490 nm to 630 nm at a fixed pump power of 10 W. The symbols represent the experimental data and the solid line show the trend in results.

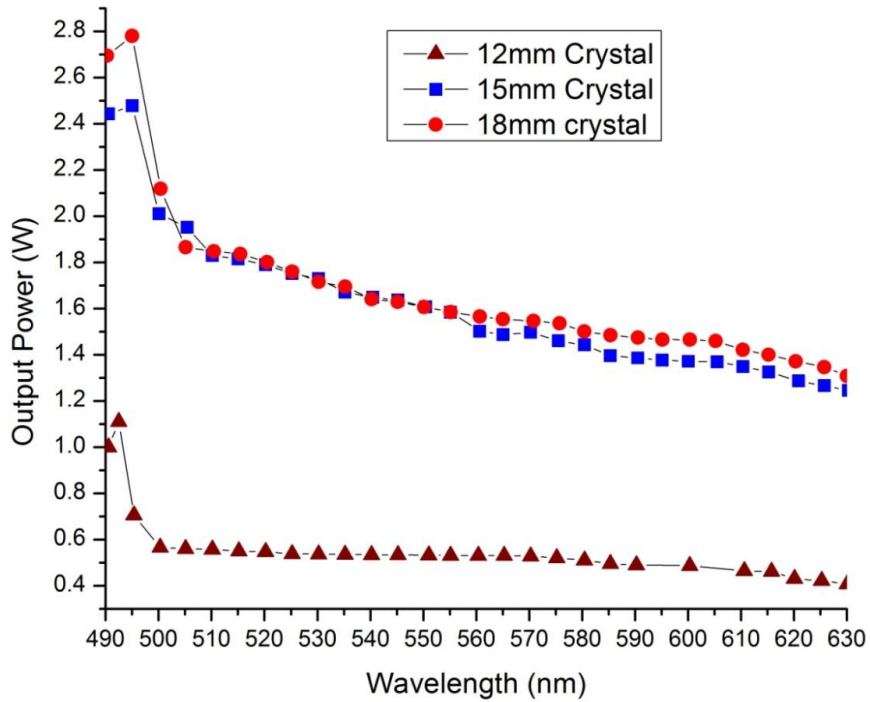


Fig.3.11: Performance comparison of signal output power of Type-I BBO OPO for different crystal sizes at 5 kHz repetition rate at a signal wavelength 492 nm. The symbols represent experimentally observed results and the solid line represents the best linear fit.

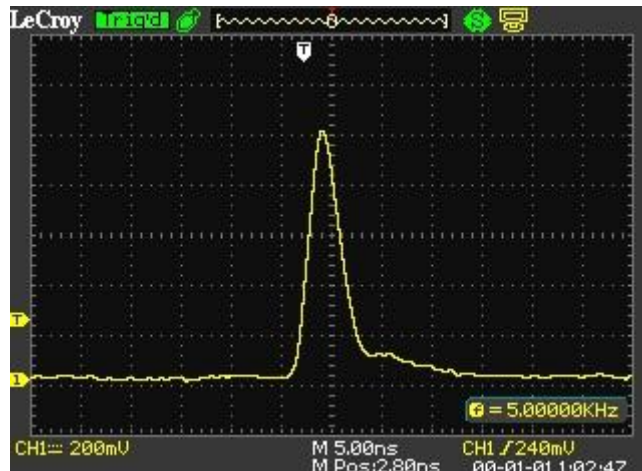


Fig.3.12: The measured temporal profile of the OPO signal output at a wavelength of 492 nm, operated at a repetition rate of 5 kHz

3.3.2 Long term power stability

The power stability of the signal output of Type-I BBO OPO system with 15 mm long crystal is studied by monitoring the output power at 492 nm when operating the pump (355 nm) laser at a repetition rate of 5 kHz. The pulse width of the generated signal output is 6 ns (FWHM). The temporal profile of the signal output was measured using fast PIN photodiode (Alphas, model: UPD-300-SP). The measured temporal profile of the OPO signal output is shown in the Fig. 3.12. The hump at the end of the temporal pulse of the signal is mainly due to the residual 532 nm from the pump laser. The Fig. 3.13 shows the long-term stability of the OPO signal output

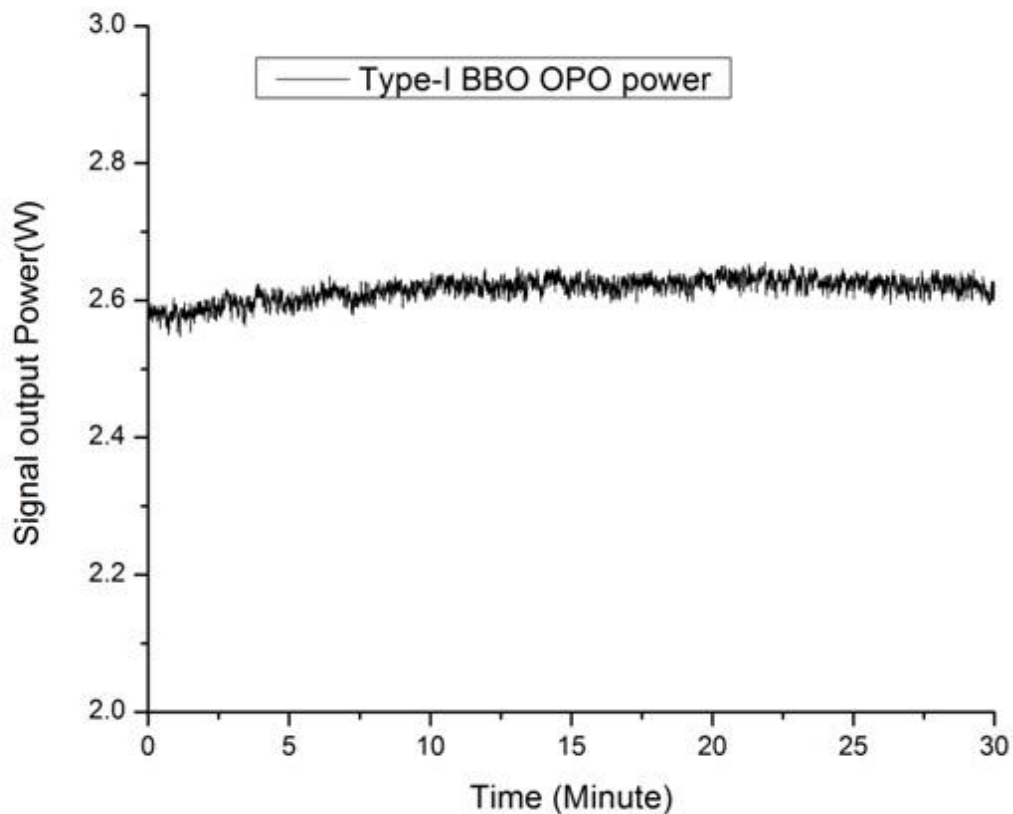


Fig.3.13: Longterm stability of the Type-I BBO OPO signal output power monitored for the duration 30 min.

power monitored for a duration of 30 min using a power meter (Ophir, Israel). During this operation, the OPO is operated with an average output power of 2.6 W at an RMS power stability of $\pm 1.9\%$ for UV pump power at 10 W.

3.3.3 Spectral linewidth

The spectral linewidth of the OPO signal output, without use of any intra-cavity spectral line-narrowing optics, is influenced by a number of factors such as wavelength, dispersion of the BBO crystal, the length of crystal, effective number of passes of the resonant wave, along with the bandwidth, divergence and pulse energy of the pump beam (355 nm) radiation.

The spectral linewidth of the Type-I BBO OPO signal output is measured at different wavelengths across its tuning range from 490 nm to 590 nm using a spectrometer (HR 2000 plus model, Ocean Optics). The spectrometer is able to measure the OPO output wavelength range from 490 nm to 590 nm only with an optical resolution of ~ 0.035 nm. Thus, measurement of the spectral linewidth of the constructed OPO beyond 590 nm is limited by the available spectrometer. The observed variation of the spectral linewidth of OPO output with signal wavelength is illustrated in the Fig. 3.14. The spectral linewidth of the OPO increases from 0.2 nm to 0.5 nm when tuned from 490 nm to 590 nm.

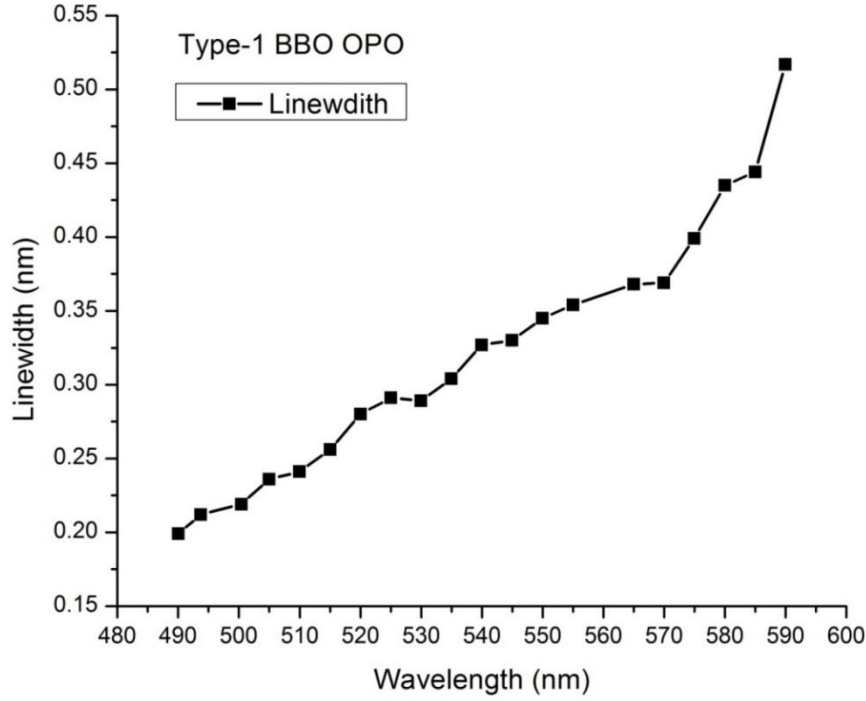


Fig.3.14: Spectral Linewidth of Type-I BBO OPO as a function of signal wavelength.

To understand this observed variation of spectral linewidth of the Type-I BBO OPO for the signal wave across its tuning range, it is theoretically calculated by considering the spectral condensation during the cavity round trips of the OPO pulses. The spectral linewidth for the signal wave is given by [97],

$$\Delta\nu_s \approx \left| \frac{\left[\left(\frac{c}{L} \right) + \left(\frac{c}{2\lambda_p} \right) \left(\frac{\partial n_p}{\partial \theta_p} \right)_0 \delta\theta_p + \Delta\nu_p \beta_{PI} \right]}{\beta_{SI}} \right| \quad 3.3$$

$$\beta_{ji} = \left[(n_j - n_i) - \lambda_j \left(\frac{\partial n_j}{\partial \lambda_j} \right)_0 + \lambda_i \left(\frac{\partial n_i}{\partial \lambda_i} \right)_0 \right] \quad 3.4$$

where $i, j = S, P$ or I as appropriate, n_j and λ_j are refractive indices and vacuum wavelengths respectively, c is the speed of light, and the partial derivatives are referred to $\Delta k = 0$. $\partial\theta_p$ and $\partial\nu_p$

are the full angle divergence and optical bandwidth of the pump beam. In our theoretical calculations, we have considered that the optical bandwidth is reduced by a factor of $m^{-1/2}$, where m is the number of intra-cavity passes during the pump pulse. This factor applies to the first term in the above Equation (3.3) by replacing the crystal length L by L_{eff} , the effective crystal length, approximated by $(m^{1/2}L)$. The spectral linewidth of the OPO is calculated across the tuning range of the Type-I BBO OPO using the above equations by considering the pump beam divergence as 0.15 mrad. The Fig. 3.15 shows the comparison of the theoretically calculated spectral linewidth of the OPO with the experimental observations. In this plot, the linewidth increases towards 600 nm because of the pump beam divergence and at near degeneracy, a small pump beam divergence can lead to large parametric linewidth.

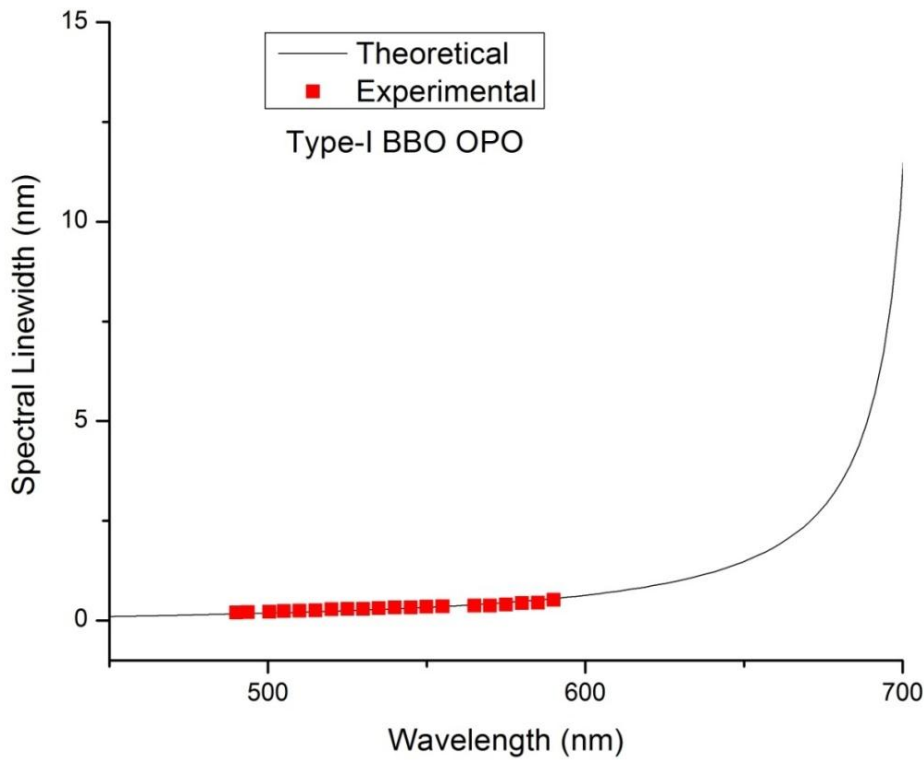


Fig.3.15: Comparison of theoretical and experimentally observed spectral linewidth of Type-I BBO OPO signal output across its tuning range.

3.3.4 Beam quality and pointing stability:

The beam quality, M^2 value and spatial profiles of the generated OPO signal beam at near and far-fields are measured using a commercial laser beam analyzer (Spiricon, M2-200-FW-SCOR). The Fig. 3.16 shows the near and far-field spatial profiles and M^2 factor of the Type-1 BBO OPO output operated at a repetition rate of 5 kHz, measured at a signal wavelength of 492 nm. The M^2 factor at this signal wavelength is found to be $M^2_x = 5.2$ and $M^2_y = 2.5$. The difference in the position of the beam along the x and y direction is due to astigmatism introduced by the cylindrical optics.

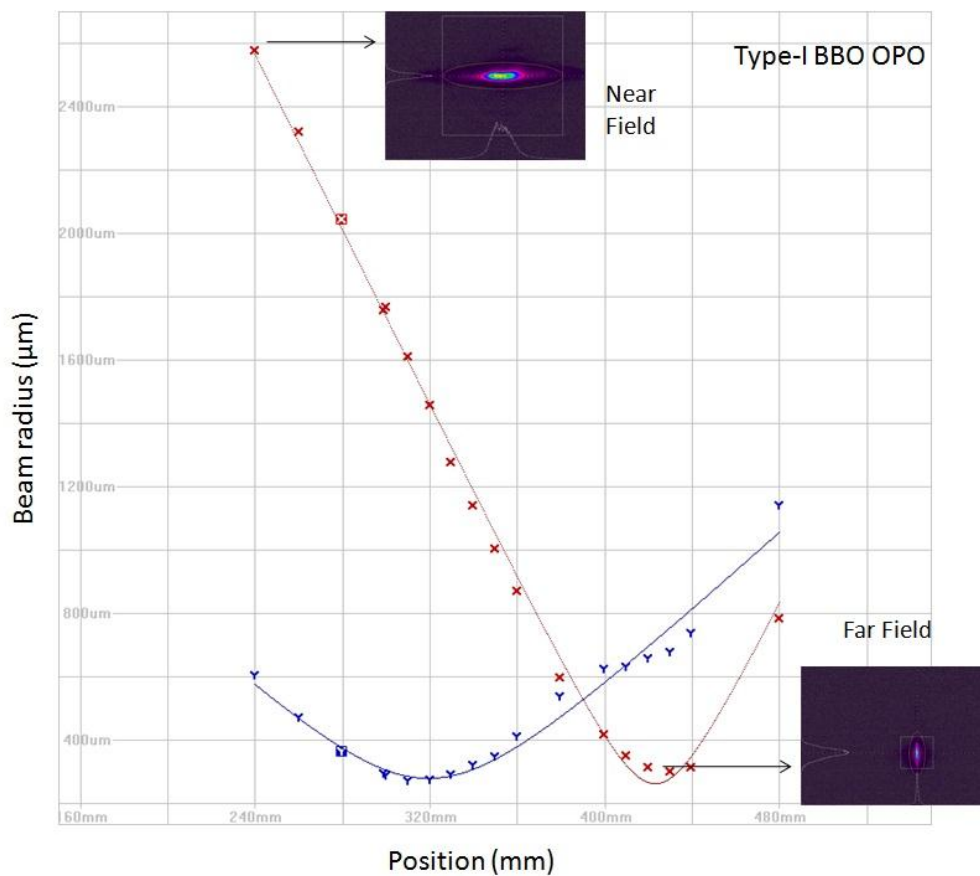


Fig.3.16: The measured M^2 factor, near and far field profiles of the OPO signal beam at a wavelength of 492 nm at a repetition rate of 5 kHz.

The beam pointing stability of the OPO signal output is measured using a commercial laser beam analyzer (Spiricon, LBA-FW-SCOR). The variation of the beam centroid, peak, and radius of the OPO signal at 492 nm, operated at a power of 3 W @ 5 kHz repetition rate, is shown in the Fig. 3.17. The standard deviations of these parameters are measured to be, Centroid: 12.36 μm (X) and 44.03 μm (Y), Peak: 87.55 μm (X), 36.37 μm (Y) and Radius: 30.43 μm .

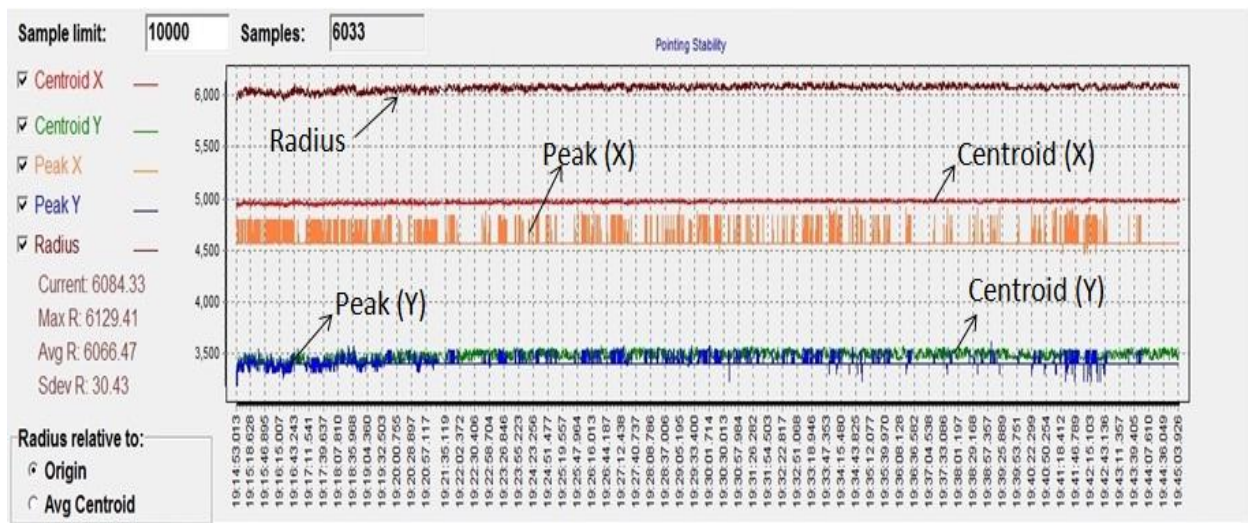


Fig.3.17: The measured beam pointing stability of the OPO signal output at a wavelength of 492 nm at a repetition rate of 5 kHz

3.4 Conclusions

In conclusion, we have developed and demonstrated, for the first time to the best of our knowledge, a broadband, high repetition rate (5 kHz), Type I BBO based OPO, pumped by the 355 nm UV beam of a DPSSL, which can be continuously tuned from 490 nm to 630 nm providing sub-mJ pulse energy. The optical characteristics of this constructed OPO output beam, such as M^2 value, beam pointing stability, near and far-field spatial profiles are measured and characterized in detail. The performance of the OPO output is comparatively evaluated, using three different Type-I BBO crystals of lengths 12 mm, 15 mm and 18 mm, and generated a maximum output of 3.23 W for an input pump power of 11.5 W @ 5 kHz with a high conversion efficiency of ~ 28 % for the 15 mm length BBO crystal. The long-term stability of the OPO output is tested by operating the OPO at its peak power, corresponding to output wavelength 492 nm, at a repetition rate of 5 kHz for the duration of about 30 minutes. During this continuous operation, the OPO operated with an average output power of 2.6 W at a conversion efficiency of 26 % with power stability of 1.9 %. The spectral linewidth of the OPO is studied across its tuning range and it is found to vary from 0.2 nm to 0.5 nm.

Chapter 4

Design and development of a high repetition rate single longitudinal mode BBO OPO pumped by 355 nm

In this chapter, we describe the design, development, and characterization of a high repetition rate (1-2 kHz), nanosecond, single longitudinal mode (SLM) Type-II phase-matched β -BaB₂O₄ (BBO) crystal OPO pumped by the third harmonic (355 nm) of a Diode Pumped Solid State Laser (DPSSL). The SLM operation of this BBO crystal based OPO is found to be tunable from 490 nm to 630 nm. The high threshold and broad spectral linewidth of the Type-II phase-matched BBO have been reduced by employing double-pass pump configuration which enables us to use low loss dispersive element in the OPO cavity to further reduce the output linewidth of the OPO. Single longitudinal mode operation of the Type-II BBO OPO has been achieved by inserting an intra-cavity solid Fabry Perot etalon at an appropriate location. The time-averaged linewidth of multi-kHz repetition rate, single-mode OPO is measured to be less than 300 MHz.

4.1 Introduction

The free-running Type-I phase-matched BBO OPOs exhibit broad spectral linewidth. The spectral linewidth of Type I BBO OPO varies from 0.2 nm to 0.5 nm as the wavelength is tuned from 490 to 590 nm (discussed in section 3.3.3 of chapter 3) and increases further to few nanometers as the wavelength is tuned toward degeneracy [91]. This outcome is mainly caused by the inherent gain bandwidth of the parametric process which is broad in the Type-I phase-matched

OPOs. Many studies have been subjected to reduce the spectral bandwidth (even down to single longitudinal mode operation) [34, 41, 92, 93, 94, 95] of type-I critical phase-matched BBO based OPOs. However, the improved performance towards a narrow linewidth operation was usually achieved at the expense of increased system complexity and an additional loss in OPO output efficiency.

Alternatively, Type-II phase matching exhibits much narrower linewidth throughout the entire tuning range, typically 0.1 nm to 0.5 nm near degeneracy [32, 50, 91], when pumped by the third harmonic (355 nm) of a Q-switched Nd:YAG pump laser. However, divergence broadening in Type-II phase matching is more predominant and it is much larger than the inherent spectral linewidth arising due to the parametric process. The large divergence broadening exhibited by this Type-II phase matching compared to that by Type-I phase matching is mainly due to the extraordinary wave propagation of the signal wave. This effect causes the asymmetric change of the OPO wavelength with the noncollinear angle of the signal wavelength. Whereas, in Type-I phase matching the OPO signal waves are propagated as an ordinary wave for which the wavelength change is symmetric with the noncollinear angle of the signal wavelength. This theoretical concept was explained by G. Anstett et.al [50] through a wavelength shift curve of type-I and type-II phase-matched, 355 nm pumped signal resonant BBO-OPOs as a function of the non-collinear angle of the signal wave. Consequently, in collinearly type-I phase-matched OPOs divergence broadening is only a small fraction of the gain bandwidth. In Type-II phase-matched OPOs, however, divergence broadening may be many times larger than the gain bandwidth. Therefore, the linewidth of the Type-II phase-matched OPO output is mainly determined by divergence broadening.

G. Anstett et al [50] have developed also a technique for reducing the divergence broadening in which they have double passed the pump beam using a pump beam reflector. Since the pump beam is double passed in the non-linear crystal, the OPO waves are amplified on each pass (in both the forward and backward directions) through the non-linear crystal. Obviously, this increases the effective gain and reduces the oscillation threshold [98, 50]. Furthermore, due to the asymmetric change of the OPO output wavelengths with the non-collinear angle, the non-collinear rays traveling in forward and backward directions experience the gain at different wavelengths. Only collinear rays experience gain at the same wavelength for both passes through the non-linear crystal. Thus, with increasing non-collinear angle the effective gain decreases. As a result, the divergence of the resonant OPO wave decreases, and the reduced divergence causes a smaller divergence broadening.

We have adopted a similar technique of double passing the pump beam in Type-II BBO OPO for reducing the spectral linewidth. Since the pump beam is reflected back, we have restricted the maximum repetition rate of the pump laser at 2 kHz to avoid any damage of intra-cavity optical components and crystal. With this technique, we have achieved a substantial reduction in the OPO spectral linewidth (~ 0.15 nm) across its tuning range. More importantly, double passing the pump beam helped to reduce the operation threshold of the Type-II BBO OPO. This encouraged us to use a low loss dispersive element such as Fabry Perot etalon inside the OPO cavity to further reduce the linewidth down to Single Longitudinal Mode (SLM) operation. The following sections of this chapter describe the development and characterization of high repetition rate, Type-II BBO OPO, and the spectral linewidth reduction technique employed which helped to a demonstration of single longitudinal mode operation of the OPO. The design aspects for the development of SLM

Type-II BBO OPO have been discussed and the developed SLM OPO has been characterized for spectral linewidth across its tuning range.

4.2 High repetition rate Type-II phase-matched BBO OPO

4.2.1 Type II BBO OPO configuration

The Type-II OPOs exhibit high pulse threshold energy and low conversion efficiency because of lower nonlinear coefficient values and larger tuning angles for covering the entire tuning range compared to Type-I [91]. The comparisons of angle dependence and variation of nonlinear coefficient in Type-I and Type-II phase matching are shown in the Fig.4.1. Thus, it is usual to use long and large aperture size non-linear crystals for efficient operation. In this OPO setup, we have used a larger size BBO crystal of dimensions $6 \times 12 \times 20 \text{ mm}^3$, which is cut ($\theta=37^\circ$, $\phi=30^\circ$) for Type-II phase matching and the crystal faces are coated with high damage threshold protective coating film at 355 nm. The measured transmission spectrum of this Type-II BBO crystal is shown in the Fig. 4.2.

The spectral acceptance and angular acceptance bandwidths are calculated using the equations (3.1) (3.2) described in section 3.2.3 of chapter 3 for Type-II interaction (e (pump) \rightarrow o (signal) +e (idler)). The calculated spectral and angular acceptance bandwidths for the pump laser with the internal phase-match angle across the tuning range of Type-II BBO OPO are shown in the Figures. 4.3 (A) and 4.3 (B).

The Type-II BBO OPO setup is similar to the Type-I BBO OPO setup as shown in the Fig.3.1, except the Type-I BBO crystal is replaced with a large size Type-II BBO crystal. The cavity length of the OPO cavity has increased to 30 mm to accommodate the 20 mm long crystal and allow the maximum angular rotation of the crystal to achieve the complete tuning range of the

OPO. The Type-II phase-matched BBO crystal based OPO configuration is shown in the Fig. 4.4. The same cylindrical focusing geometry used for Type-I BBO OPO had employed for the Type-II BBO OPO. As a result, the pump beam intensities are comparable and therefore the gain coefficient. Hence, the same OPO cavity mirrors used in Type-I BBO OPO had employed for the Type-II BBO OPO cavity. The thermal focusing in the crystal can be neglected as it is calculated to be $\sim 10\text{m}$ using the equations described by et.al [96], for the pump laser operating the power of 12 W at a repetition rate of 5 kHz

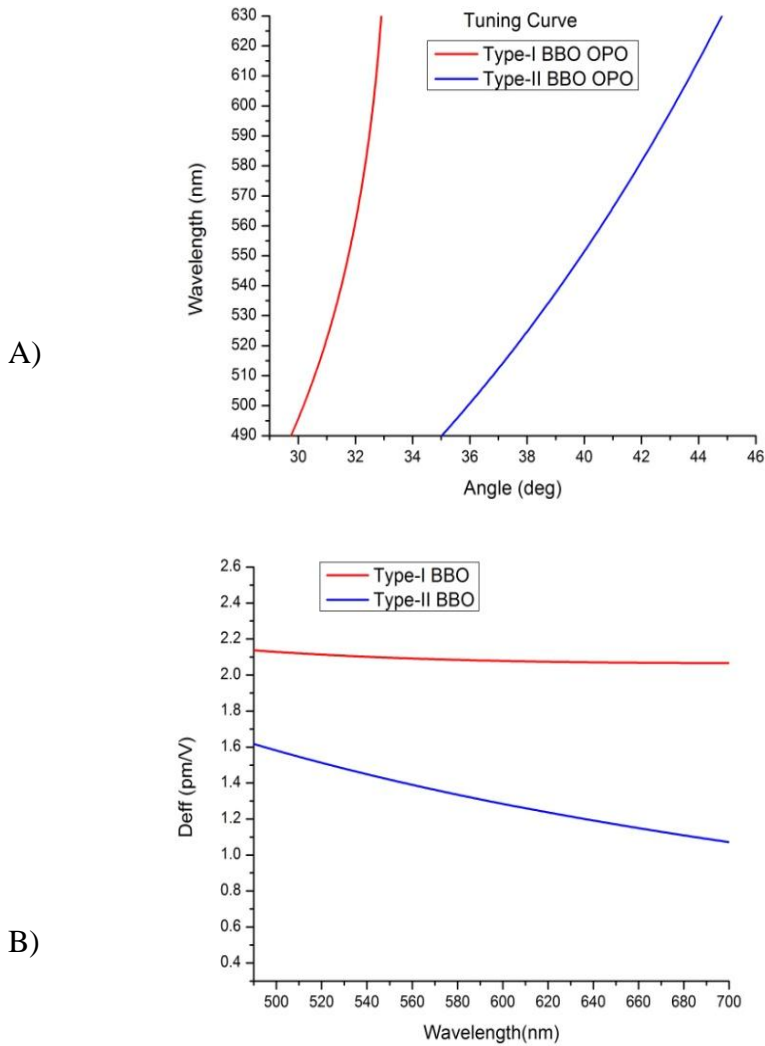


Fig.4.1: Comparison of A) Angle dependence wavelength tuning and B) Nonlinear coefficient in Type-I and Type-II phase matching, pumped at 355 nm [59].

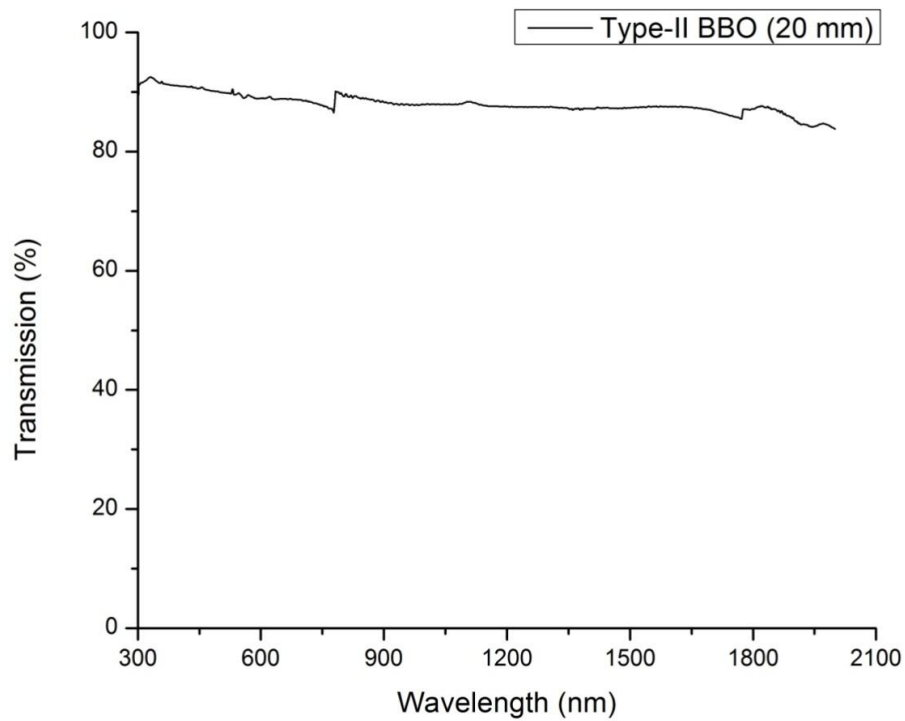
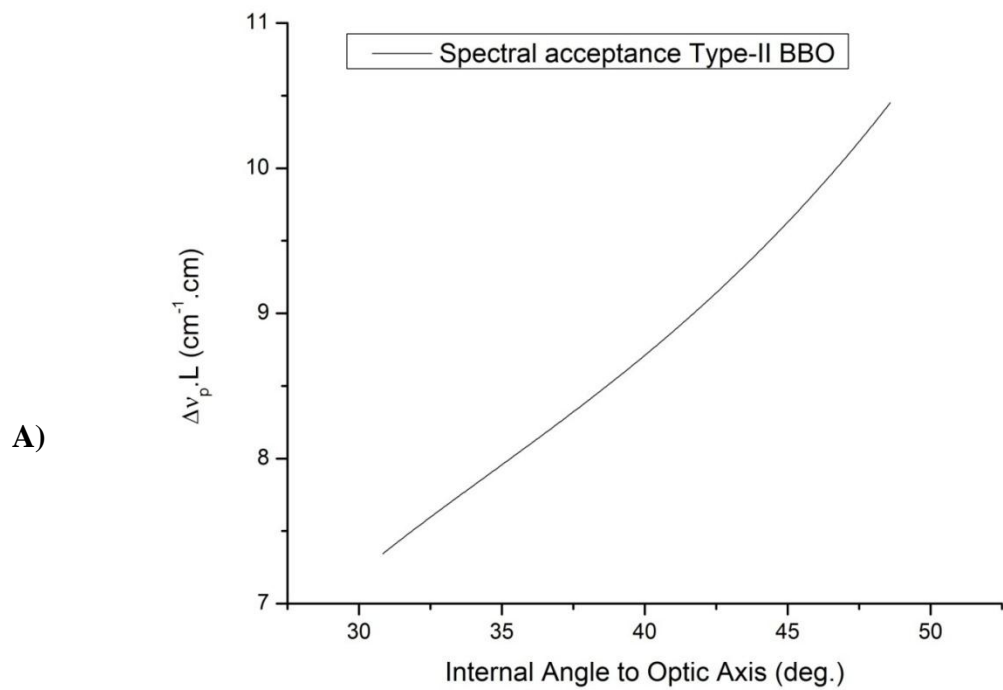


Fig.4.2: Measured Transmission spectrum of the Type-II BBO crystal used in the OPO setup.



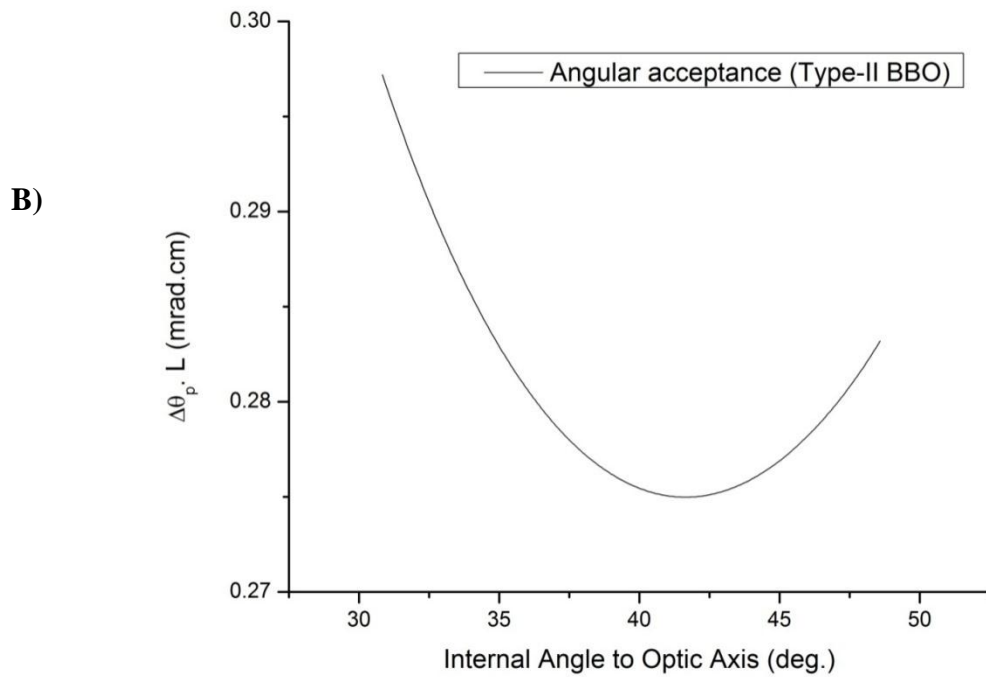


Fig.4.3: Calculated A) Spectral acceptance bandwidth B) angular acceptance bandwidth of the Type-II BBO OPO across the tuning range.

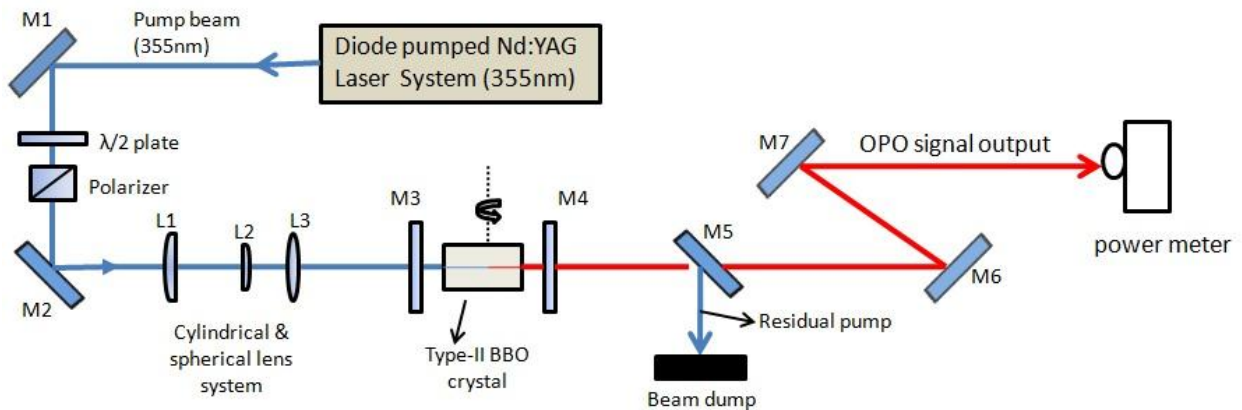


Fig.4.4: Schematic of the Type-II phase matched BBO crystal OPO used for narrowband operation

4.2.2 Performance of the Type-II BBO OPO

4.2.2.1 Dependence of output power on the repetition rate of the pump laser

The signal output from Type-II BBO crystal OPO can be continuously tuned from 490 nm to 630 nm with an angular variation of 10 degrees. The performance of the OPO signal output is studied at the peak wavelength of 512 nm, for different repetition rates of the pump laser. The Fig. 4.5 shows the theoretical and experimentally measured wavelength tuning of the signal wave with a change in internal angle to the optic axis of Type-II BBO OPO. The variation of the signal output power is measured while the pump laser is operated at different repetition rates (1 to 4 kHz) as a function of input pump power, which is illustrated in Fig 4.6. The OPO output signal power is observed to increase with the input pump power. However, the performance of the OPO starts to degrade if the UV pump beam excited OPO is operated beyond 3 kHz PRF. The threshold pulse energy of our Type-II BBO OPO system is ~1 mJ and we have obtained a slope efficiency of about 23 % when operated with the pump laser (355 nm) at 3 kHz. The output power of the OPO is observed to be very unstable and fluctuating with time if we operate the pump laser beyond 3 kHz, and the pulse energy is more than 2 mJ. The degradation of the OPO output power is found to originate mainly to the increased residual absorption of pump beam resulting in inhomogeneous heating of the crystal, which is discussed in chapter 5 of this thesis.

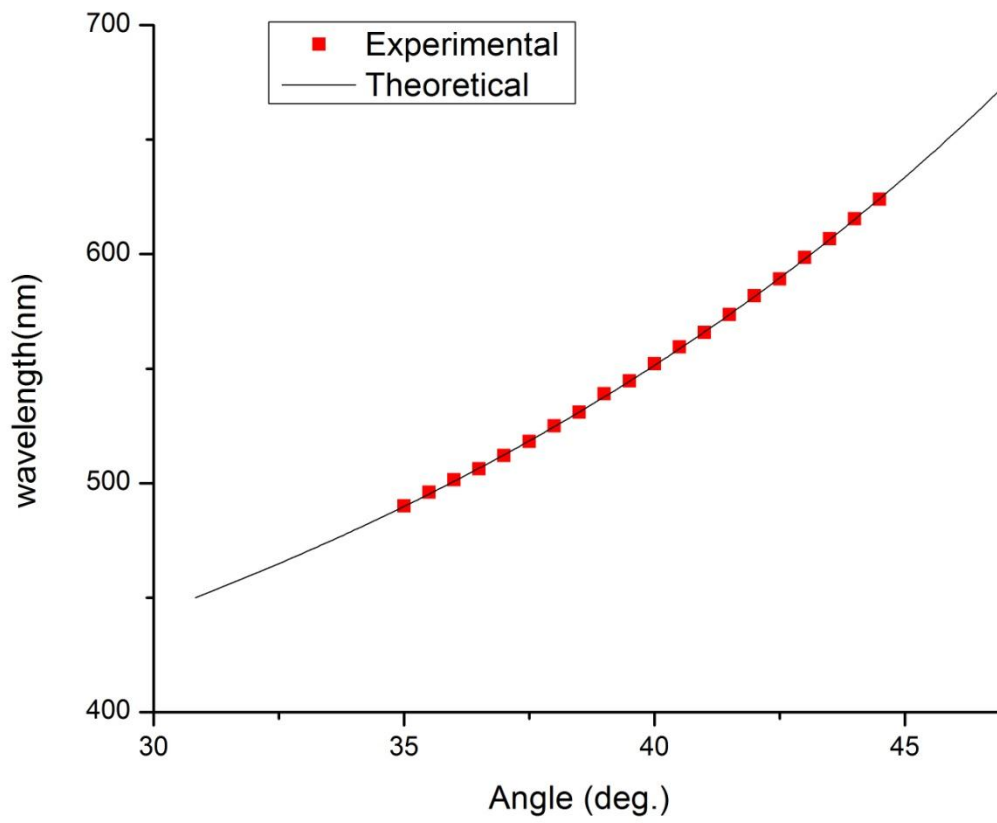


Fig.4.5: Wavelength tuning curve of the signal wave with change in internal angle to the optic axis of Type-II BBO OPO.

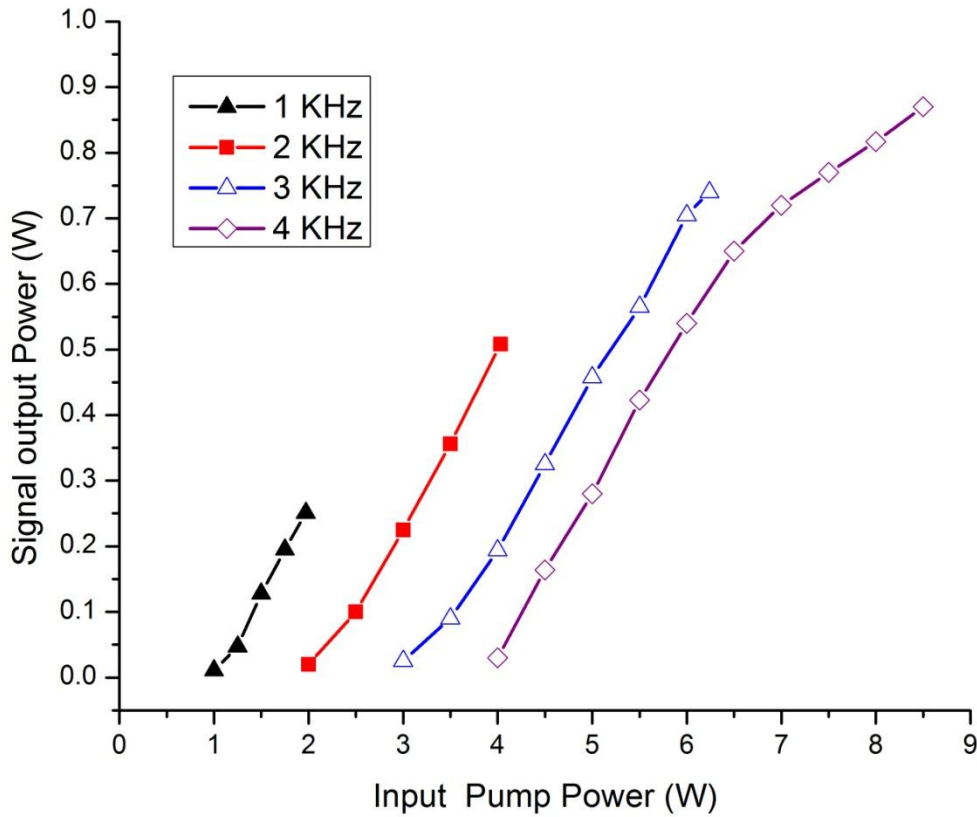


Fig.4.6: Signal output performance of the Type-II BBO OPO at different repetition rates of the pump laser.

4.2.2.2 Spectral linewidth of the OPO

The spectral linewidth of the Type-II BBO OPO signal output is measured at different wavelengths of the tuning range from 490 nm to 590 nm at a PRF of 2 kHz. The variation of linewidth with wavelength is illustrated in the Fig.4.7. The spectral linewidth of this free-running OPO varies between 0.53 nm to 0.65 nm across its tuning range. The spectrometer can measure the signal output with a resolution of 0.035 nm. The spectral linewidth of the 355 nm pumped Type-II BBO OPO across the tuning range of the signal wave is theoretically calculated by using

the Equations (3.3) and (3.4) discussed in section 3.3.3 in chapter 3 for Type-II interaction. In the calculations, we have considered the divergence of the pump beam is 0.15 mrad. The Fig. 4.8 shows the comparison of the theoretical and experimentally observed spectral linewidth of the Type-II BBO OPO across the tuning range of the signal wave. The deviation in the experimentally observed spectral linewidth results when compared to theoretical results is mainly due to the inaccuracy in the measurement of spectral linewidth with a low-resolution spectrometer (HR 2000 plus, Ocean Optics).

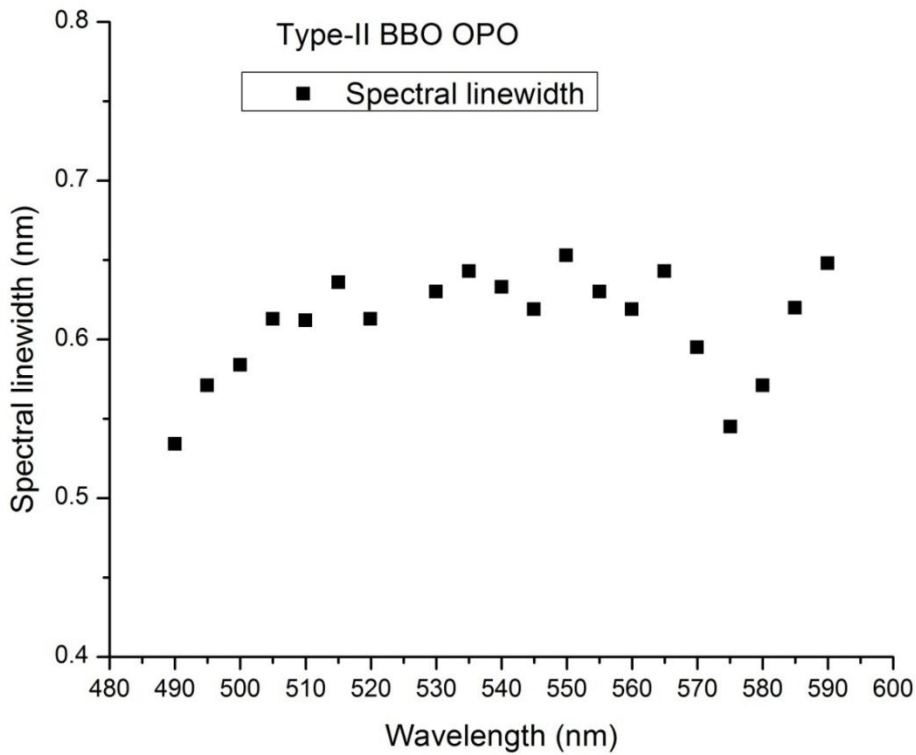


Fig.4.7: Spectral linewidth of Type-II BBO OPO as a function of signal wavelength.

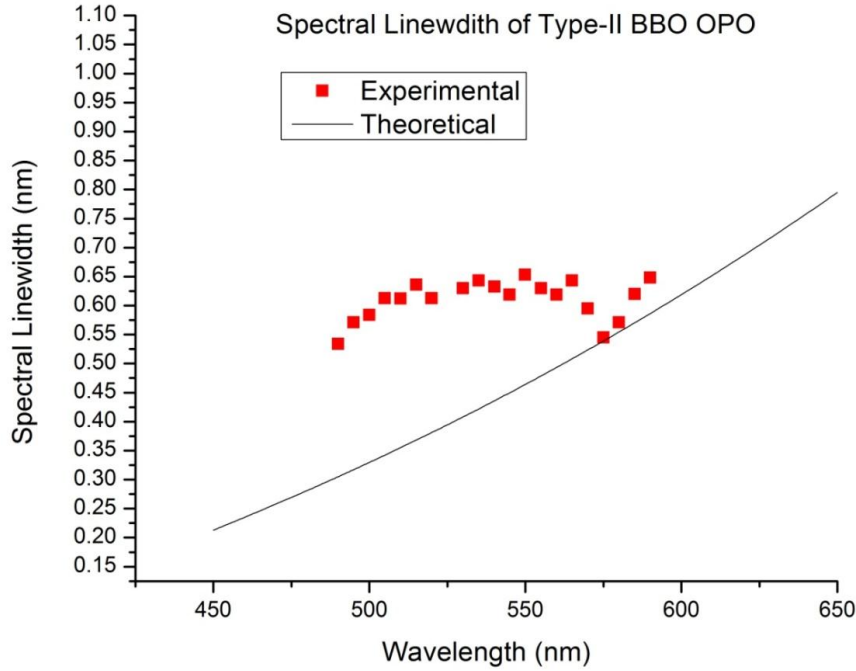


Fig.4.8: Comparison of theoretical and experimental observed spectral linewidth of Type-II BBO OPO across the tuning range of the signal wave.

To determine the contribution of divergence of the pump on the resulting spectral linewidth of the Type-II BBO OPO, calculated the spectral linewidth arising due to the angular divergence of the pump beam and oscillator gain bandwidth. The spectral linewidth due to the divergence of the pump beam in Type-II phase matching is given by [97],

$$\Delta\nu_{div} \approx \frac{\left(\frac{c}{2\lambda_p}\right) \left(\frac{\partial n_p}{\partial \theta}\right)_0 \delta\theta_p}{\left[n_s^0 - n_i^e(\theta) + \lambda_s \left(\frac{\partial n_s}{\partial \lambda_s}\right) - \lambda_i \left(\frac{\partial n_i^e(\theta)}{\partial \lambda_s}\right)\right]} \quad 4.1$$

The spectral linewidth of the OPO is mainly determined by the oscillator gain bandwidth which is in turn determined by crystal birefringence and dispersion is given by,

$$\Delta\nu_{gain\ bandwidth} \approx \frac{c}{l [n_s^o - n_i^e(\theta) + \lambda_s \left(\frac{\partial n_s}{\partial \lambda_s}\right) - \lambda_i \left(\frac{\partial n_i^e(\theta)}{\partial \lambda_s}\right)]} \quad 4.2$$

Where n_s^o and n_i^e are the refractive indices at the signal and idler wavelengths respectively, λ_s and λ_i are wavelengths of the signal and idler wavelengths respectively and c is the speed of light. The spectral broadening due to pump beam divergence and gain bandwidth in Type-II phase matching BBO OPO across the tuning range of the OPO was calculated using the Equations (4.1) and (4.2) respectively. The Fig. 4.9 shows the comparison of the spectral linewidth of the OPO across the tuning range arising due to these two factors. From this comparison of the spectral linewidth, it is evident that in Type-II phase matching the spectral linewidth of the OPO strongly depends on the pump beam divergence. As a result, the small change in the spectral linewidth of the Type-II BBO OPO, due to increase in the repetition rate from 1 kHz to 3 kHz and pump pulse energy from 1.5mJ to 2.5 mJ (since the available pump pulse energy is only 2.5 mJ) was not able to measure using the low resolution spectrometer which can measure only the spectral linewidth above 0.1 nm. Hence, to operate the Type-II BBO OPO at much reduced linewidths limited by the inherent nonlinear process of the crystal the divergence broadening pump beam has reduced to a much lower value.

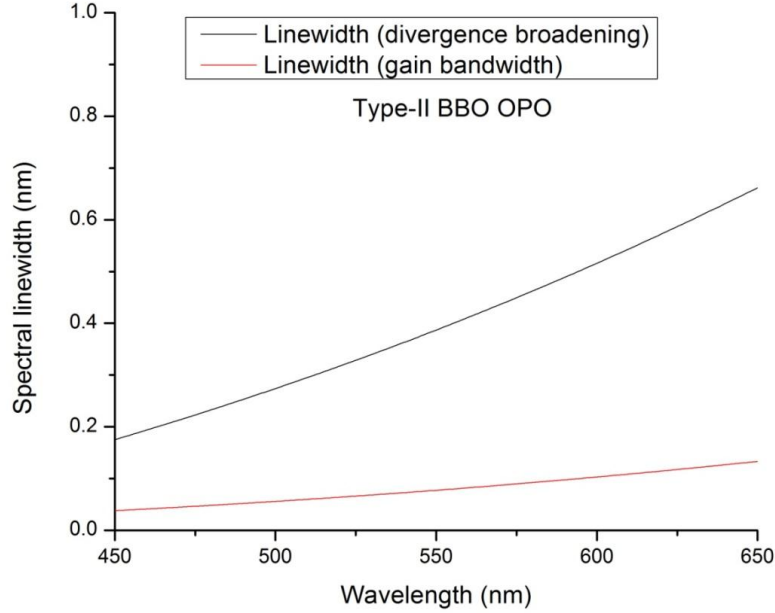


Fig.4.9: Comparison of calculated Spectral Linewidth of Type-II BBO OPO arising due to divergence and inherent parametric process.

4.2.2.3 Beam quality

The Fig. 4.10 shows the near and far-field profiles and M^2 factor of the Type-II BBO OPO measured at a signal wavelength of 512 nm at a repetition rate of 4 kHz at 2 mJ pulse energy. The M^2 factor at this signal wavelength is measured to be $M^2_x = 6.4$ and $M^2_y = 3.9$. The difference in the position of the beam in the x and y direction is due to astigmatism introduced by the cylindrical optics.

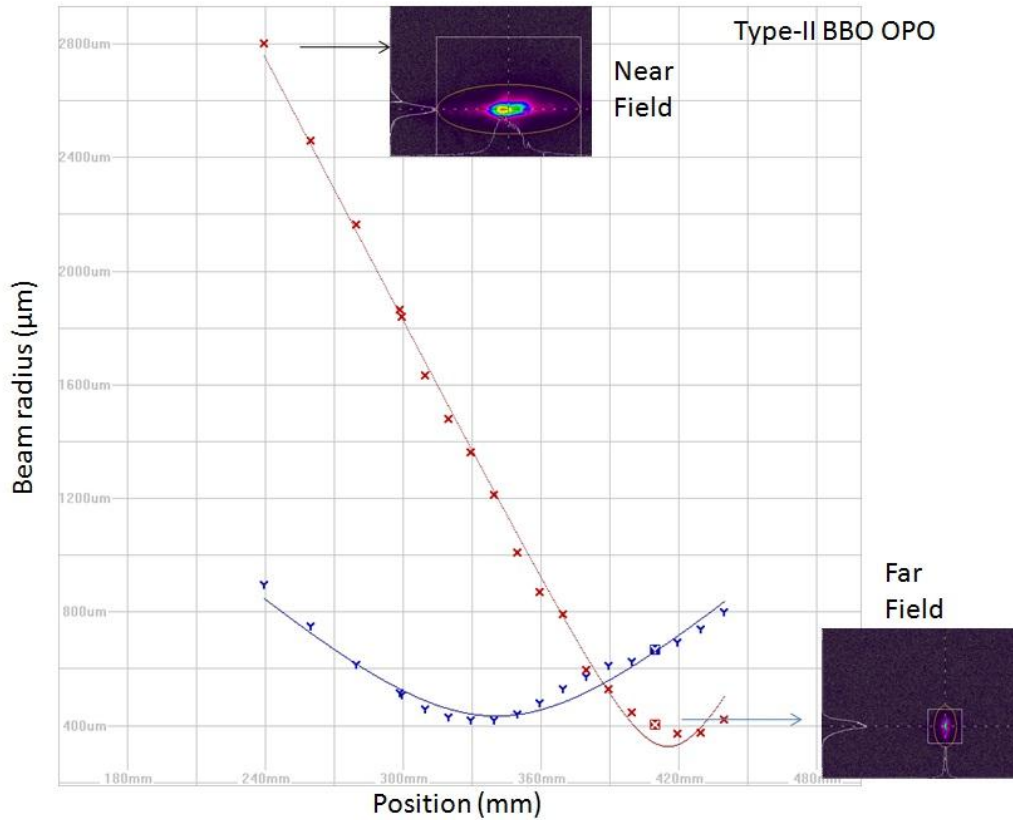


Fig.4.10: The measured M^2 factor, near and far field profiles of the OPO signal beam at a wavelength of 512 nm at a repetition rate of 4 kHz.

4.3 Reduction of spectral linewidth of Type II BBO OPO

4.3.1 Type-II BBO OPO with double pass pump beam configuration

The spectral linewidth of the pulsed OPO's signal output depends on pump beam spectral linewidth, OPO cavity length, and divergence of the generated signal output [65, 99]. The Type-II phase matching OPO's exhibit much narrower linewidth in comparison to Type-I phase matching

OPO's [91, 50]. However, the influence of divergence of the resonant signal wavelength to the spectral linewidth in Type II phase matching is more than that of Type-I phase matching due to asymmetric change of the resonant OPO wavelength with non-collinear angle [50]. Hence, in the case of Type-II phase matching OPO's, divergence broadening mainly determines the spectral linewidth of the signal output.

Therefore, the increase in the spectral linewidth of Type-II BBO OPO when compared to Type-I BBO OPO is mainly due to divergence broadening. In order to reduce the divergence of the generated signal output, we have placed a pump beam reflector inside the Type-II BBO OPO cavity in between the crystal and output coupler for double passing the pump beam inside the crystal as shown in the Fig. 4.11. The pump beam reflector is a flat mirror, dielectric coated for high reflectivity ($> 99\%$) at 355 nm for normal incidence and high transmission for signal and idler wavelengths. The advantage of double passing the pump beam configuration is that it will not only increase the gain of the signal because of the amplification of signal wave in both forward and backward directions and therefore decreases the oscillation threshold [98, 65], but also decreases the divergence of the resonant signal wave as discussed in ref [50]. Reduction of the divergence of the resonant signal wave narrows the spectral linewidth to its inherent spectral linewidth arising mainly due to the parametric process of the OPO. Even though the pump beam is reflected back into the cavity, it was observed that reflected pump beam was not coupled back into the pump laser cavity because the reflected cylindrical focused pump beam from the OPO cavity observed to increase its beam size to a large value after retracing through the cylindrical focusing system. Hence only a fraction of the reflected pump beam coupled into variable attenuator, which is a combination of a polarizer and a half-wave plate prevents the pump beam entering into the laser. The use of Faraday isolator would be the ideal choice for blocking the back

reflected/ scattered pump beam completely. However, the losses due to the insertion of the Faraday isolator will further reduce the available pump pulse energy.

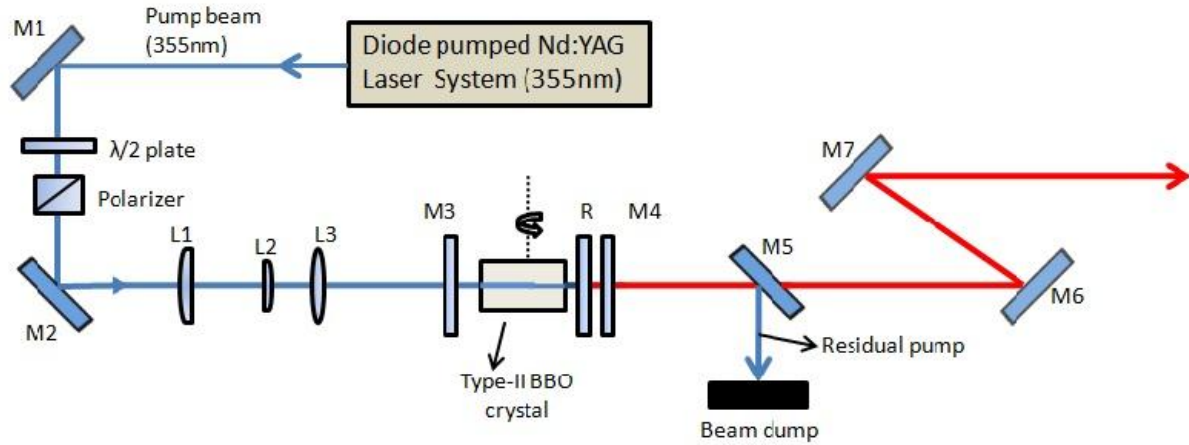


Fig.4.11: Schematic of the Type-II BBO OPO with double pass pump geometry. M1, M2: Pump beam routing mirror, M3, M4: OPO cavity mirrors, M5: Pump beam reflector, M6, M7: Signal beam reflectors, R: Pump beam reflector.

4.3.2 Performance characteristics of Type II BBO OPO in double pass pump configuration

4.3.2.1 Spectral linewidth of the OPO

The spectral linewidth of the signal output from Type-II BBO OPO with double pass configuration of the pump beam is measured at different wavelengths of the tuning range from 490 to 590 nm at a repetition rate of 2 kHz. A comparison of the spectral linewidth of the signal wavelengths obtained from all three OPO setups (Type-I BBO OPO, Type-II BBO OPO and Type-II BBO OPO with pump beam double pass configuration) are shown in the Fig.4.12. By employing

pump beam double pass configuration for Type-II BBO OPO, the spectral linewidth of the signal output is reduced by a factor of 4 when compared to free running Type-II BBO OPO.

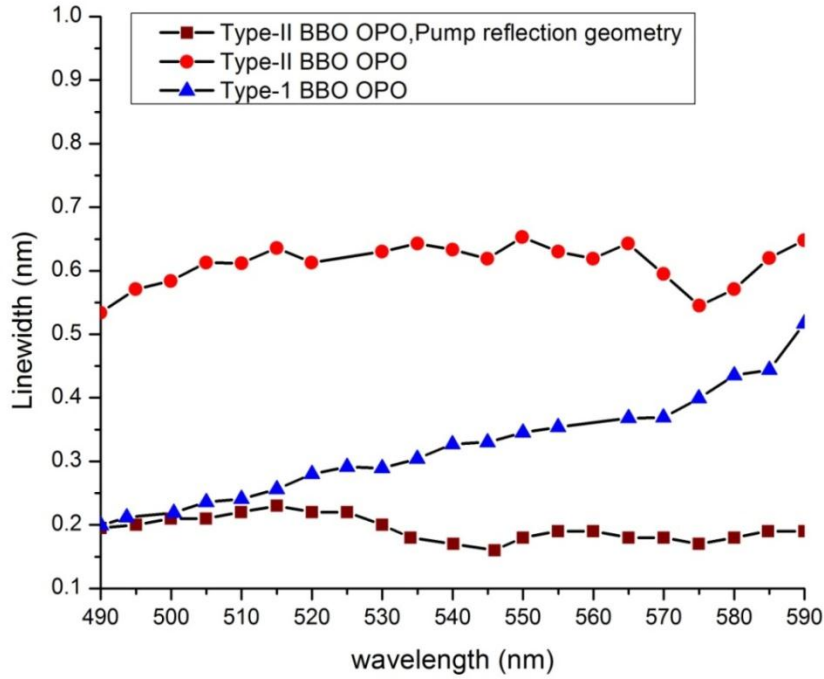


Fig.4.12: Comparison of spectral linewidth of Type-I, Type-II BBO and Type-II BBO OPO using pump double pass configuration.

4.3.2.2 Conversion efficiency

The performance of the Type-II BBO OPO with pump double pass configuration is compared with the free-running Type-II BBO OPO at a signal wavelength of 512 nm when the pump laser is operated at a repetition rate of 2 kHz. The variation of signal output power measured with input pump power for both the OPO setups is shown in the Fig.4.13. The performance of the OPO is found to improve in pump double pass configuration when compared to free-running operation. In pump double pass configuration, the OPO operates at a maximum output power of 800 mW at 2 kHz repetition rate with a conversion efficiency of 18.2 % at 512 nm and the threshold power is around 1.5, whereas, in free-running operation, the conversion efficiency drops to 15 % and the threshold power is increased to 2 W.

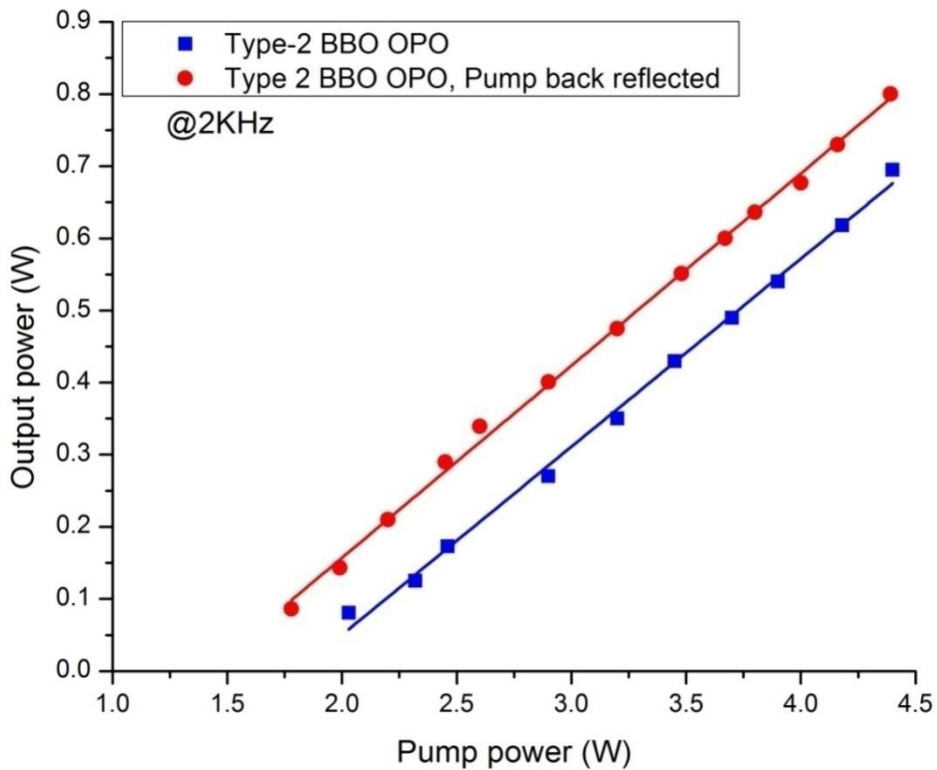


Fig.4.13: Performance comparison of Type-II BBO OPO using pump double pass configuration.

4.3.2.3 Beam quality

The Fig. 4.14 shows the near and far-field profiles and M^2 factor of the Type-II BBO OPO in double pass configuration, measured at a signal wavelength of 560 nm at a repetition rate of 2 kHz. The M^2 factor at this signal wavelength is measured to be $M_x^2 = 5.0$ and $M_y^2 = 2.5$.

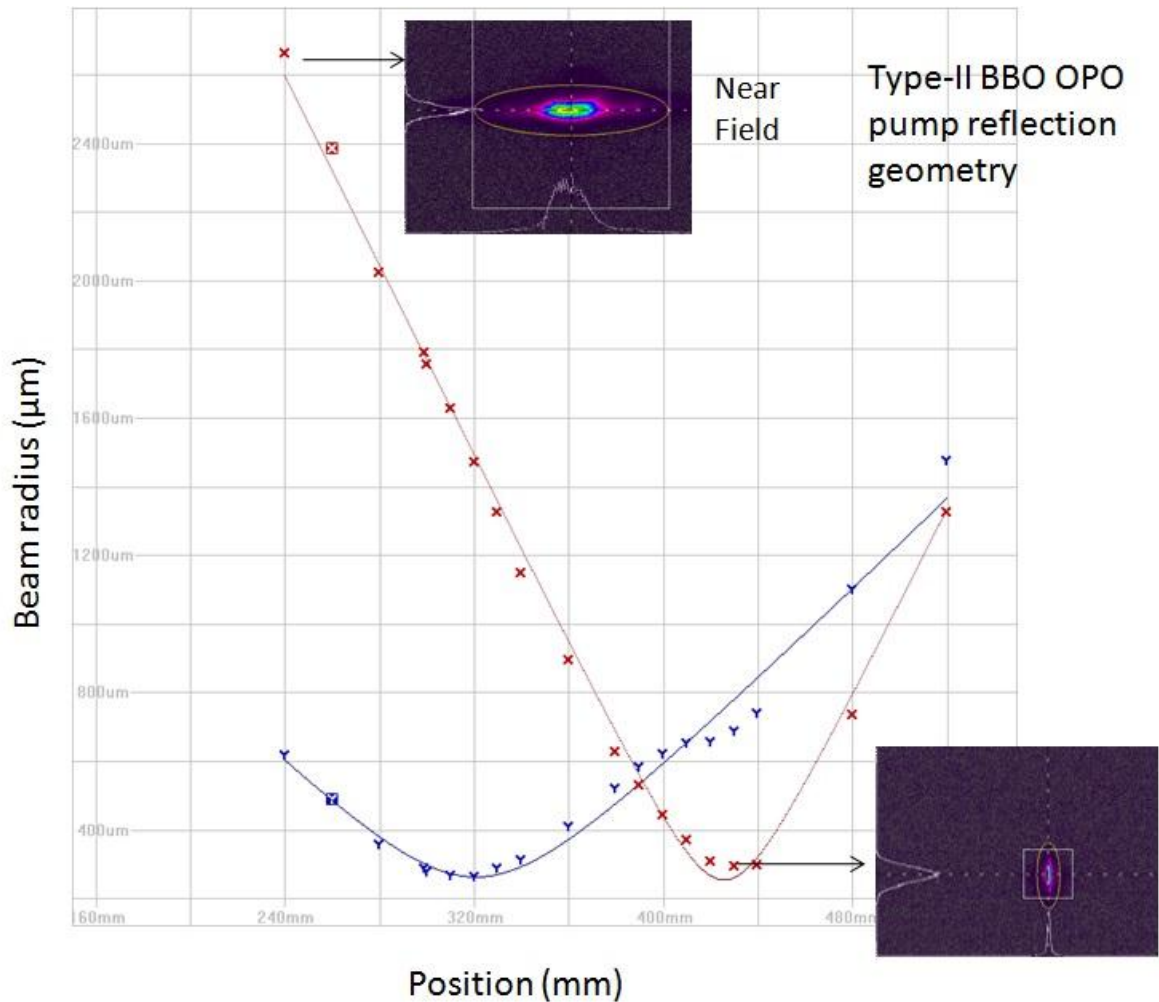


Fig.4.14: The measured M^2 factor, near and far field profiles of the Type-II BBO OPO signal beam at a wavelength of 560nm at a repetition rate of 2 kHz.

4.4 High repetition rate Single Longitudinal Mode (SLM) Type II BBO OPO

4.4.1 Design of SLM Type II BBO OPO

Consequent to the reduction of spectral linewidth and threshold of Type-II BBO OPO by employing double pass pump geometry, as discussed in section 4.3.2 of this chapter 4, we have intended to insert a low loss dispersive element such as a thin Fabry-Perot etalon in the OPO cavity to operate the OPO in single longitudinal mode (SLM). The tilted etalon has no reflection loss for frequencies corresponding to its Fabry-Perot transmission maxima. At other frequencies, the reflections from this etalon suffered loss from the cavity, and thus constitute a frequency-dependent loss mechanism. For achieving single-mode operation, the tilted Fabry-Perot etalon must have adequate selectivity to suppress axial modes in both sides adjacent to the desired one. Further, its free spectral range must be large enough so that the gain of the laser is sufficiently reduced at its adjacent axial modes resonance.

The schematic of the Fabry Perot etalon based SLM Type-II BBO OPO cavity configuration is shown in the Fig. 4.15. The etalon is placed at an angle θ to the resonator axis, after the pump beam reflector in the Type-II BBO OPO cavity with double pass pump configuration. This design has the advantage of rugged operation by avoiding optical damage due to the direct impact of pump beam intensity on the etalon. The transmission maxima of the etalon occur at frequencies ν_n is given by [100],

$$\nu_n = \frac{nc}{2n_r L_1 \cos \theta'} \quad 4.3$$

where n is an integer, θ' is the refraction angle of the beam within the etalon, n_r is the etalon refractive index, and L_1 is its length. The tilting angle θ has to be adjusted so that the transmission

peak of the etalon has to coincide with the mode nearest the peak of the OPO gain profile as shown schematically in the Fig. 4.16.

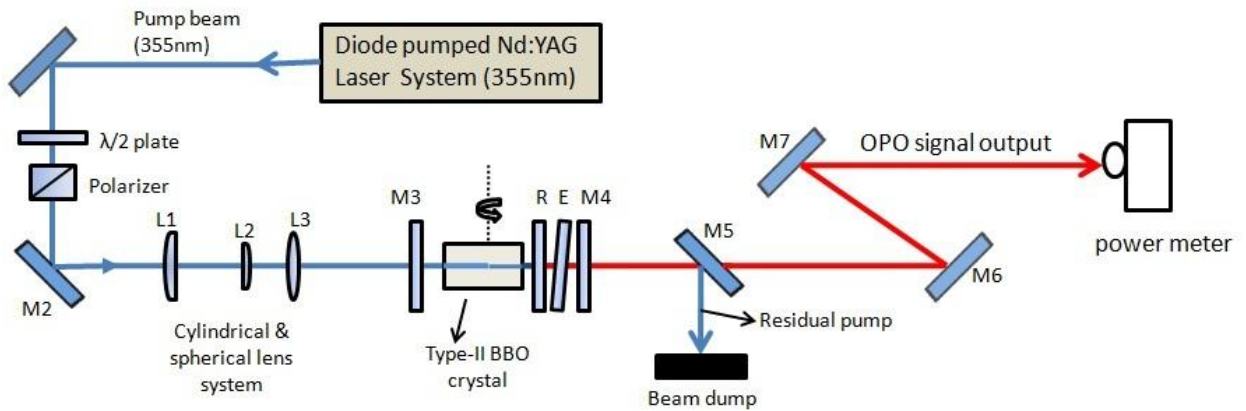


Fig.4.15: Schematic of the Fabry Perot etalon based SLM Type-II BBO OPO, E represents etalon.

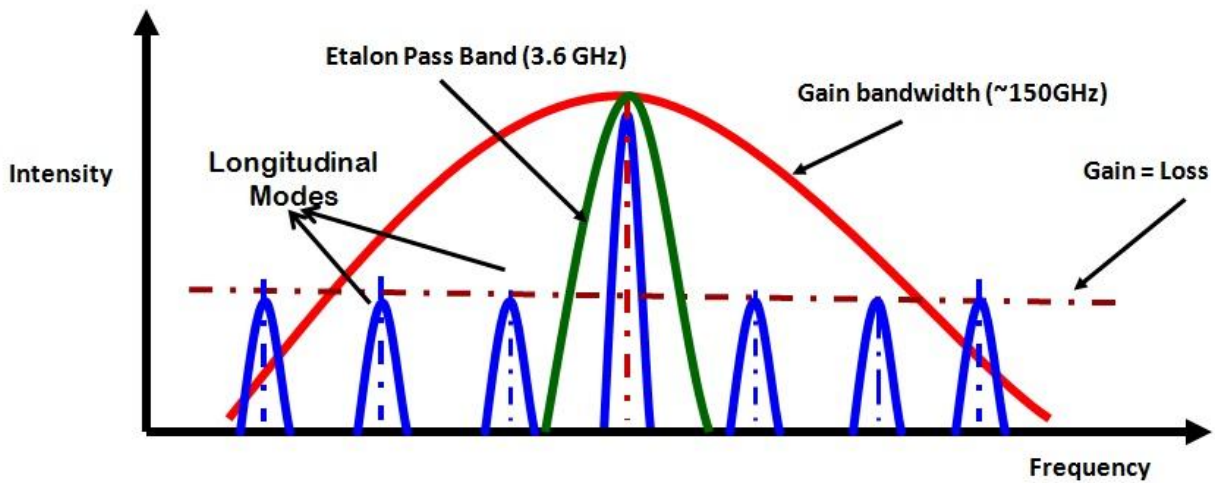


Fig.4.16: Schematic of the single longitudinal mode selection using an intra-cavity FP etalon.

It is well understood that if the frequency separation $\Delta\nu = c/2L$ between two adjacent longitudinal modes is $> \Delta\nu_c/2$, where $\Delta\nu_c$ is the linewidth of an etalon transmission peak, then the etalon selects the mode nearest to line center from its neighbors. The discrimination between adjacent longitudinal modes requires,

$$\frac{\Delta\nu_c}{2} = \frac{\Delta\nu_{\text{fsr}}}{2F} \leq \Delta\nu \quad 4.4$$

where $\Delta\nu_{\text{fsr}}$ is the free-spectral range and F is the finesse of the etalon. To ensure single longitudinal mode operation, we also require the etalon free-spectral range $\Delta\nu_{\text{fsr}}$ to be larger than or equal to half the gain linewidth $\Delta\nu_0$ of the OPO; otherwise, the two neighboring transmission peaks of the etalon passband would allow corresponding cavity modes to oscillate. Discrimination between adjacent transmission maxima of the etalon then requires,

$$\Delta\nu_{\text{fsr}} \geq \frac{\Delta\nu_0}{2} \quad 4.5$$

From the above Equations (4.4) and (4.5), in order to achieve single mode operation using Fabry Perot etalon, the length of the OPO cavity must satisfy,

$$L \leq \left(\frac{c}{\Delta\nu_0} \right) 2F \quad 4.6$$

Considering these in our design for achieving single mode operation in Type-II BBO OPO, we have used a 20 mm diameter solid fused silica etalon (SLS optics LTD) inside the cavity. The thickness of the etalon is 1.3 mm which corresponds to the Free Spectral Range ($\Delta\nu_{\text{fsr}}$) of 79 GHz. The Finesse of the etalon is 22 @ 500-600 nm. The corresponding linewidth of an etalon transmission peak ($\Delta\nu_c$) is 3.59 GHz. Following the conditions discussed in equations (4.4) and (4.5) for achieving the single mode operation, the optical cavity length of the OPO is restricted to 75 mm which is well within the limit calculated from the equation (4.6) for the gain bandwidth ($\Delta\nu_0$) of ~150 GHz. Because of the use of large size (20 mm) Type-II BBO crystal increases the

thermal loading and deteriorates the performance as shown in the Fig.4.6 when operated the pump laser above 3 kHz repetition rate at pulse energy $> 2\text{mJ}$. Moreover, the beam reflection geometry employed for reducing the spectral linewidth of the OPO restricts the operation of the SLM OPO to a maximum of 1 kHz repetition rate.

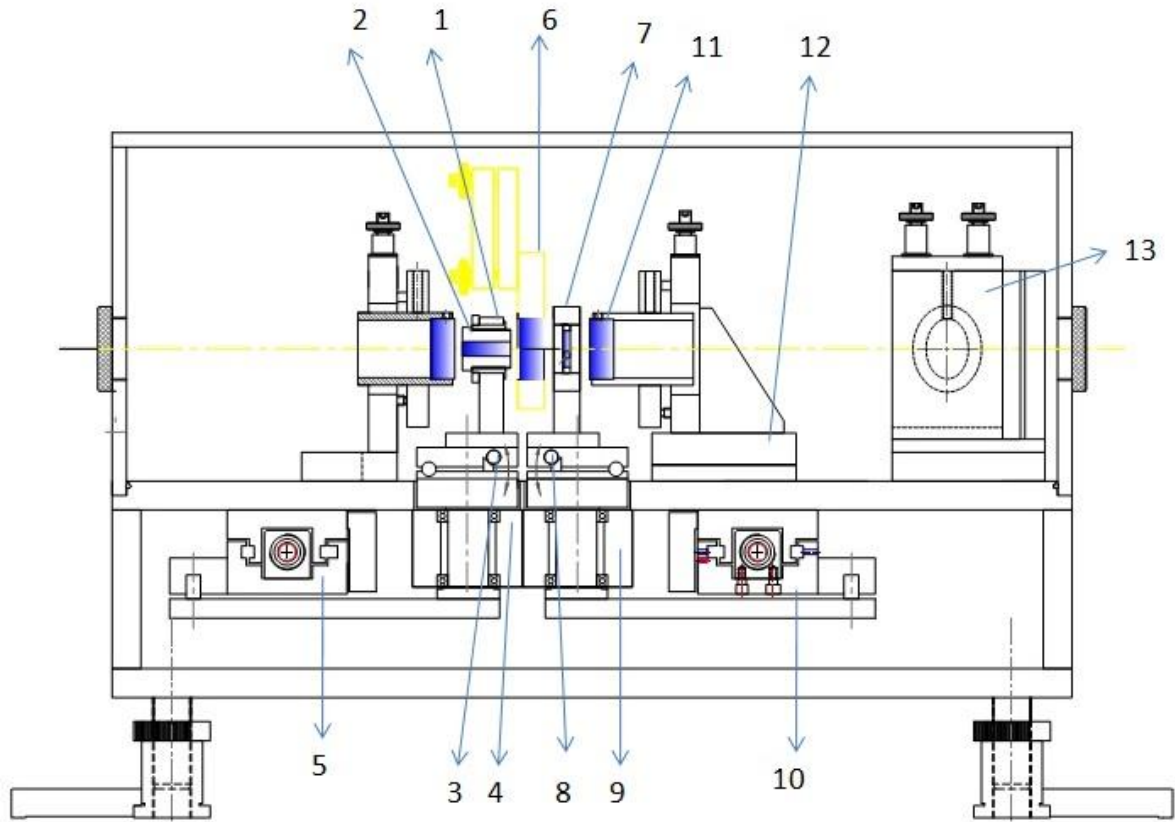
4.4.2 Development of automated SLM OPO Module

In this design of SLM OPO, the etalon tilt is to be adjusted for continuous tuning of OPO output wavelengths by tuning the crystal. Therefore, an automated SLM operation mechanism of our developed OPO over its wide wavelength tuning range has been worked out. A drawing of the implemented optomechanical design of SLM Type-II BBO OPO module is shown in the Fig. 4.17. The optical components of the OPO module are mounted on a rigid platform to avoid the mechanical vibrations. The BBO crystal, as shown in the Fig. 4.17, is mounted in a custom made three axes position holder which provides 360 deg. roll, precise yaw adjustment over a range of ± 10 deg. and pitch adjustment over a range of ± 2 deg. for precision optical alignment and wavelength tuning. The coarse wavelength tuning of the SLM OPO is accomplished through the stepper motorized rotation of the crystal with an angular resolution of $1 \mu\text{rad}$. The etalon is mounted in an optical holder which provides precise adjustments of yaw over a range of ± 5 deg. and pitch over a range of ± 2 deg. The angular rotation of the etalon provides the fine adjustment of etalon transmission peak to coincide with the peak of the OPO cavity gain bandwidth which is achieved through the computer-controlled stepper motorized rotation with an angular resolution of $1 \mu\text{rad}$. The fine wavelength tuning and the frequency stability of the SLM OPO are achieved by OPO end mirror which is mounted on an $8 \mu\text{m}$ PZT driven translation stage.

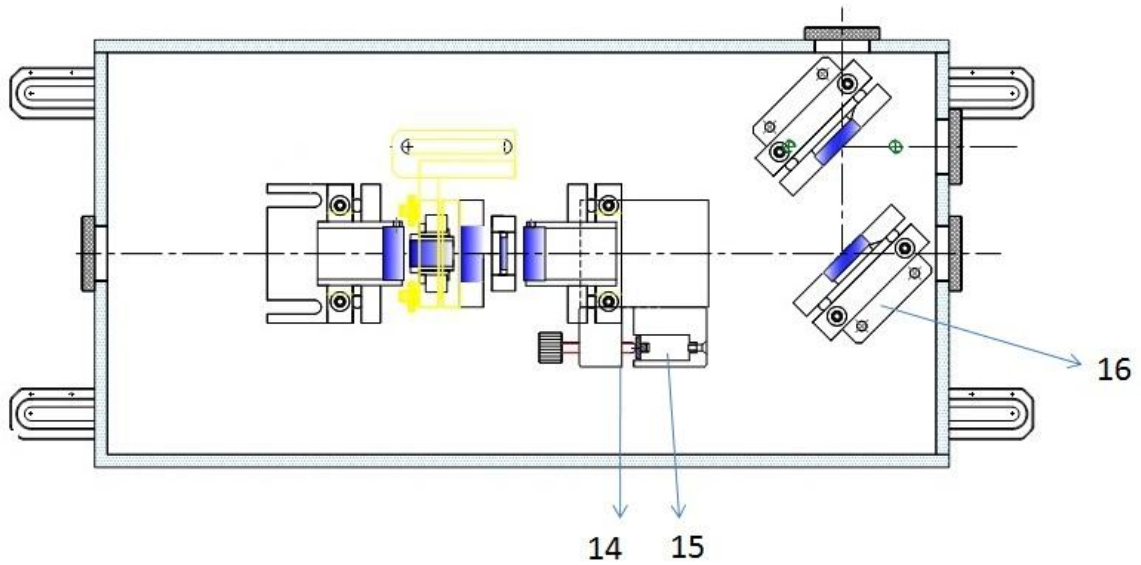
The change in the frequency due to the change in the cavity length is given by,

$$-\frac{\Delta\nu}{\nu} = \frac{\Delta\lambda}{\lambda} = \frac{\Delta L}{L} \quad 4.7$$

The maximum change in frequency achieved with a full 8 μm change in the cavity length due to PZT translation is ~ 63 MHz. The PZT is controlled through a PZT controller (Thor Labs Inc.) with a resolution of 1 nm that corresponds to a minimum controllable change in the frequency of 7.8 MHz. It may be noted that for achieving mode hop free SLM tuning of the OPO, the etalon tilt angle and the cavity length has to be tuned synchronously. For locking the wavelength at a fixed value, we have developed wavelength locking software which acquires the wavelength data from the commercial wavemeter and generates an error signal corresponding to the change in the wavelength value from the set value. The error signal is then sent to the feedback control loop of PZT to change the cavity length of the OPO to set the desired wavelength value. We have presented the preliminary test results of frequency stabilized long term operation of the OPO under wavelength locking, discussed in section 4.4.3.2. The system performance depends on the precision of the optics, their mounts and their positioning accuracy [101]. Hence, all the optical mounts are specially designed and developed for achieving reliable and highly stable SLM operation of the OPO.



A)



B)

Fig.4.17: Opto-mechanical drawing of the automated SLM Type-II BBO OPO module. A) Side view of the OPO module B) Top view of the OPO module.

1. Three axis position holder for crystal
2. 360 deg. Roll control for the crystal holder
3. ± 2 deg. Pitch control for the crystal holder
4. Stepper motor actuator for the Yaw control movement of crystal holder
5. Stepper motor for the crystal holder
6. Pump beam reflector mount
7. Solid etalon holder
8. ± 2 deg. pitch control for the etalon holder
9. Stepper motor actuator for the yaw control movement of etalon holder
10. Stepper motor for the crystal holder
11. Back mirror mount
12. PZT controlled translation stage for the back mirror
13. OPO signal beam routing mirror mounts
14. PZT actuator for the translation stage
15. Piezoelectric transducer (PZT)
16. OPO signal beam routing mirror mounts

4.4.3 Performance characteristics of SLM OPO

4.4.3.1 Spectral characterization of SLM OPO

The spectral analysis of the SLM, Type-II BBO OPO output is carried out by using Fabry Perot etalon based interferometer setup and wavelength meter (WS Ultima (WS-U), High Finesse, Germany). The schematic of the Fabry Perot interferometer setup is shown in the Fig. 4.18. The FP etalon (SLS Optics) with an FSR of 4.5 GHz and a finesse of 30 has been used in this experiment. For this purpose, a sampled beam from the SLM-OPO output is launched into an FP etalon setup as shown in the Fig. 4.18 using an optical fiber assembly. The FP etalon generated interferograms are imaged onto a CCD camera sensor using a 300 cm focal length imaging lens. Fig. 4.19 (A) shows the FP etalon interferograms of SLM OPO output operating at a wavelength of 550 nm at a repetition rate of 1 kHz and (B) shows the interferogram of the frequency stabilized He:Ne laser obtained with the same 4.5 GHz FP interferometer. The Fig. 4.20 illustrates the intensity plot of the horizontal pixel scan of the fringe pattern across the diameter.

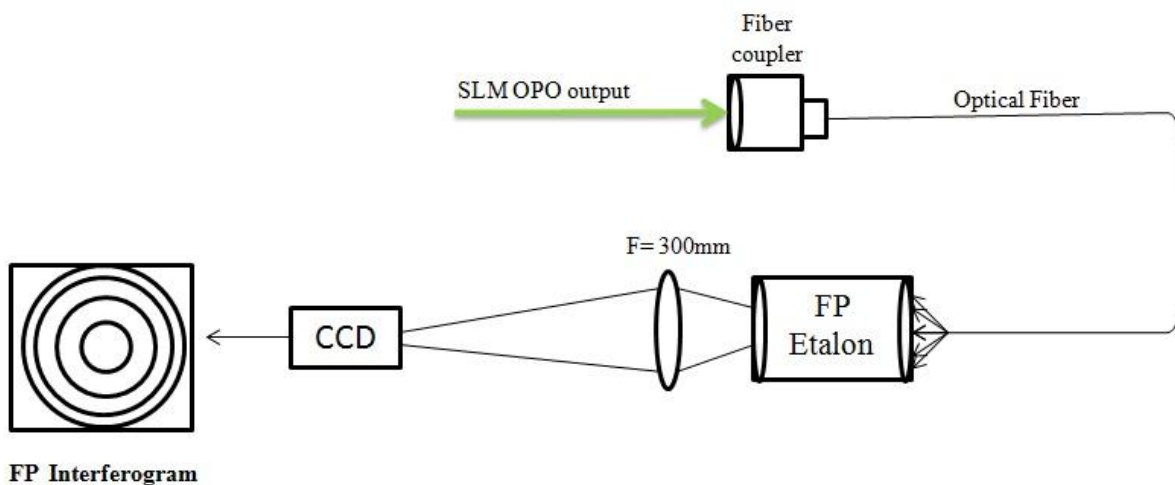
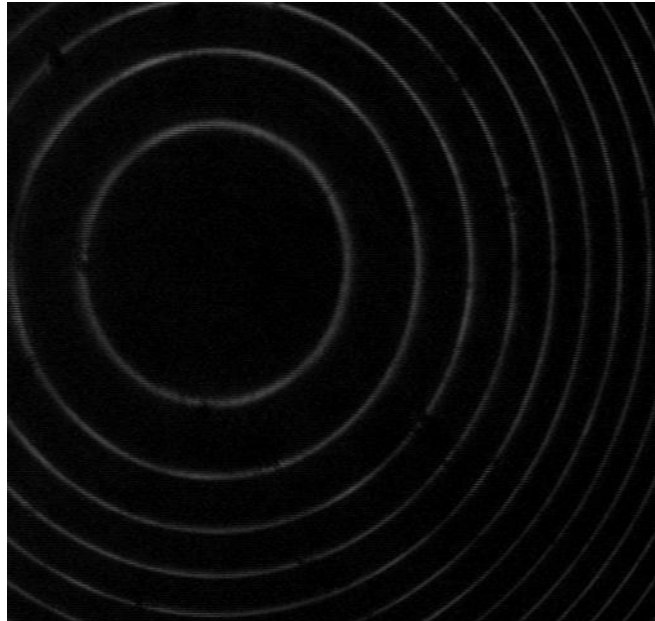


Fig.4.17: Schematic of the FP etalon based spectral measurement technique.

A)



B)

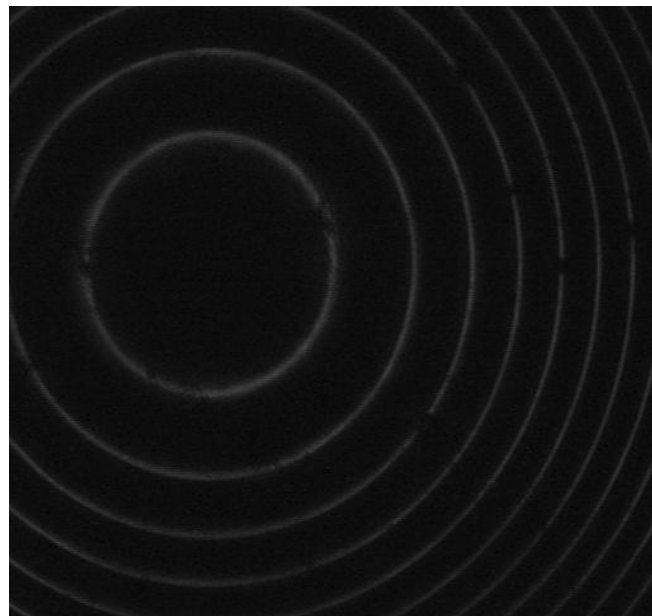


Fig.4.18: (A) Interferogram of the SLM OPO at 560 nm obtained with 4.5 GHz FP Interferometer.
(B) Interferogram of the frequency stabilized He:Ne obtained with 4.5 GHz FP Interferometer.

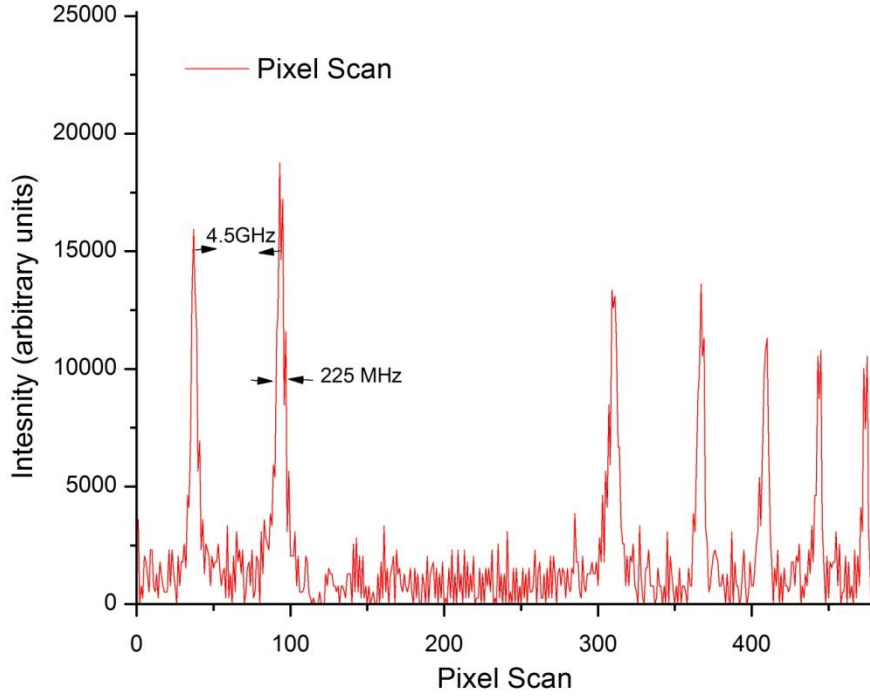


Fig.4.19: Intensity plot of the pixel scan of Interferogram (A), SLM OPO output at 560 nm.

The spectral linewidth of the SLM output can be estimated from the FP interferogram by using the standard expression [102] given by,

$$\Delta\nu = \frac{2D_1\Delta D_1}{D_2^2 - D_1^2} FSR \quad 4.8$$

where D_1 and D_2 are the diameter of the first and second fringes, respectively, and ΔD_1 represents the width (FWHM) of the first fringe. Using this technique the time-averaged spectral linewidth of SLM OPO output measured to be $\sim 225\text{MHz}$ at 550 nm operating at 1 kHz repetition rate. The same SLM OPO sampled output is used also to measure the spectral linewidth using Fizeau interferometer based wavelength meter (WS-U, High Finesse, Germany). The absolute wavelength measurement accuracy of this WS-U model is 30 MHz. This wavelength meter has an option to measure spectral linewidth with an accuracy of 100 MHz. The Fig.4.21 shows the spectral

measurement of SLM OPO operating at different wavelengths using this high-resolution wavelength meter.

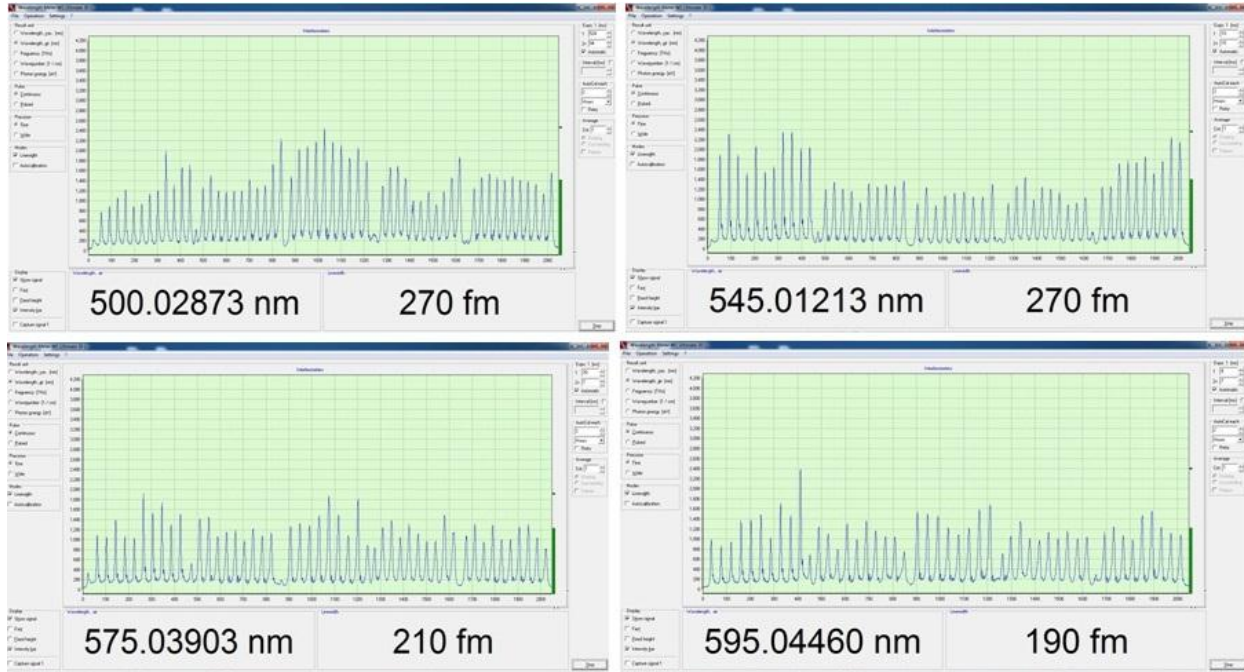


Fig.4.20: Spectral characteristics of SLM Type-II BBO OPO operating at different wavelengths.

4.4.3.2 Frequency stability of the SLM OPO

The SLM OPO operating at a wavelength of 564.78 nm, at 1 kHz repetition rate, without frequency stabilized feedback loop is monitored continuously using the high-resolution wavelength meter (WS-U). The frequency, as well as the corresponding spectral linewidth of the OPO, is continuously monitored for a duration of 1 hour. The Fig. 4.22 shows the long term stability of the SLM OPO wavelength and linewidth. The spectral linewidth of the SLM OPO measured using the high-resolution wavemeter is shown in the Fig. 4.23. During the long term operation, the wavelength of the SLM OPO varies from 564.78650 nm to 564.787381 nm with a

mean value of 564.7872695 nm at a standard deviation of 126 fm without mode hop. The spectral linewidth varies from 0.2 pm to 0.44 pm at a mean value of 0.298 pm with a standard deviation of 51.5 fm. The drift in the wavelength during the continuous operation is attributed mainly to the environmental temperature variation in the system.

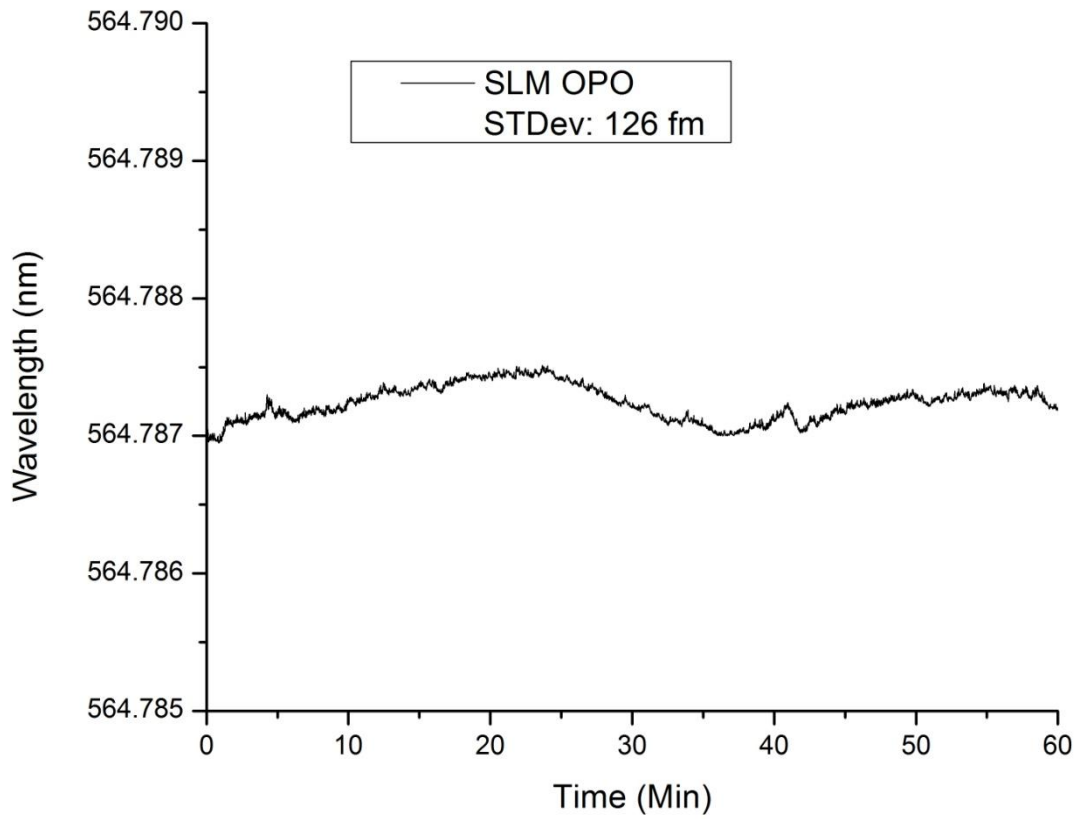


Fig.4.21: Inherent frequency stability of SLM OPO operating at a wavelength of 564.787 nm.

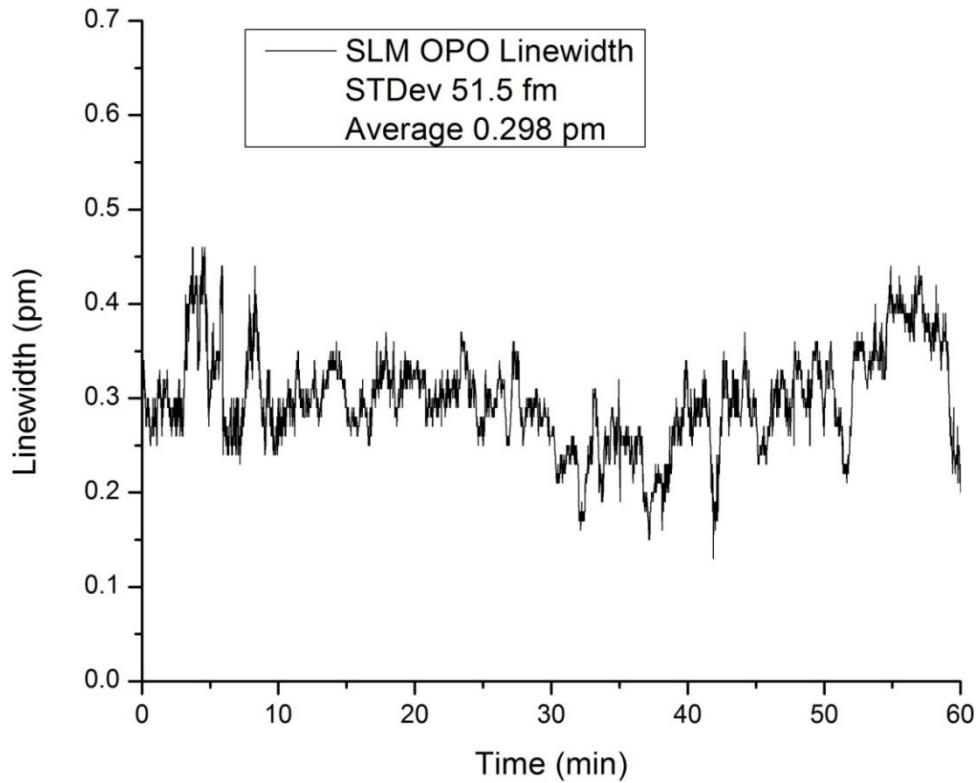


Fig.4.22: Variation of the spectral linewidth during the long-term operation of the SLM OPO operating at a wavelength of 564.787 nm.

In order to stabilize the frequency of the OPO system further, we have locked the wavelength using the PZT control feedback loop discussed in section 4.4.2. The Fig. 4.24 shows the long term stability of frequency stabilized OPO operating at a wavelength of 564.801 nm. The variation of the spectral linewidth of the OPO under locking condition is shown in the Fig. 4.25. During the continuous operation, up to 25 minutes, the SLM OPO is operated mainly at the desired wavelength (under lock condition). The wavelength change max: 564.80121 nm and min: 564.80101 nm with a mean value of 564.80109 nm at a standard deviation of 76.74 fm without mode hop. The Fig. 4.25 shows the comparison of frequency stability of the OPO under wavelength no lock and locking condition on equal grounds. In the case of under no lock condition,

the wavelength observed to drift towards the longer wavelength side from 564.786951 nm to 564.787504 nm with a standard deviation of 94.3 fm, whereas, in wavelength locking condition the OPO operates at a frequency of 564.8011 nm with frequency stability of 76.5 fm. However, the spectral linewidth of the SLM OPO under wavelength locking increases with time from 0.2 to 0.6 pm during this operation due to the fact that the etalon angle was not synchronously angle tuned corresponding to the change in the wavelength due to the forced change in the cavity length under wavelength lock condition. Hence, the linewidth of the SLM signal output increases slowly with the time leading to mode hopping after 25 minutes of operation which is shown in the Fig. 4.25. We are now improving the locking system by implementing the synchronized control tuning of the cavity length and etalon angle for mode hop free operation.

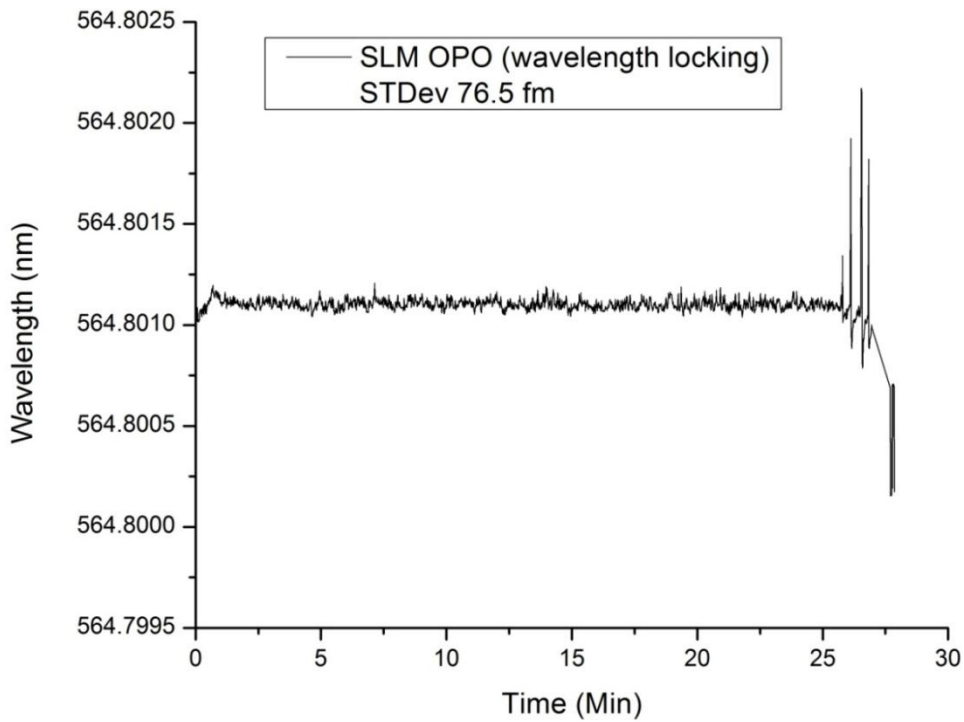


Fig.4.23: Frequency stability of SLM OPO with cavity stabilized feedback loop

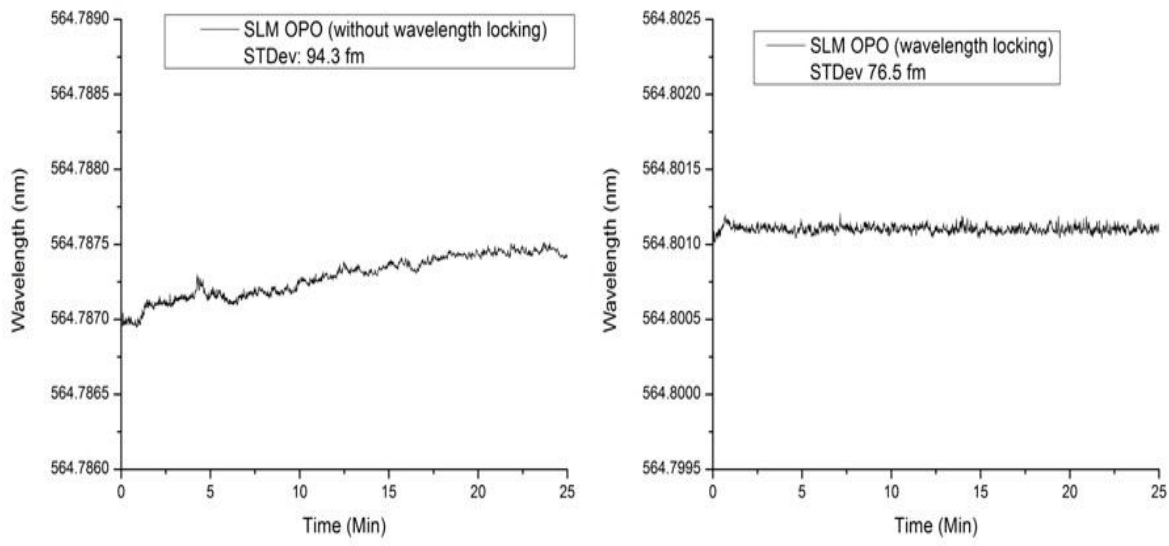


Fig.4.24: Comparison of the spectral linewidth of the SLM OPO under wavelength locking and without locking.

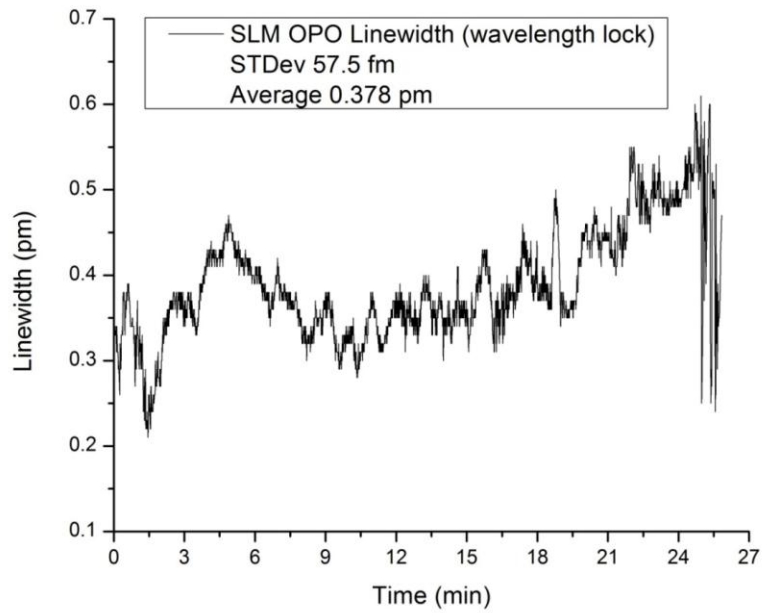


Fig.4.25: Variation of the spectral linewidth of the SLM OPO under wavelength locking.

4.4.3.3 Output Performance of the SLM OPO

The performance of the SLM Type-II BBO OPO has been characterized by studying the variation of the signal output power across its tuning range. The Fig. 4.26 shows the variation of measured signal output power when the SLM OPO signal output is tuned from 500 nm to 600 nm at a fixed pump power of 1.4 W. The reduction in the efficiency of OPO system during tuning output signal from 500 nm to 600 nm is due to decrease in the effective nonlinear coefficient of the Type-II phase-matched BBO crystal (as shown in Fig. 4.1) with the increase in signal wavelength and further due to higher reflection losses at the crystal surface. We have achieved a maximum output power of 62 mW with a conversion efficiency of 3.9 % at a repetition rate of 1 kHz at its peak wavelength 518.6 nm. At this operating condition, the pulse width of the SLM OPO measured to be 4.5 ns as shown in Fig. 4.27.

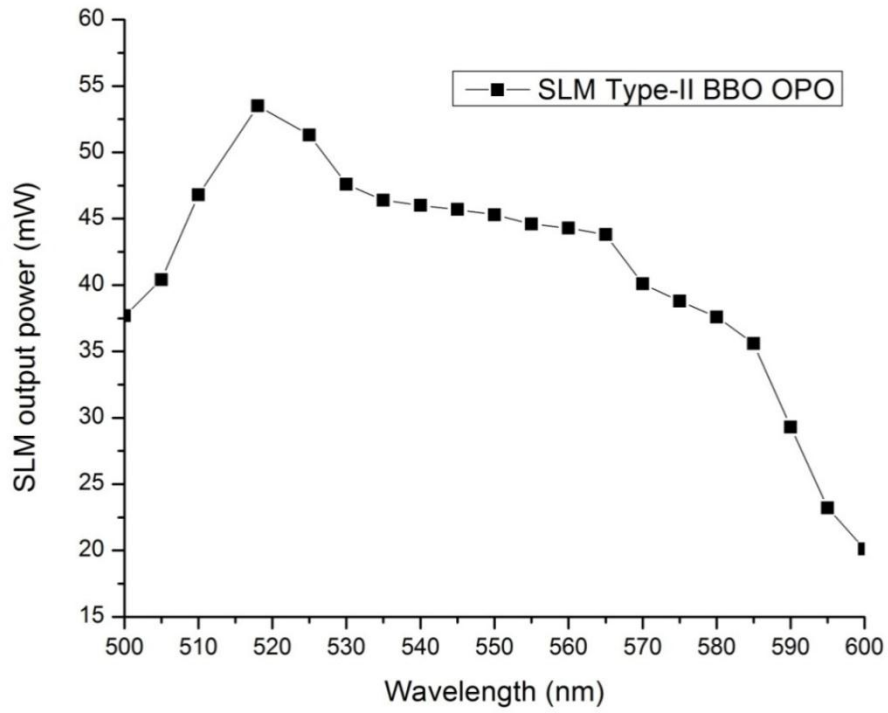


Fig.4.26: Variation of SLM OPO signal output power across its tuning range

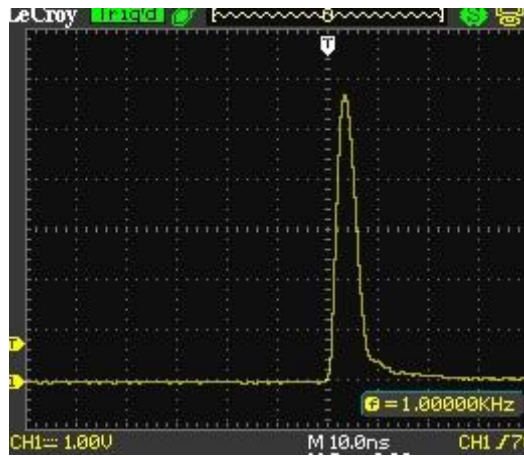


Fig.4.27: Temporal pulse shape of the SLM OPO operating at a wavelength of 518.6 nm at 1 kHz repetition rate.

4.4.3.4 Beam quality

The Fig.4.28 shows the near and far-field profiles and M^2 factor of the OPO signal measured at a signal wavelength of 560 nm at a repetition rate of 1 kHz. The M^2 factor at this signal wavelength is measured to be $M^2_x = 2.1$ and $M^2_y = 1.4$. The difference in the position of the beam in the x and y direction is due to astigmatism introduced by the cylindrical optics.

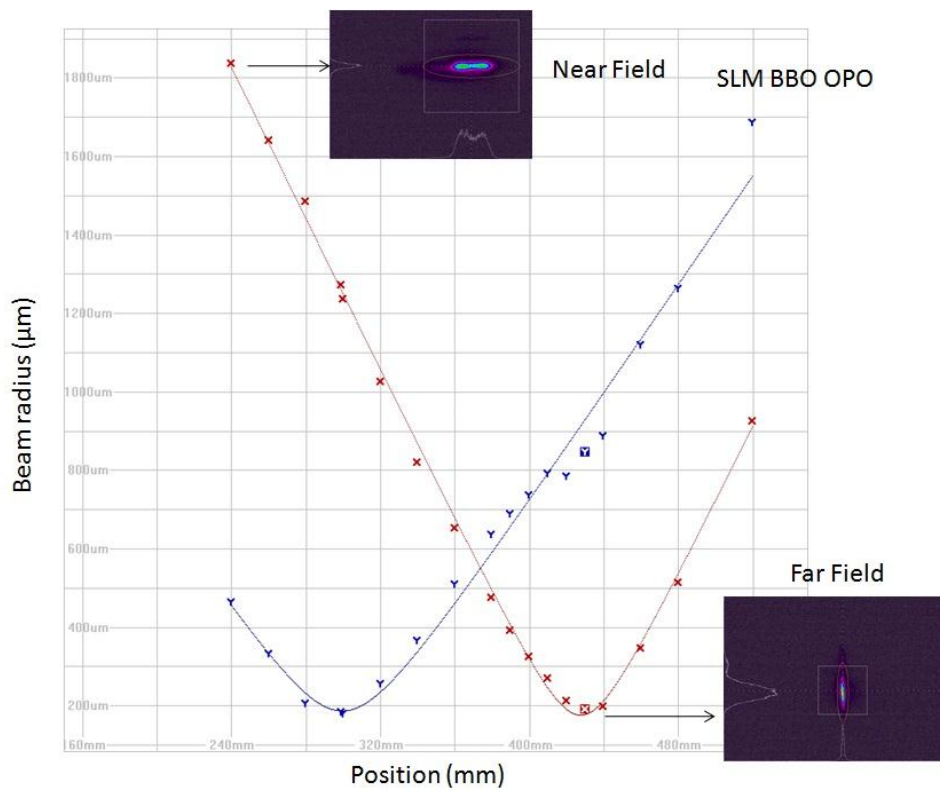


Fig.4.28: The measured M^2 factor, near and far field profiles of the SLM OPO signal beam at a wavelength of 560 nm at a repetition rate of 1 kHz.

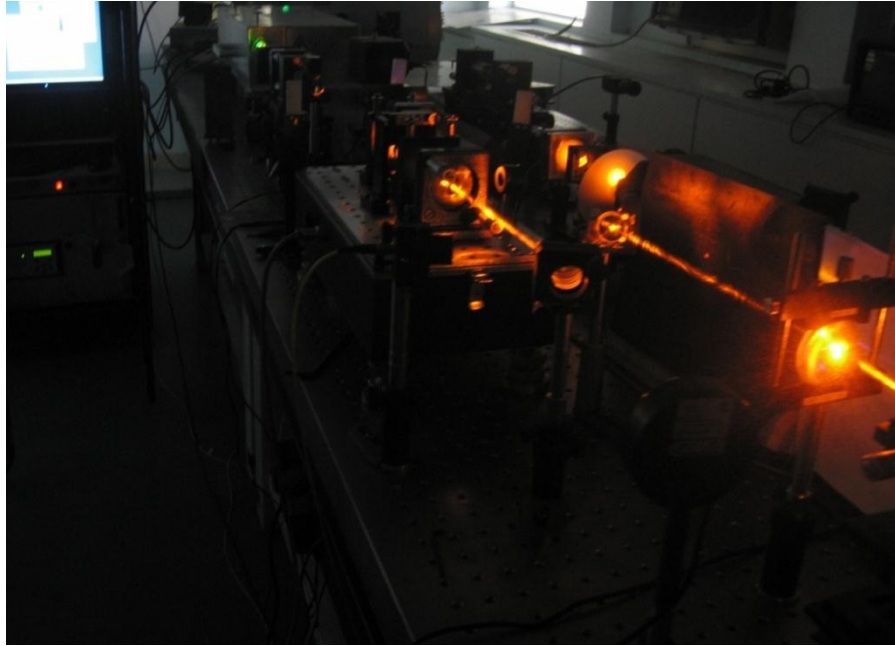


Fig.4.29: Photograph of the High repetition rate SLM OPO operating at a wavelength of ~ 590 nm at 1 kHz repetition rate.

4.5 Conclusion:

In conclusion, we have developed a high repetition rate (1-3 kHz), Type-II phase-matched BBO OPO pumped at 355 nm, which can be continuously tuned from 490 nm to 630 nm. The pump beam reflecting geometry is used for reducing the spectral bandwidth and oscillation threshold of the Type II BBO OPO that facilitated to use single intra-cavity FP etalon in the OPO cavity to demonstrate SLM operation in Type-II BBO OPO at 1 kHz. The spectral characteristics of the SLM OPO have been studied and the time-averaged spectral linewidth is measured to be ~ 225 MHz. The frequency stability of the SLM OPO with and without active cavity stabilization has been studied. We have summarized the tuning and spectral characteristics of the multi-kHz repetition rate OPOs developed in our lab in Table 4.1.

Table 4.1: Operating characteristics of high repetition rate OPOs developed at our lab.

OPO configuration	Repetition rate	Tuning wavelength	Spectral Linewidth
Type-I BBO OPO	1-5 kHz	490-630 nm	0.2-0.5 nm
Type-II BBO OPO	1-3 kHz	490-630 nm	~ 0.5 nm
Type-II BBO OPO pump double pass Configuration	1-2 kHz	490-630 nm	~ 0.15- 0.18 nm
SLM Type-II BBO OPO	1 kHz	500-600 nm	~ 225 MHz (0.225 pm)

Chapter 5

High average power operation of the OPO limited by thermal loading in BBO crystal

5.1 Introduction

Reliable and sustainable high repetition rate, high average power operation of the solid-state OPO over its tunable visible wavelength range will be useful for many basic and applied research. Presently, dye lasers in MOPA (master oscillator power amplifier) configuration have been providing a high repetition rate (typically 10's kHz), high average power tunable output in the visible spectral region for such applications. Therefore, it is evident that we extend our study toward increasing the high repetition rate operation of OPO. We have studied the effect of high average power operation on the performance of the nanosecond Type-II β -BaB₂O₄ (BBO) based optical parametric oscillators (OPO), pumped by the third harmonic (355 nm) of a Diode Pumped Solid State Laser (DPSSL) operating at repetition rate (3-5 kHz), and will be presented in this chapter. It is observed that the power and wavelength stability of the high average power optical parametric oscillators are affected by the thermal effects arising from the residual optical absorption in a nonlinear crystal. Thermal loading in the BBO crystal arising due to high repetition rate operation is studied by measuring the temperature distribution of the crystal for determining the average power scaling limit of visible nanosecond OPO's.

Thermal effects in optical parametric oscillators and amplifiers operating at low repetition rate (typically 10 to 100 Hz), low average power are usually negligible because of the fact that no

energy is stored in the parametric process and low residual crystal absorption at interacting waves in the nonlinear crystal does not result into the thermal load. However, at multi-kHz repetition rate, high average power operation of these OPOs the residual optical absorptions of pump, signal and idler waves in the nonlinear crystals, typically $\sim 0.1 \text{ m}^{-1}$ in the BBO, are large enough to be significant which gives rise to thermal gradients which can lead to thermo-optical distortions and disturb phase-matching condition. In addition, if the thermal effect is strong the thermal-induced stress in the nonlinear crystal may lead to optical damage of the crystal during its sustainable high average power operation [103]. The detrimental effects of thermal loading such as thermal lensing and bistability have been reported in OPOs [103,104]. In BBO crystal not only linear absorption, the two-photon absorption, as well as dynamic color center formation [105,106] are also the limitations for high average power operation, which lead to accumulated thermal effects.

This thermal effect leads to inhomogeneous heating of the nonlinear optical crystal that results in spatial temperature gradient and refractive index changes. The spatial inhomogeneous refractive index gradient leads to spatially varying phase-matching conditions, limiting the attainable average power, bandwidth and beam quality [107, 96]. If the thermal loading increases beyond the acceptable temperature bandwidth of the crystal, discussed in section 1.2.8 of chapter 1, then total optical interaction volume of the crystal will no longer satisfy the phase-matching condition resulting degradation of the parametric conversion efficiency. Therefore, in order to attain high conversion efficiencies as well as good spectral stabilities of these OPOs, the thermal gradients arising due to optical absorption must be much lower than the crystal acceptable temperature bandwidth.

Therefore, we have studied the effect of residual absorption of optical power at the pump (355 nm) and generated signal along with idler within the Type-II BBO crystal at 5 kHz repetition

rate of the pump laser beam and with typical pulse energies of 2-2.5mJ. The performance of the OPO has been evaluated by studying the variation of output signal power with input pump power at different repetition rates. The temperature gradient arising, mainly due to absorption of the high average power pump beam, has been measured by imaging the crystal using an infrared camera. This measurement facilitated us to ensure that the temperature gradient remained much lower than the acceptable temperature limit of the BBO crystal.

5.2 Measurement technique of thermal loading in BBO crystals

In our multi kHz repetition rate, Type-II BBO OPO, the performance of the OPO is found to degrade at high average power (8 W) of the pump beam, discussed in section 4.2.2 of chapter 4. As the average power of pump laser increases, the residual absorption of the pump beam in the BBO crystal increases. As a result, the crystal may have developed a temperature gradient which deteriorated the performance of the OPO. These temperature gradients in the crystal may have induced the change in phase matching conditions which causes the reduction in the gain of the signal output. These temperature gradients in the crystals depend on many factors such as crystal shape, size, thermal conductivity, and heat removal geometry and also crystal growth methods and fabrication conditions.

In order to measure the temperature profiles in both Type-II and Type-I BBO crystals arising due to the absorption of the pump laser (355 nm) beam, operating at different average power levels, we have developed an infrared camera (ThemaCAM Researcher, FLIRSC640) based temperature measurement setup. During measurement, this infrared thermo-camera is corrected for the emissivity of the BBO crystal ($\epsilon_{\text{BBO}} \sim 0.78$ [108]). The high-resolution camera acquires the real-time thermal image of the BBO crystal through its commercial software and performs the

thermal analysis of the image to give the temperature distributions at various desired locations and measures the maximum temperature of the crystal with an accuracy of 0.1⁰C. From the temperature measurements of the BBO crystals with increasing pump power, it is found that the pump beam absorption is the main source of heating and the absorption due to significantly lower power signal and idler waves are negligible. Therefore, a rise in crystal temperature measurements is carried out in presences of high repetition rate pump beam only. Different BBO crystals used in our OPO set-up are wrapped with a 100 μm thick indium foil to ensure good thermal contact over the whole crystal length and mounted in a copper holder for efficient heat removal. In our OPO setups discussed in earlier chapters, the crystals are not provided with any cooling, except air cooling at room temperature (~22⁰ C). Therefore, during OPO operation the crystals transferred the generated heat to the surrounding environment through conduction and convection processes. For a set pump power, the peak temperature of the crystal is measured when the temperature of the crystal reached a steady-state value. The thermal conductivity and thermo-mechanical properties of the BBO crystals are reported in the ref [72, 109]. Some of the important thermal properties of the BBO crystal are listed in Table.5.1. The Fig.5.1 shows the infrared camera image of the crystal with temperature distribution in the transverse direction to the propagation of the pump beam. In the Fig.5.1, the rectangular illuminated area shows the crystal which is mounted in the copper holder (the black region around the crystal). The Point A represents the location of the localized heat zone where high average power pump laser has been striking the crystal surface. The point B represents the lesser heat zone which is obviously the crystal boundary. The radial temperature change, ΔT (r) given by $\Delta T(r) = T_{\max} - T(r)$ causes the thermal dephasing, that results in the spatially varying phase-matching condition. The peak temperature of the BBO crystal is measured to be 45⁰C when the pump laser is operated at a repetition rate of 5 kHz with 2.25 mJ pulse energy. The Fig.5.2

shows the evolution of the measured temperature with time at the locations A and B of the crystal which is shown in the Fig. 5.1

Table 5.1: Some important physical and thermal properties of BBO crystal [59]

Crystal	Density (Kg/m ³)	Specific Heat (J/Kg-K)	Thermal Conductivity (10 ⁻⁶ /K) (, ⊥ optics axis)	Thermal Expansion (10 ⁻⁶ /K) (, ⊥ optics axis)
BBO	3840	490	1.6, 1.2	36, 4

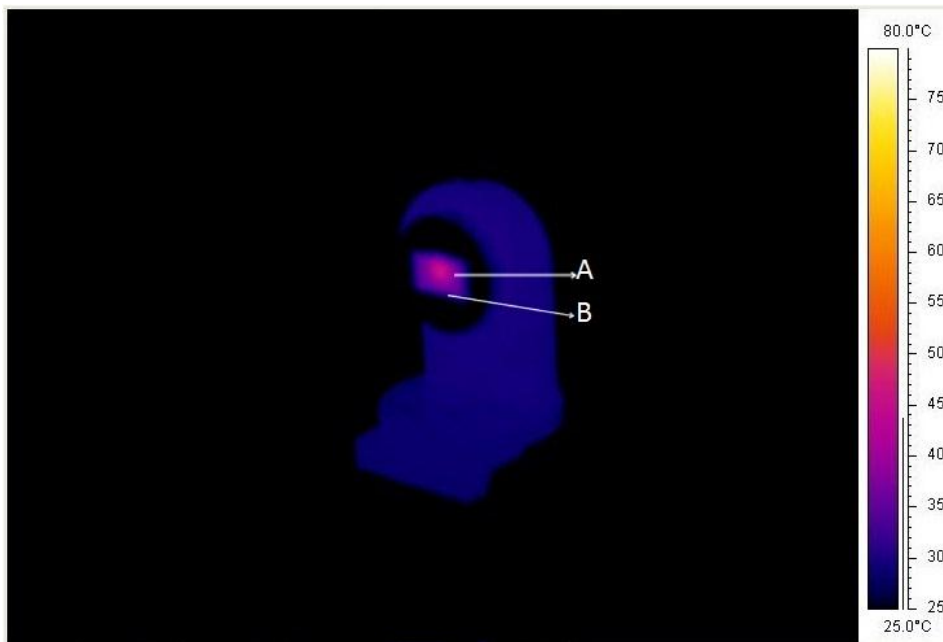


Fig.5.1: Infrared camera image of the crystal acquired when a high repetition rate (5 kHz) pump laser is propagated through the BBO crystal.

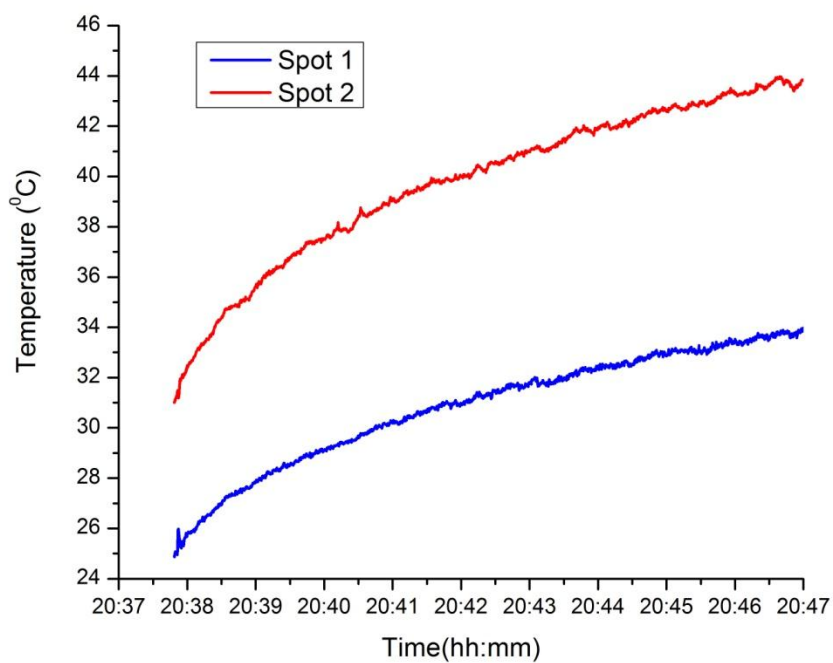


Fig.5.2: The temperature rise of the crystal with time at locations A and B

5.3 Effect of high average power operation on the performance of Type-II BBO OPO

5.3.1 The effect of thermal loading in Type-II BBO OPO

The Type-II phase-matched BBO crystal based OPO, which is setup for achieving high repetition rate narrowband operation, has been discussed in detail in chapter 4, section 4.2.1. The reason for choosing the Type-II phase-matched BBO crystal for narrowband operation is that the

Type-II phase matching exhibit much narrower spectral linewidths compared to Type-I phase matching. Conversely, the Type-II OPOs exhibit lower optical conversion efficiency because of smaller nonlinear coefficient values compared to Type-I shown in the Fig.4.1 of chapter 4. Hence it is necessary to use these type-II BBO crystals in longer and larger aperture sizes for efficient operation. The disadvantage of using the BBO crystal in longer size is that it increases the walk off angle and also decreases the acceptance angle, the acceptance bandwidth, and the acceptance temperature bandwidth. The decrease in acceptance angle and acceptance bandwidth impose more stringent constraints on pump laser for good beam quality as well as high spectral purity. Whereas, a decrease in acceptance temperature bandwidth of the crystal restricts the high average power operation of OPOs. The acceptable temperature bandwidth depends on the length of the crystal, as discussed in section 1.2.8 of chapter 1.

The FWHM temperature acceptance bandwidth of a crystal of length l is given by,

$$l\Delta T = \frac{1}{\left[\frac{1}{\lambda_s} \frac{dn_s^o}{dT} - \frac{1}{\lambda_i} \frac{dn_i^e}{dT} - \frac{1}{\lambda_p} \frac{dn_p^e}{dT}\right]} \quad 5.1$$

Where, $dn^o/dT = -16.6 \times 10^{-6} \text{ K}^{-1}$ and $dn^e/dT = -9.3 \times 10^{-6} \text{ K}^{-1}$ (λ varies from 400-1000 nm).

Using the equation (5.1) the acceptance bandwidth of the Type-II BBO crystal for 20 mm length at a signal wavelength is calculated to be $\sim 8.33\text{K}$ and for Type-I BBO crystal with crystal length of 15 mm is 11.16 K. Hence for efficient operation of the OPOs using the Type-II BBO crystal with a length of 20 mm, the temperature gradients arising due to high average power operation must be less than the acceptable temperature bandwidth of 8.33K. The change in the phase-matching angle with the corresponding increase in the temperature for the signal wavelength at 560 nm of Type-II BBO OPO is calculated to be $\sim 4.6 \mu\text{rad}/^\circ\text{C}$.

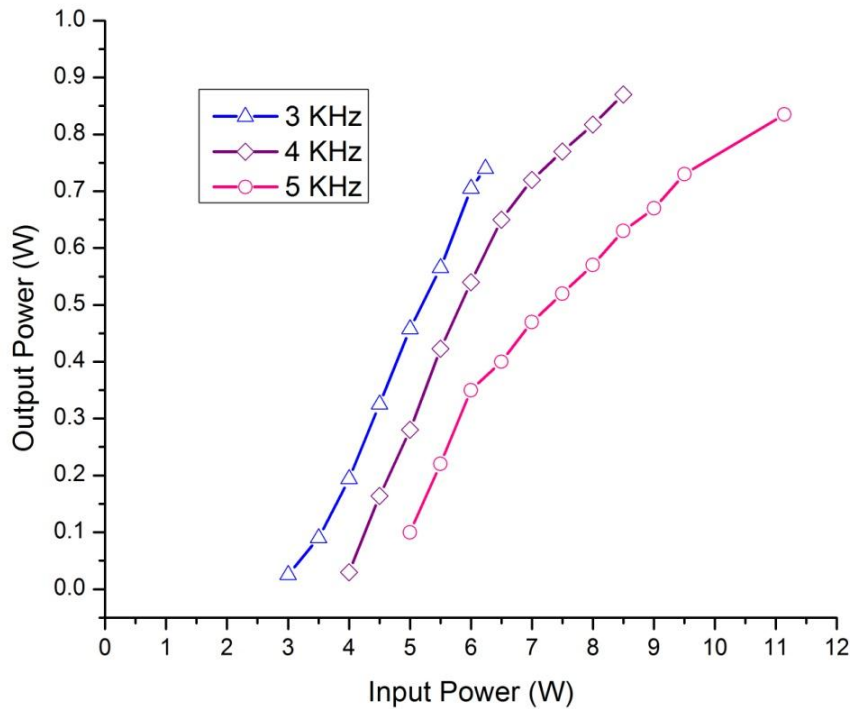


Fig.5.3: Output performance of the Type-II BBO OPO at high average powers of the input pump laser.

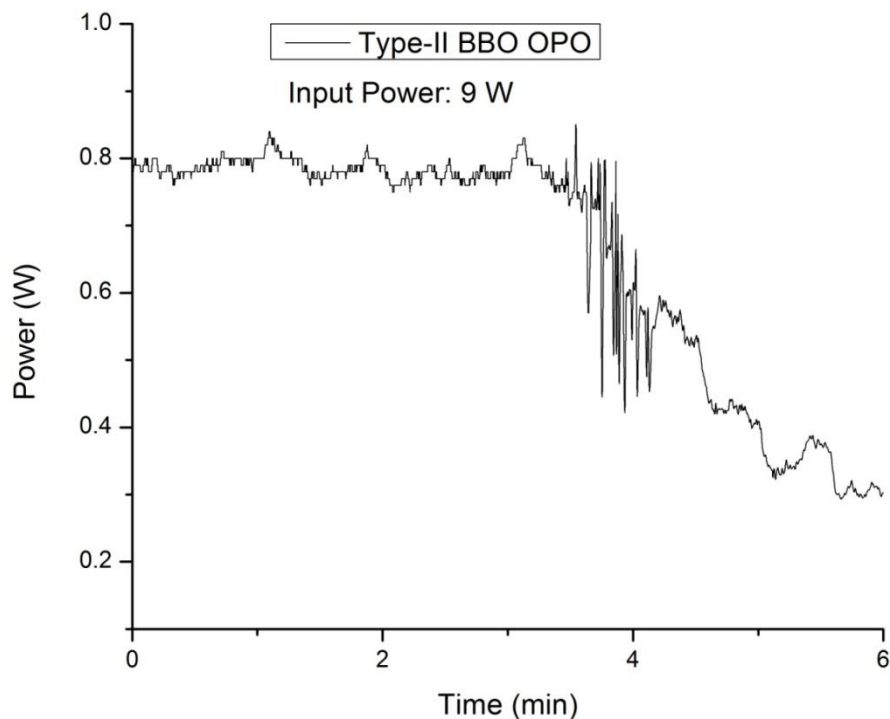


Fig.5.4: The longterm power stability of the Type-II BBO OPO at an input power of 9W at 4 kHz repetition rate

The Fig. 5.3 shows the performance of the Type-II BBO OPO above 3 kHz repetition rate. From the plots in the figure, it is clear that at a lower repetition rate of the pump laser the OPO output rises linearly with an increase in pump power, as predicted by the theory. However, at a higher repetition rate of the pump laser with average power beyond ~ 8 W, the performance of the Type-II BBO crystal OPO starts to degrade. The long-term power stability of the Type-II BBO OPO at an input pump power of 9 W @ 4 kHz repetition rate is shown in the Fig. 5.4. From this plot, it is evident that the output power of the signal wave starts to degrade after 4 minutes of operation. To investigate the reasons for the degradation of the performance of the OPO at high repetition rates of the pump laser, the absorption in the BBO crystal has been determined by

performing transmission measurements to estimate the overall losses due to linear and two-photon Absorption (TPA). The Fig. 5.5 shows the transmission loss of the pump laser power through the Type-II BBO crystal at different repetition rates at a fixed pump pulse energy of 2.25 mJ.

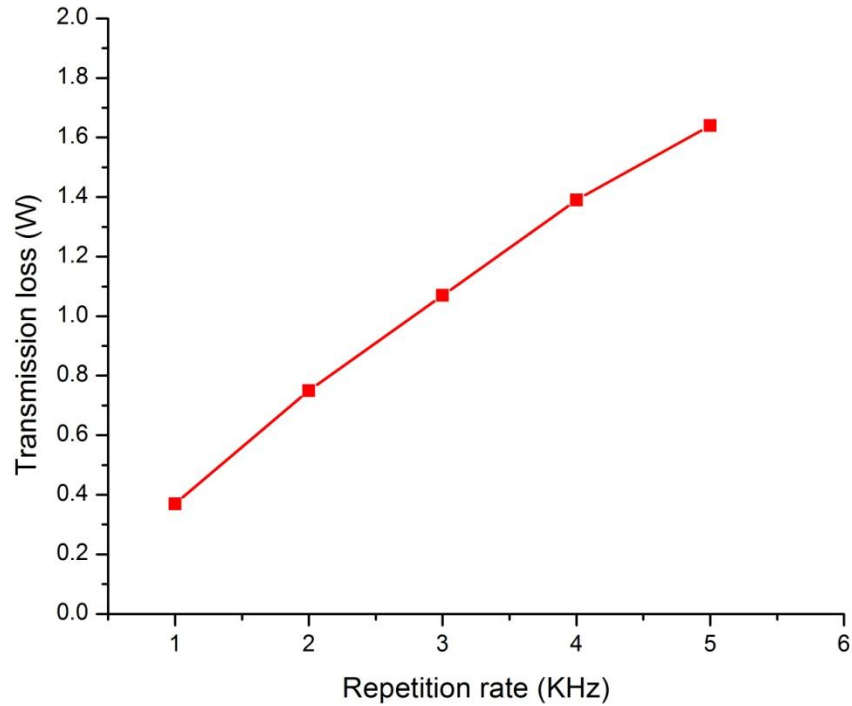


Fig.5.5: Propagation transmission loss of the pump laser beam in the Type-II BBO crystal operating at different repetition rates with a pulse energy of 2.25 mJ.

The transmission loss of the pump laser beam propagating inside Type-II BBO crystal is measured to increase with an increase in the repetition rate. We have observed a substantial reduction in the transmitted power of the pump laser at a repetition rate of 5 kHz. Typically, a maximum power loss of 1.7 W was obtained at an input pump power of 11.25 W. Obviously, the absorbed pump power in the crystal develops thermal loading in the crystal which in turns increases the localized temperature of the crystal. The peak temperatures of the crystal at different

average powers of the crystal has been measured to estimate the average power scaling limit of the Type-II BBO OPO, which is discussed in the next section of the thesis.

5.3.2 Average power scaling limits of Type-II BBO OPO

In order to estimate the thermal loading and temperature gradients inside the Type-II BBO crystal, we have measured the steady-state peak temperature of the crystal and temperature distributions using the infrared camera, as discussed in section 5.2 of this chapter. The Fig. 5.6 shows the variation of the signal output power and the corresponding measured peak temperatures of the crystal at different repetition rates of the pump laser operating at a set pulse energy of 2.25 mJ.

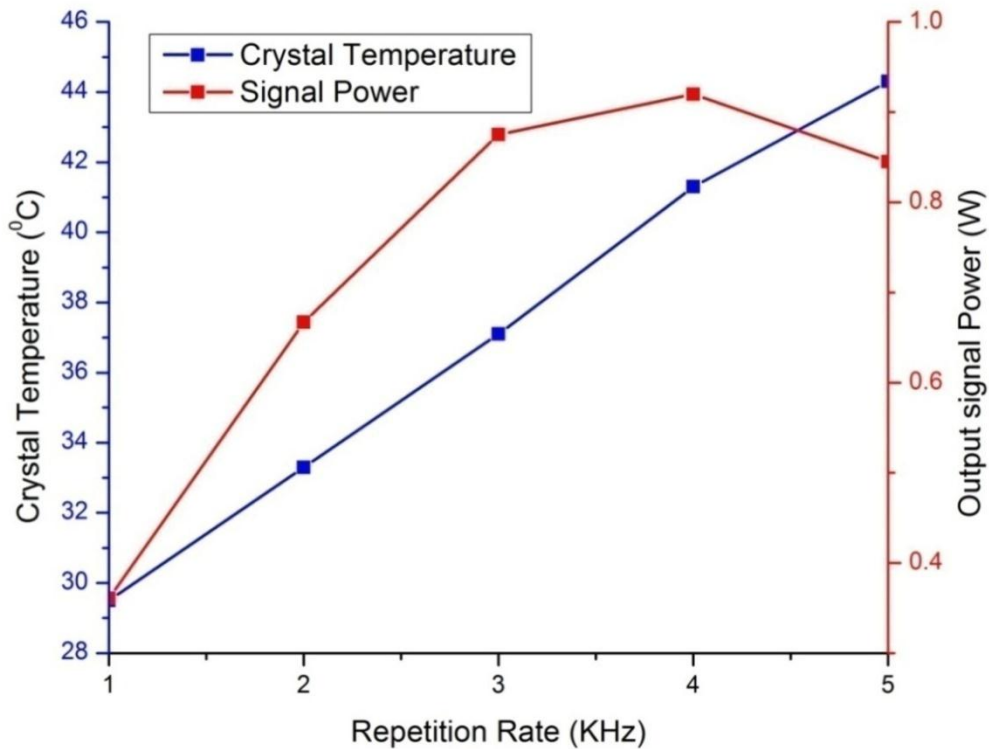


Fig.5.6: Variation of the output signal power and temperatures of the crystal when the pump laser operating at different repetition rates with pulse energy of 2.25 mJ.

It is observed that the pump laser operating above 8 W of average power, the temperature gradient of Type-II BBO crystal exceeded its acceptable temperature bandwidth. Consequently, the output performance, such as pulse to pulse stability of the Type-II BBO OPO degrades.

The Fig. 5.7 illustrates the comparison of measured peak temperatures at the crystal input surface of both Type-I and Type-II BBO crystals as a function of the repetition rate of the pump laser (room Temperature $\sim 26^{\circ}\text{C}$) with a set pump pulse energy 2.25 mJ. From our temperature measurements, it is apparent that the Type-II BBO crystal exhibits a much slower rate of heat transfer because of their bigger size and volume in comparison to the Type-I BBO crystal. Hence, the temperature gradient in Type-II BBO crystal is higher compared to Type-I BBO crystal, in otherwise similar OPO operation conditions. Thus, Type-I BBO crystal with dimensions similar to our optimized crystal size (length 15 mm) is suitable for achieving high average power operation under pump repetition rate of 5 kHz at a pulse energy of around 2 mJ. Furthermore, for high average power narrowband operation, instead of using longer size Type-II BBO crystal, the possibility of using highly efficient Type-I BBO crystal integrated with other narrowband techniques such as injection seeding [34] and Grazing Incidence OPO (GIOPO) [110] configuration can be exploited.

Since the temperature gradients are observed to approach the temperature bandwidth tolerance limits, they may induce optical stress inside the crystal hindering long term operation of such high repetition rate OPO's [111]. The temperature gradients must be minimized for damage-free long term OPO operation of these crystals. Heat management schemes such as cooling the side surfaces of the crystals for dissipating the heat more effectively; minimizing the heat accessions such as coatings of the crystals may be adopted. Recent approach of sandwiching the

crystal front and rear surfaces with a transparent and high thermal conductivity material like sapphire plate [112, 108], which has forty times larger thermal conductivity than BBO crystals, are proposed to implement with improved designs of reduced thermal effects for future development of high average power narrowband visible OPO's.

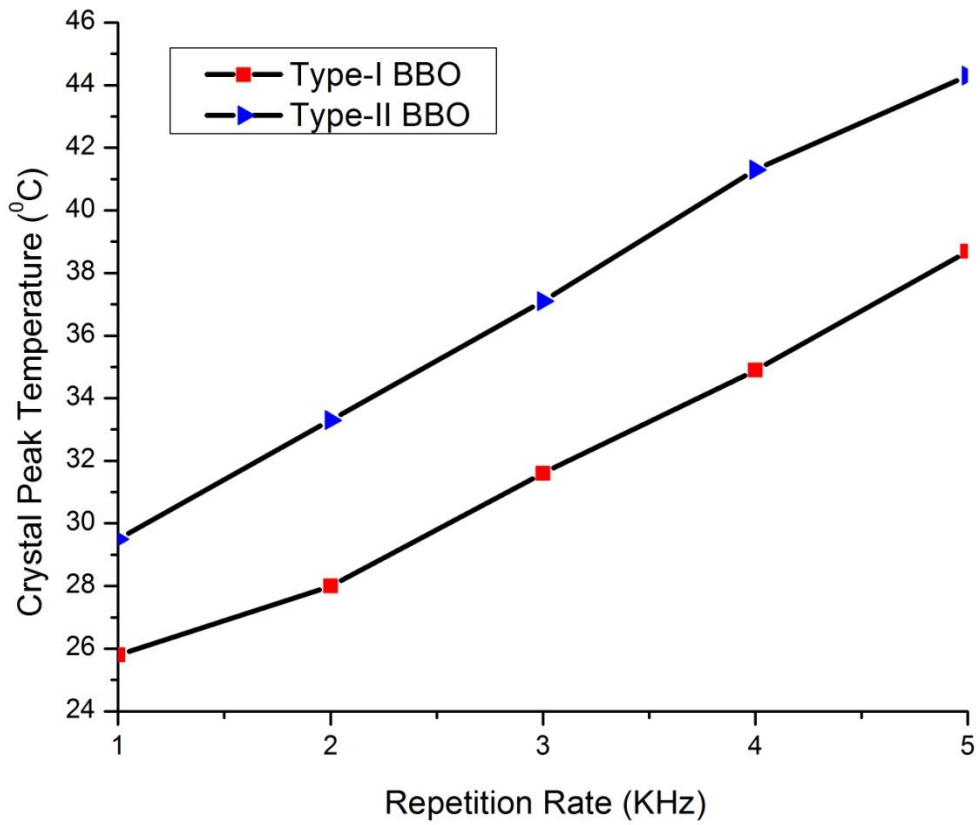


Fig.5.7: Comparison of measured peak temperatures of Type-I and Type-II BBO crystals at different repetition rates of pump laser for set pump pulse energy of 2.5 mJ.

5.4 Conclusion:

In conclusion, we have developed a technique for measuring the thermal loading arising due to the absorption of the pump laser inside the BBO crystals. We have studied the effect of pump beam absorption on the performance of a Type-II β -BaB₂O₄ (BBO) operating at different average powers. The performance of this OPO is observed to degrade when the pump laser is operated beyond 3 kHz repetition rate with a pulse energy of 2.25 mJ, owing to the thermal effects arising due to the residual absorption of the pump beam. In order to explain the degraded performance of the Type-II BBO OPO at higher repetition rates, we have measured the increase in the temperatures of the BBO crystal as a function of the pump lasers and discussed the influence of thermal effect on the performance of high average power OPO's.

Chapter 6

Application of narrowband OPO for measuring attenuation coefficient of seawater samples in the visible spectral region for underwater communications

This chapter of the thesis describes the application of the constructed multi-kHz repetition rate, nanosecond, narrowband OPO which offers continuous wavelength tunability in the entire visible spectral region. Among many applications of this high average power OPO, we have used it for a need based measurement of wavelength dependent optical attenuation coefficient of seawater samples. We have developed an appropriate laboratory experimental set up for deriving the optical attenuation coefficient of various water samples including seawater by utilizing the constructed widely tunable (450-650 nm), high repetition rate (2 kHz), narrowband OPO for the use of these data in underwater communication. The variation of the attenuation coefficient of seawater samples as a function of wavelength illustrates the maximum transmission window of the seawater in the visible region.

6.1 Introduction

Laser based underwater communication is capable of providing high bandwidths communication compared to the existing acoustic and RF techniques [113-120]. They are being projected to be useful for strategic and scientific applications involving high bandwidth image and data transfer at a faster rate [121, 122] in the ocean underwater. High-speed optical communication system using a single laser diode with a transmission rate of 2.7 Gbit/s has been demonstrated with a propagation distance of 34.5 m [123]. However, the performance of these underwater communication systems is very much dependent on the propagation characteristics of the laser beam in the seawater. The laser beam suffers severe attenuation due to absorption and scattering of the laser photons because of the interactions with the water molecules and other particulate matters in water. As a consequence, underwater optical links inside the seawater are limited to much shorter ranges when compared with other techniques. In an underwater environment, matters such as chlorophyll are capable of absorbing the blue and red lights. These matters and other colored dissolved organic materials (CDOM) can increase the turbidity of the water, and thus minimize the propagation distance of the laser beam. The communication link range varies from a few meters in more turbid harbor water to approximately 100 m in clear blue ocean water. The optimum wavelength of the laser source in an underwater optical link depends on the inherent optical properties of the seawater which varies widely between geographic locations. In coastal and harbor water, closer to land, the concentration of particulate matter such as organic and inorganic is much higher, and as a result, the wavelength of minimal attenuation is shifted from blue to green wavelengths.

Hence, for designing the laser based underwater communication systems it is important to generate the wavelength dependent optical attenuation coefficient data of the seawater samples

taken at different geographic locations. These data will provide the optimum wavelength of a particular seawater sample at which the laser beam propagates to a maximum distance. In this chapter, we describe the measurement of the optical attenuation coefficient of seawater samples using recently developed high average power, nanosecond OPO system which is capable of generating the tunable radiation continuously from 450 nm to 650 nm. Using our experimental setup, we have determined and illustrated the variation of the optical attenuation coefficient of various water samples across the OPO tuning wavelength.

6.2 OPO based seawater optical attenuation coefficient measurement technique

The schematic of the OPO based optical attenuation coefficient measurement setup is shown in Fig.6.1. The OPO in this experiment is a Type-II BBO crystal based OPO in double-pass configuration [81]. The details of the OPO design and its performance was discussed in section 4.3.2 of the thesis chapter 4. Even though, the OPO cavity mirrors are broadband dielectric coated in the wavelength region of 450-650 nm (Fig. 3.2), we have claimed the tuning range of these developed OPOs are limited to only 490-630 nm is mainly due to the decrease in the % of the transmission in the wavelength region of 450-480 (output coupler) and 450-460 nm (input mirror). However, the extended tuning range of the OPO in the wavelength range of 450-490 nm and 630-650 nm had observed and utilized for measuring the attenuation coefficient of seawater samples in the wavelength region of 450-650 nm. The spectral linewidth of the generated signal beam is found to vary from 0.15 nm to 0.19 nm across its tuning range. The operating characteristics of the OPO are given in the Table. 6.1. The output signal beam is routed to a power meter and a wavelength meter using the mirrors M6 and M7 for measuring the input power and wavelength.

Table 6.1: Operating characteristics of Type-II BBO OPO.

OPO	Output characteristic
Tuning Range	450-650 nm
Power	300 mW
Spectral Linewidth	0.15-0.19 nm
Pulse width	6 ns
Repetition rate	2 KHz
Beam divergence	~ 3 mrad

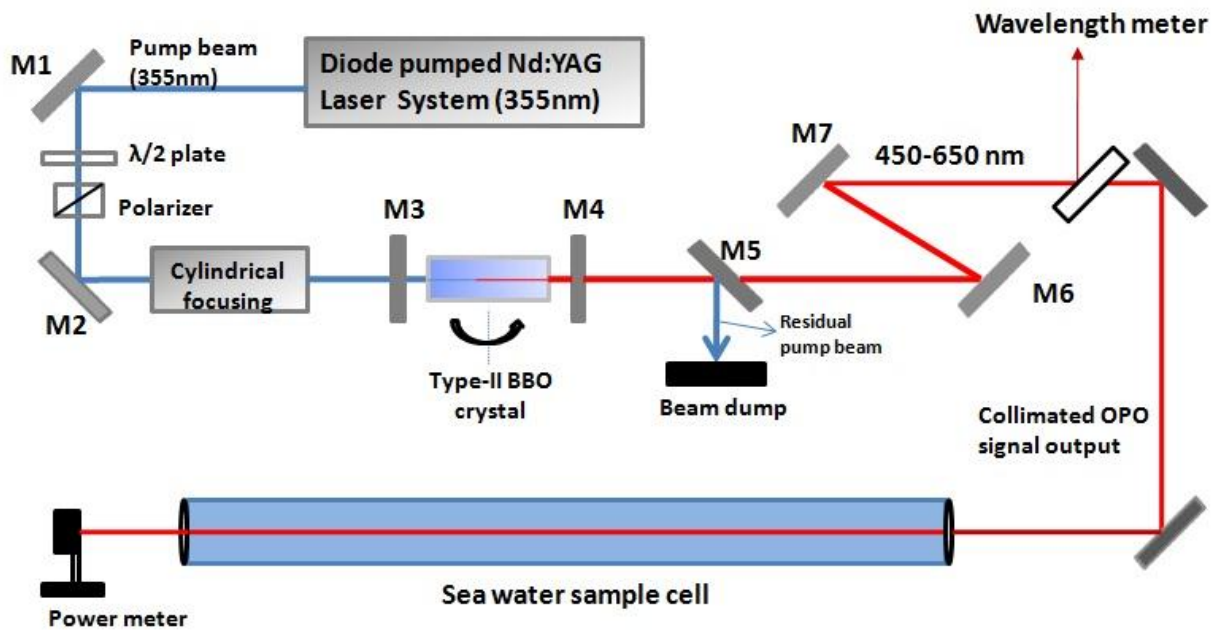


Fig.6.1: Schematic of the OPO based optical attenuation coefficient measurement technique.

Both the mirrors M6 and M7 have high reflectivity at the OPO signal wavelength and high transmission for pump and idler wavelengths so as to restrict the pump and the idler from reaching

the power and wavelength measurement systems. A uniform irradiance profile of the OPO signal beam is achieved by using two circular apertures to allow only the central portion of the signal beam to propagate through the water sample cell. The divergence of the signal beam is measured to be ~ 3 mrad. Using the routing mirrors as shown in the Fig.6.1, the OPO signal beam is made to propagate through the water sample cell which is having a length of 2 m. The ratio of the OPO signal beam powers, before and after transmission through the sample cell, is measured and compared with the ratio of the powers measured for the empty cell to determine the optical attenuation coefficient of the water samples.

6.3 Experimental Results

6.3.1 Comparison of the optical attenuation coefficient of various water samples

The loss of the OPO signal power propagating through the water sample cell is due to the combined effect of absorption and scattering of the optical beam. The overall attenuation of the laser beam during its propagation through water can be expressed as a beam extinction coefficient, c which is the linear combination of absorption coefficient $a(\lambda)$ and scattering coefficient $b(\lambda)$ given as, $C(\lambda) = a(\lambda) + b(\lambda)$. The propagation loss factor, L_p as a function of wavelength and the propagation distance, z is then given as, $L_p(\lambda, z) = \exp(-C(\lambda)z)$.

Using the above experimental setup with tunable OPO, the attenuation coefficient of seawater samples, collected from the coastal area of Arabian sea near BARC, Trombay and different test water samples such as de-ionized water, municipal tap water, de-ionized water dissolved with salt (salinity of $\sim 3.5\%$) are measured for different wavelengths of the OPO signal

output. Fig.6.2 shows the variation of attenuation coefficient with a wavelength of different water samples including the seawater sample.

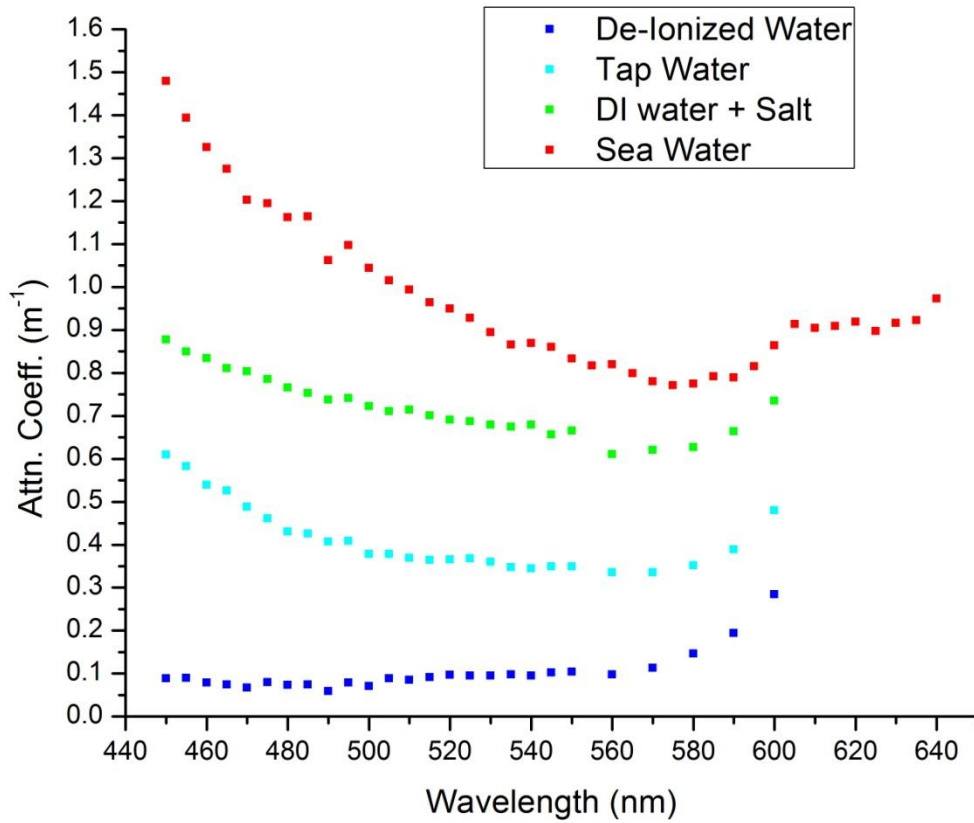


Fig.6.2: Comparison of measured optical attenuation coefficient of different water samples as a function of visible wavelengths.

6.3.2 Determination of laser transmission window of seawater samples

The Table.6.2 summarizes the measured transmission wavelength window of different water samples. The attenuation coefficient of Arabian Sea water sample collected from the coastal area of BARC, Trombay is observed to be low at a wavelength of ~580 nm. Thus we have demonstrated sensitivity and simplicity of our developed multi-kHz repetition rate OPO set up for measuring the optical attenuation coefficient of various water samples with high accuracy to determine the transmission window for choosing the precise laser wavelength to propagate the laser beam for longer distances in the sea.

Table 6.2: Measured laser transmission window of various water samples

S.No.	Water Type	Attenuation coefficient (m^{-1})	Transmission window
1.	Seawater (Turbid harbor sample)	0.76-0.78	550-600 nm
2.	DI water + salt	0.6-0.65	540-590 nm
3.	Tap Water	0.3-0.4	480-590 nm
4.	DI water	0.05-0.1	450-550 nm

6.4 Conclusions:

In conclusion, we have developed a tunable (visible range) OPO based optical attenuation coefficient measurement technique which is used for measuring the optical attenuation coefficient of seawater samples, collected from different geographic locations. These data are useful in determining the transmission wavelength window of seawater for designing the underwater optical communications system.

Summary

The major objectives of the present investigation are to develop a widely tunable, high repetition rate, narrowband, 355 nm pumped nanosecond OPOs, for the first time, which are highly desirable for various spectroscopic applications in departmental programs. These OPOs have been developed with an intention to replace existing ubiquitous dye laser oscillators, presently serving as high average power narrowband tunable sources of laser. The dye laser oscillators are limited by the wavelength tunability, safety and complexity issues related to handling and disposal of such hazardous and toxic dye solutions. To this end, various design configurations of the OPOs have been explored by using different types of phase-matched BBO crystals with different sizes and characterized their performances to determine the optimum design configuration of the OPO for achieving high repetition rate narrowband operation of the OPOs. Thermal loading arising due to high average power operation of these OPOs have been investigated to determine the ultimate power scalability of these devices. The achievements are highlighted below.

1. The optimum elliptical focusing parameters of the high repetition rate (5 kHz) input UV (355 nm) pump beam have been evaluated numerically for achieving reliable low threshold operation of a singly resonant nanosecond β -BaB₂O₄ (BBO) based optical parametric oscillator.
2. Designed and developed broadband, high repetition rate (5 kHz), nanosecond, Type-I phase-matched β -BaB₂O₄ (BBO) crystal based optical parametric oscillator (OPO), pumped by the third harmonic (355 nm) of a Diode Pumped Solid State Laser (DPSSL), for the first time. This OPO can be continuously tuned from 490 nm to 630 nm. The performance of the OPO has been characterized for the performance and spectral linewidth at 5 kHz repetition rate.

3. Designed and developed a spectral linewidth reduction technique in Type-II BBO OPO that facilitated to use single intra-cavity FP etalon in the OPO cavity to demonstrate SLM operation in Type-II BBO OPO at 1 kHz. The time-averaged spectral linewidth of the developed SLM OPO is measured to be ~ 250 MHz across its tuning range. The performance of the SLM OPO has been characterized for its performance and frequency stability.
4. We have investigated that the residual absorption of the pump beam due to high average power operation beyond 3 kHz repetition rate with a pulse energy of 2.25 mJ in 20 mm long Type-II β -BaB₂O₄ crystal OPO increases thermal loading to above its acceptable temperature limits of the crystal. As a result, these temperature gradients of the crystal have induced the change in phase matching conditions which causes the reduction in the gain of the signal output.
5. We have utilized our in-house developed high repetition rate widely tunable (spectral region of 450-650 nm) narrowband OPO for measuring the optical attenuation coefficient of seawater samples, collected from different geographic locations. These data are useful in determining the laser transmission wavelength window of seawater for designing the underwater optical communications system.

All solid-state, high repetition rate, high monochromaticity (SLM) and broad wavelength tunability (500-600 nm) are the key features of the developed OPO device. The laser sources with these features are highly desirable for applications in DAE especially in multistep laser photoionization spectroscopy of actinides to determine the number of important physical properties of heavy atoms with complex spectra including ionization potentials, energy levels, and lifetimes of levels, branching ratios, isotope shifts, and hyperfine structure. In addition, these sources are essential for achieving high signal to noise ratios in the elemental/isotope trace detection of actinides.

References:

1. T. H. Maiman, *Nature* 187, 493 (1960)
2. F. J. Durate (Ed.), *High power dye lasers*, Springer-Verlag, Berlin, 1992
3. W. Demtröder, *Laser Spectroscopy*, 3rd Ed. (Springer, 2003).
4. F. P. Schäfer and K. H. Drexhage, *Dye Lasers*, 2nd rev. ed., vol. 1, Berlin; New York: Springer-Verlag, 1977.
5. F. J. Durate (Ed.), *Tunable lasers handbook*, Academic Press, Inc., 1995
6. P. F. Moulton, "Spectroscopic and laser characteristics of Ti:Al₂O₃", *J. Opt. Soc. Am. B* 3 (1), 125 (1986)
7. W. Koechner (Ed.), *Solid-state laser engineering*, Springer-Verlag, Berlin, 1996
8. R. L. Byer, *Optical Parametric Oscillators*, In *Treatise in Quantum Electronics* (Academic Press, New York 1973) pp. 587-702
9. M. Ebrahimzadeh, *Optical Parametric Devices*, in *Handbook of Laser Technology and Applications*, PP 1347-1392.
10. B. J. Orr, J.G.Y. He, R.T. White, Spectroscopic applications of pulsed tunable optical parametric oscillators, in *Tunable Laser Applications*, Chap, 2, 3rd edn, ed. by F.J. Duarte (CRC Press, New York, 2016), pp. 18–106.
11. P. A. Franken, A. E. Hill, C.W. Peters, and G. Weinrich, "Generation of optical harmonics," *Phys. Rev. Lett.*, vol. 7, pp. 118–119, Aug. 1961.
12. D. A. Kleinman, "Nonlinear dielectric polarization in optical media," *Phys Rev.*, vol. 126, 1977(1962).

13. P. D. Maker, R.W. Terhune, M. Nisenhoff, and C. M. Savage, "Effects of dispersion and focusing on the production of optical harmonics," *Phys. Rev. Lett.*, 8, 21–22 (1962).
14. S. A. Akhmanov, A. I. Kovrigin, R. V. Khokhlov, and O. N. Chunaev, *Zh. Eksp. Theor. Fiz*, vol. 45, p. 1336, 1963; *JETP Vol.18, No.4, P. 919* (1964)
15. J. A. Armstrong, "Interactions between light waves in a nonlinear dielectric", *Phys. Rev.* 127 (6), 1918 (1962)
16. R. H. Kingston, *Proc. IRE* 50, 472 (1962)
17. N. M. Kroll, *Phys. Rev.* 127, 1207 (1962)
18. S. A. Akamahov and R. V. Khokhlov, *Soviet Phys. JETP* 16, 252 (1953)
19. J. A. Giordmaine and R. C. Miller, *Phys. Rev. Lett.* 14, 973 (1965)
20. R. G. Smith, *Optical parametric oscillators (Lasers)*, ed.: A. K. Levine and A. J. Demaria, Marcel Dekker Inc, New York 1976, pp: 189-207.
21. L. E. Myers, R. C. Eckardt, M. M. Fejer, R. L. Byer, W. R. Bosenberg, and J. W. Pierce, *J. Opt. Soc. Am. B*, 12, 2102 (1995)
22. D. S. Hum and M. E. Fejer, *Quasi-phasematching*, *C. R. Physique* 8, 180 (2007)
23. R. L. Byer and A. Piskarskas, Feature issue on: Optical parametric oscillator and amplification, ed.: *J. Opt. Soc. Am. B* 10, 1655 (1993)
24. R. L. Byer and A. Piskarskas, Feature issue on: Optical parametric oscillator and amplification, ed.: R. L. Byer and A. Piskarskas, *J. Opt. Soc. Am. B* 10, 2147 (1993)
25. C. Chen et al., A New- Type Ultraviolet SHG Crystal - β -BaB₂O₄, *Sci. Sin Ser. B* 28, 235 (1985).
26. Y. X. Fan et al., *Proc. Conf. on Lasers and Electro-Optics*, 527 (1988).
27. L. K. Cheng et al., *Appl. Phys. Lett.* 53(3), 175 (1988).

28. Y. X. Fan, R. C. Eckardt, R. L. Byer, C. Chen, and A. D. Jihang, *IEEE J. Quantum Electron.* QE 25, 1196 (1989)
29. A. Fix, T. Schroder, and R. Wallenstein, *Laser Optoelektron*, 23, 106 (1991)
30. Y. X. Fan, R. C. Eckardt, R. L. Byer, J. Notling, and R. Wallenstein, *Appl. Phys. Lett.* 53, 2014 (1988)
31. W. R. Bosenberg, W. S. Pelouch, and C. L. Tang, *Appl. Phys. Lett.* 55, 1952 (1989)
32. W. R. Bosenberg and C. L. Tang, *Appl. Phys. Lett.* 56, 1819 (1990)
33. Y. Wang, Z. Xu, D. Deng, W. Zheng, X. Liu, B. Wu, and C. Chen, *Appl. Phys. Lett.* 58, 1461 (1991)
34. A. Fix, T. Schroder, R. Wallenstein, J. G. Haub, M. J. Jhonson, and B. J. Orr, *J. Opt. Soc. Am. B*10, 1744 (1993)
35. H. Komine, *Opt. Lett.* 13, 643 (1988)
36. M. Ebrahimzadeh, A. J. Henderson, and M. H. Dunn, *IEEE J. Quantum Electron.* QE-26, 1241 (1990)
37. J. Pinard and J. F. Young, *Opt. Commun.* 4, 425 (1972)
38. T. K. Minton, D. W. Michael, K. Kolenbrander and J. M. Lisy, *Rev. Sci. Instrum.* 57, 1210 (1986)
39. A. Hordvik and P. B. Sacket, *Appl. Opt.* 13, 1060 (1974)
40. R. C. Bapna and K. Dasgupta, *Optics and Laser Technology*, 33, 125 (2001)
41. G. Robertson, A. Henderson and M. H. Dunn, *Appl. Phys. Lett.* 62, 123, 1993
42. J. E. Bjorkholm and H. G. Daniel meyer, *Appl. Phys. Lett.* 15, 171 (1969)
43. A. Borsutzky, *Quantum Semiclass. Opt.* 9, 191–207 (1997)

44. J. D. Miller, M. Slipchenko, T. R. Meyer, N. Jiang, W. R. Lempert, J. R. G. Gord, *Optics Letters* 34(9) 1309 (2009).
45. N. Jiang, M. C. Webster, and W. R. Lempert, *Applied Optics*, Vol. 48, 4, B23 (2008).
46. M. Peltz, Anstett U, Bader U, Bartchek J, Borsutzky A, Wallenstein R. *CLEO* 63 (1999).
47. B. Baillon, B. LeGarrec, L. A. Lompre. *Quantum semiclass. Optics*, 9, 285 (1997)
48. S. Wu, A.G.Blacke, *SPIE Proc*, 52, 3263 (1998)
49. D.W.Coutts, J.A.Piper, *IEEE J Quant Electron*, 28, 1761, (1992)
50. G. Anstett, G. Göritz, D. Kabs, R. Urschel, R. Wallenstein, A. Borsutzky, *Appl. Phys. B* 72, 583 (2001)
51. R. W. Boyd, *Nonlinear Optics*, Academic Press, San Diego, CA, 1992
52. Y. R. Shen, *Principles of Nonlinear Optics*, John Wiley and Sons, New York, 1984
53. R. L. Sutherland, *Handbook of Nonlinear optics*, Dekker, New York, 2003
54. S. E. Harris, *Proc. IEEE* 57, 2096 (1969)
55. J. M. Manley and H. E. Rowe, *Proc. IRE* 47, 2115 (1959)
56. W. H. Louisell, A. Yariv, and A. E. Seigman, *Phys. Rev.*124, 1646 (1961)
57. A. Yariv, *Quantum Electronics*, John Wiley, New York (1989)
58. M. M. Fejer, G. A. Magel, D. H. Jundt, and R. L. Byer, *IEEE J. Quantum Electron.* 28, 2631 (1992).
59. A.V. Smith, *SNLO Nonlinear Optics Code (Ver. 60) (AS-Photonics, Albuquerque) (2013)*
60. V. G. Damitrev, G. G. Gurzadyan, and D. N. Nicogosyan, *Handbook of Nonlinear optical crystals*, 2 nd edition, Springer-Verlag, Berlin (1997)
61. M. V. Hobden, *Phase-Matched Second-Harmonic Generation in Biaxial Crystals*, *Journal of Applied Physics*, 38, 4365 (1967)

62. G. D. Boyd, A. Askin, *Phys Rev*, 37, A1305 (1965)
63. W. R. Bosenberg, W. S. Pelouch and C. L. Tang, *Appl. Phys. Lett.* 55, 1953 (1989)
64. D. J. Kuizenga, *Appl. Phys. Lett.* 21, 570 (1972)
65. R.C. Bapna, Investigations of pulsed β -barium borate optical parametric oscillator, Ph. D thesis, University of Mumbai, (2008)
66. S. J. Bronson and R. L. Byer, *IEEE J. Quantum Electron.* QE-15, 415 (1979)
67. N. Nikogosyan, *Appl. Phys. A* 52, 359 (1991)
68. T. Schroder, K. J. Boller, A. Fix, and R. Wallenstein, *Appl. Phys.* B58, 425 (1994)
69. H. Q. Li et al., *Opt. Commun.* 232, 411 (2004)
70. D. E. withers et al., *J Opt. Soc. Am. B* 10, 1737 (1993)
71. I.T. Sorokina and K.L. Vodopyanov, (Eds.), Solid-state mid-infrared laser sources, *Topics in Applied Physics* 89, Springer-Verlag, Berlin Heidelberg (2003).
72. N. Nikogosyan, *Nonlinear Optical Crystals: A Complete Survey*, Springer (2010).
73. K. L. Vodapyanov, F. Ganikhanov, J. P. Maffetone, I. Zwieback, and W. Ruderman, *Opt. Lett.* 25, 841 (2000)
74. G. D. Boyd, and D. A. Kleinman, *Journal of Applied Physics*, 39, 3597 (1968)
75. Y. Suematsu, *Jpn. J. Appl. Phys.*, 11, 387 (1972)
76. R. Fisher, C. Tran-ba and L.W. Wiecezorek, *Sov. J. Quantum Electron.* 7, 1455 (1977)
77. J. A. C. Terry, Y. Cui, Y. Yang, W. Sibbett, and M. H. Dunn, *J. Opt. Soc. Am. B*, Vol. 11, pp 758 (1994)
78. R. C. Bapna, C.S. Rao, K. Dasgupta, *Opt. Laser Technol.* 40, 832 (2008)
79. S. Guha, F. Wu and J. Falk, *IEEE J. Quantum Electron.* QE-18, 907 (1982)
80. T. W. Tukker, C. Otto, and J. Greve, *J.Opt.Soc. Am. B*, 15, 2455 (1998)

81. C. S. Rao, S. Kundu, A.K Ray, Appl. Phys. B, 124, 163 (2018)
82. H. Wang and A.M.Weiner, IEEE J. Quantum Electron. QE-39, 1600 (2003)
83. C. Ward and K. David, Numerical mathematics and computing, 6th Edition, Thomas Learning Inc. (2008),
84. W.R.Bosenberg, L.K.Cheng and C.L.Tang, Ultraviolet optical parametric oscillation in β -BaB₂O₄, Appl. Phys. Lett. 54,13-15 (1989)
85. Y. Cui, M.H.Dunn, C. J. Nome, W. Sibbett, B. D. Sinclair, Y. Tang and J. A. C. Terry, Opt. Lett. 17 646, (1992)
86. Y. Cui, D. E. Withers, C. F. Rae, C. J Norrie, Y. Tang, B. D.Sinclair, W.Sibbett and M. H.Dunn, Opt. Lett. 18 122-4 (1993)
87. L. R. Marshall, J. Kasinski and R. L. Burnham, Opt. Lett. 16 1680, (1991)
88. L. E. Myers and W. R. Bosenberg, IEEE J. Quantum Electron. 33 1663-72 (1997)
89. U. Bader, J. Bartschke, I. Klimov, A. B. Orszutsky and R. Wallenstein, Opt. Commun. 147, 95-8 (1998)
90. D. Hon In: Stich M L, editor. Laser handbook. Amsterdam: North, Holland; 1979.
91. S. Wu, G.A. Blake, Z. Sun, J. Ling, Appl. Opt. 36, 5898 (1997)
92. J. M. Boon-Engering, W. E. van der Veer, and J. W. Gerritsen, Optics Letters, Vol. 20, PP. 380 (1995)
93. J. G. Haub, M. J. Johnson, and B. J. Orr, Appl. Phys. Lett. 58, 1718 (1991)
94. W. R. Bosenberg and D. R. Guyer, J. Opt. Soc. Am. B 10, 1716 (1993).
95. B. C. Johnson, V. J. Newell, J. B. Clark, and E. S. McPhee, J. Opt. Soc. Am. B / Vol. 12, 2122 (1995)
96. N.P. Barnes, J.A. Williams-Byrd, J. Opt. Soc. Am. B 12, 124, (1995)

97. J. G. Haub, M. J. Johnson, A. J. Powell, and B. J. Orr, *Optics Letters*, vol.20, 1637, (1995)
98. J.E. Bjorkholm, A. Ashkin, R.G. Smith, *IEEE J. Quantum Electron.* QE-6, 797 (1970)
99. R. Urschel, U. Bader, A. Borsutzky, R. Wallenstein, *J. Opt. Soc. Am. B*, 16, 565 (1999)
100. O.Svelto, “Principles of Lasers”, Fifth edition, Springer US, (2010)
101. P Griffith, D Silberman, “Optical Mounts: Ignore Them at your Peril”, *Photonics Spectra*, September (1998).
102. S. Lavi, L. A. Levin, J. Liran, and E. Miron, “Efficient oscillator-amplifier dye laser pumped by a frequency doubled Nd:YAG laser”, *Appl. Opt.*18, 525 (1979)
103. S. T. Lin, Y. Y. Lin, Y. C. Huang, A. C. Chiang, and J. T. Shy, *Opt. Lett.* 33(20), 2338–2340 (2008).
104. M. Vainio, J. Peltola, S. Persijn, F. J. M. Harren, and L.Halonen, *Appl. Phys. B* 94, 411 (2009).
105. M. Takahashi, A. Osada, A. Dergachev, P. F. Moulton, M. Cadatal-Raduban, T. Shimizu, and N. Sarukura, *J. Cryst. Growth* 318(1), 606–609 (2011)
106. R. Bhandari, T. Taira, A. Miyamoto, Y. Furukawa, and T. Tago, *Opt. Mater. Express* 2(7), 907–913 (2012).
107. H.Komine, *J. Opt. Soc. Am. B* 10, 1751 (1993)
108. R. Riedel, J. Rothhardt, K. Beil, B. Gronloh, A. Klenke, H. Höppner, M. Schulz, U. Teubner, C. Kränkel, J. Limpert, A. Tünnermann, M. J. Prandolini, and F. Tavella, *Opt. Express*, Vol. 22, PP 17607 (2014).
109. D. Eimerl, L. Davis, S. Velsko, E.K. Graham, A. Zalkin, *J. Appl.Phys.* 62, 1968 (1987)
110. L.A.W. Gloster, I.T. McKinnie, Z.X. Jiang, T.A. King, J.M. Boon-Engering, W.E. van der Veer, W. Hogervorst, *J. Opt. Soc. Am. B* 12, 2117 (1995)

111. J. Rothhardt, S. Demmler, S. Hädrich, T. Pesche, J. Limpert, A. Tünnermann, *Opt. Lett.* 38, 763 (2013)
112. C. Rothhardt, J. Rothhardt, A. Klenke, T. Peschel, R. Eberhardt, J. Limpert, A. Tünnermann, *Opt. Mater. Express* 4, 1092 (2014).
113. H. Kaushal and G. Kaddoum, “Underwater optical wireless communication,” *IEEE Access* 4, 1518–1547 (2016).
114. Z. Zeng, S. Fu, H. Zhang, Y. Dong, and J. Cheng, “A survey of underwater optical wireless communications,” *IEEE Comm. Surv. and Tutor.* 19(1), 204–238 (2017).
115. P. Tian, X. Liu, S. Yi, Y. Huang, S. Zhang, X. Zhou, L. Hu, L. Zheng, and R. Liu, “High-speed underwater optical wireless communication using a blue GaN-based micro-LED,” *Opt. Express* 25(2), 1193–1201 (2017).
116. C. Wang, H. Yu, and Y. Zhu, “A long distance underwater visible light communication system with single photon avalanche diode,” *IEEE Photonics J.* 8(5), 7906311 (2016).
117. Y. Chen, M. Kong, T. Ali, J. Wang, R. Sarwar, J. Han, C. Guo, B. Sun, N. Deng, and J. Xu, “26 m/5.5 Gbps underwater optical wireless communication based on an OFDM-modulated 520-nm laser diode,” *Opt. Express* 25(13), 14760–14765 (2017).
118. H. M. Oubei, J. R. Duran, B. Janjua, H. Y. Wang, C. T. Tsai, Y. C. Chi, T. K. Ng, H. C. Kuo, J. H. He, M. S. Alouini, G. R. Lin, and B. S. Ooi, “4.8 Gbit/s 16-QAM-OFDM transmission based on compact 450-nm laser for underwater wireless optical communication,” *Opt. Express* 23 (18), 23302–23309 (2015).
119. T. C. Wu, Y. C. Chi, H. Y. Wang, C. T. Tsai, and G. R. Lin, “Blue laser diode enables underwater communication at 12.4 Gbps,” *Sci. Rep.* 7, 40480 (2017).

120. C. Shen, Y. Guo, H. M. Oubei, T. K. Ng, G. Liu, K. H. Park, K. T. Ho, M. S. Alouini, and B. S. Ooi, "20-meter underwater wireless optical communication link with 1.5 Gbps data rate," *Opt. Express* 24(22), 25502–25509 (2016).
121. P. Lacovara, "High-bandwidth underwater communications," *Marine Technol. Soc. J.* 42, 93–102 (2008).
122. N. Farr, A. D. Chave, L. Freitag, J. Preisig, S. N. White, D. Yoerger, and F. Sonnichsen, "Optical modem technology for seafloor observatories," in *Proceedings of IEEE Oceans* (IEEE, 2006), pp. 1–6.
123. X. Liu et al., *Opt. Express*, 26, 15, 19259–19274 (2018).